Experimental Investigation into Spatial Quantum Optical Properties for Satellite Targeting through the Turbulent Atmosphere

by

Christopher Pugh

A thesis
presented to the University of Waterloo
in fulfillment of the
thesis requirement for the degree of
Master of Science
in
Physics–Quantum Information

Waterloo, Ontario, Canada, 2013

AUTHOR'S DECLARATION

I hereby declare that I am the sole author of this thesis. This is a true copy of the thesis, including any required final revisions, as accepted by my examiners.

I understand that my thesis may be made electronically available to the public.

Christopher Pugh

Abstract

A major field of research at the current time is that of implementing Quantum Key Distribution over large distances using satellites. If this protocol works with this technology, it will have huge implications on future information security. In order for a satellite to implement this idea, there are many aspects that must be taken into account. One of the big issues that comes up for this type of system is that of propagating light through the turbulent atmosphere and its effects on the acquisition, pointing and tracking system. The projects studied in this thesis study some of the effects of the atmosphere on certain detectors, try to develop pointing schemes for better accuracy as well as develop knowledge in free space propagation of other single photon experiments.

In the first experiment, I study the spatial correlations of the daughter photons created in spontaneous parametric down conversion. I look at the effect of altering the pump beam on the positions of the down converted photons and see if the pump can be manipulated in a way to control the directions of the daughter photons. I begin to utilize a deformable mirror and Shack-Hartmann wavefront sensor which are generally used in adaptive optics, but we plan to use them to alter the pump beam in the spontaneous parametric down conversion process to analyze the correlations between the pump and down converted photons.

The second experiment investigates the effects of laser scintillation on the performance of a possible tracking device that could be implemented on a satellite. This quad sensor tracks the position of a beam and a system will be developed to move the sensor to keep the beam in the center where there is a hole for the quantum single photons to stream through. In order to create the effects of scintillation, a turbulence simulator box was built and characterized. This box combines wind turbulence with a heat gradient to mimic atmospheric turbulence on a small scale.

Finally, my contributions to a large scale, long distance free space quantum optics experiment are explained and the overall goal of the experiment is discussed. This experiment exposed me to actual free space transmission issues as well as many fundamental techniques for performing long distance optics experiments. In this experiment there was no correction for atmospheric turbulence, but in the future, techniques could be implemented which might increase the efficiencies of the free space links.

Acknowledgements

I would like to begin by giving my deepest thanks to my Lord and God Jesus Christ. Without him, I am nothing and I owe him my life. The Catholic Church means so much to my life I would be lost without it.

For my research, I would like to thank my supervisor Thomas Jennewein, for his continued guidance and support through my entire degree. For his encouragement when results were down and his praise when accomplishments were made. I would also like to thank the members of Dr. Jennewein's research group who have helped me along the way, in particular Dr. Piotr Kolenderski for his leadership and help with my main experiment, Dr. Brendon Higgins who has helped teach me the ways of science and has provided much needed technical writing knowledge, and Dr. Chris Erven who transferred some of his knowledge, most of his equipment and his office to me. Thanks also go to Jean-Philippe Bourgoin (for this thesis template), Evan Meyer-Scott, Deny Hamel, Catherine Holloway, and Dr. Rolf Horn for help and fruitful discussions. Another special thanks goes to Aimee Heinrichs for walking the thin line between hope and despair with me and ending with hope. I would also like to thank Dr. Rob Hill and Dr. Kevin Resch for being on my examining committee and Dr. Avery Broderick for being on my Masters committee.

Thank you also to my friends, family and the Knights of Columbus who have provided me with love and support and dinners throughout this journey. With their help, I look forward to my future PhD work.

Dedication

To my wonderful parents William and Brenda Pugh–without whom I would not be where I am today.

Table of Contents

List of Tables

List of Figures

Chapter 1

Introduction to Quantum Links in Free Space

Current classical cryptographic infrastructure is a very robust and safe way to ensure that data can be transferred from one point to another without being revealed to an adversary. However, with current research into quantum computing, it has been discovered that these schemes are not safe against quantum computers. Therefore, there is a need for a cryptographic system which will be safe against these systems. This is where Quantum Key Distribution is very important [1, 2]. Quantum Key Distribution uses the principles of quantum mechanics, which relies on probabilities to ensure complete security when creating a secret key between two parties. The scheme is able to detect the presence of eavesdroppers and can therefore prevent the transmission of secret data before it enters a public channel. Once a secret key is generated with the assurance that the two parties involved are the only ones with knowledge of that key, they can then encrypt the data classically and send the information over a public channel with confidence of it remaining safe.

1.1 Towards a Global Quantum Cryptography Network

There are two ways to implement quantum communications and cryptography systems with photons: with fiber and in free space. In fiber, the distance is limited due to the loss through the cable, and currently distances of around 150km have been achieved [3]. With free space, current tests and systems are limited to line of sight, which due to the curvature and terrain of the Earth is similarly limited to around 250km. However, if there was a way for two locations on earth to be connected (even at different times) with optical links, quantum cryptography systems with photons could then be implemented globally.

One proposal to implement such a device is the Quantum EncrYption and Science Satellite (QEYSSat).

The main purpose of QEYSSat is to demonstrate Quantum Key Distribution (QKD) over very large distances. The satellite will fly in a low earth orbit ($\approx$ 600km) and pass over specialized ground stations. While the satellite passes over one ground station, a link from the ground to the satellite will be established (uplink) and QKD performed. When the satellite then passes over another ground station located somewhere else on the earth, another uplink will be established and QKD performed. A combination of the two constructed keys is sent to the ground stations, which will link them with a common secure key.

Extensive studies have been completed investigating the losses and analyzing links links available between ground stations and satellites [4, 5]. A few of the issues which have sparked interest following this work involve loss due to atmosphere and acquisition, pointing and tracking systems. Further information pertaining to these issues is discussed in following sections of this chapter, and some experiments done to study these effects are presented in later chapters.

One of the most important features required to implement a satellite for optical communications is the acquisition, pointing and tracking system. Many different systems have been proposed [6–14] and some implemented. The purpose of this system is to first establish contact between the satellite and the ground station in the acquisition phase. Once the sender and receiver are looking at each other, they need to remain looking at each other throughout the satellite pass and maintain a level of precision dependent on the purpose of the link. This is where the pointing and tracking are important. Different systems require different accuracies and precision and thus there is not a single system that would be appropriate for all systems. Single photons will be used in the QEYSSat mission, and with that single photon detectors will also be used. After noise, cooling, and small active areas of these detectors are taken into account, it is very important to have an extremely accurate pointing system so as many photons as possible are collected and thus the key generation rate is higher. In Chapter 3 one possible device to achieve this pointing is tested under the effects of laser scintillation. Chapter 2 describes an experiment investigating the spatial correlations of the photons created in spontaneous parametric down conversion, and considers whether they can be utilized for a pointing mechanism.

1.2 Atmospheric Turbulence

An unfortunate drawback to free space optical experiments through the atmosphere is the effects of turbulence on the optical beam. These effects cause many distortions such as scintillation, beam wander and higher order effects. Atmospheric turbulence makes it quite difficult to achieve the desired results from an experiment, but there are mitigation strategies, as will be seen later. Due to the large amount of information available on atmospheric turbulence, it is difficult to summarize the entire field, thus I will only focus on the significant parameters (refractive index structure constant, C_n^2, inner scale, l_0, outer scale, L_0, and the Fried's coherence length, r_0) and theory related to the experiments detailed in the chapters of this thesis.

Turbulence in the atmosphere is caused by natural small variations in temperature [15]. These variations cause changes in wind velocity, also known as eddies, which in turn changes the density of the air in various locations. Since the density is different in successive "pockets" in the atmosphere, the refractive index that the light experiences changes as the beam propagates.

A clear way to see the effects of atmospheric turbulence is to gaze upon a star in the night sky. It is observed that the star twinkles and wanders a very small amount. The twinkling of the star is caused by random intensity fluctuations due to the beams of light from the star passing through different atmospheric paths and therefore experiencing different amounts of interference. The random wander is caused by the slight changes in the angle-of-arrival due to the small changes in the refractive index of the atmosphere. If using a telescope to observe the star, another effect that can be seen is the spreading out of the star in the image–this is caused by higher order aberrations from the atmospheric turbulence and similar results for a local point source will be examined in Chapter 3.

Some of these common effects have familiar names associated with them. The random intensity fluctuations in the light is known as scintillation. The slight shifting of the position of the beam or object is known as beam wander or tilt. These are both low order aberrations from the atmosphere. Some of the terms for the higher order aberrations are closely related to issues one may have with their eyes such as astigmatism or coma. These and more of the higher order aberrations will be discussed in the coming section.

Atmospheric turbulence has been well studied and many models have been proposed, but it is so complex that a statistical interpretation is the best model possible. One of the most prominent theories to describe atmospheric turbulence is that of Kolmogorov [16, 17]. In his work, he determined the mean-square velocity difference between two points which are separated by a displacement vector $\mathbf{r}$ in space. We can see the velocity structure tensor

as [15, 18]

$$D_{ij} = \langle [\upsilon_i(\mathbf{r}_1 + \mathbf{r}) - \upsilon_i(\mathbf{r}_1)][\upsilon_j(\mathbf{r}_1 + \mathbf{r}) - \upsilon_j(\mathbf{r}_1)] \rangle, \tag{1.1}$$

where υ_i is the velocity component in the i^{th} direction, $\mathbf{r}_1$ is a slightly changed path, and the angle brackets represent an ensemble average.

Since this equation is very challenging to solve for real velocity situations, three assumptions will be made.

1. The atmosphere is locally homogeneous, or simply, the velocity depends only on the vector $\mathbf{r}$ [16].
2. The atmosphere is locally isotropic; again more simply, the velocity only depends on the magnitude of $\mathbf{r}$ [16].
3. The turbulence is in-compressible, $\nabla \cdot \mathbf{v} = 0$ [19].

The first two assumptions now allow Equation 1.1 to be written as

$$D_{ij} = [D_{\parallel}(r) - D_{\perp}(r)]n_i n_j + D_{\perp}(r)\delta_{ij}, \tag{1.2}$$

where n_i are the components of the unit vector along $\mathbf{r}$. $D_{\parallel}$ is the structure function of the wind velocity component parallel to $\mathbf{r}$ and $D_{\perp}$ transverse to $\mathbf{r}$. Using the final assumption, $D_{\parallel}$ and $D_{\perp}$ can be related as

$$D_{\perp} = \frac{1}{2r}\frac{d}{dr}(r^2 D_{\parallel}). \tag{1.3}$$

This results in a final structure function given by

$$D_{\parallel} = \langle [\upsilon_r(\mathbf{r}_1 + \mathbf{r}) - \upsilon_r(\mathbf{r}_1)]^2 \rangle. \tag{1.4}$$

If the distance between the two points is within the inertial sub-range (meaning it is between the inner and outer scales to be defined and explained below) of turbulence, the structure function becomes [17]

$$D_{\parallel} = D_{\upsilon} = C_{\upsilon}^2 r^{2/3}, \tag{1.5}$$

where C_{υ} is the velocity structure constant. This constant provides a measure of the energy in the turbulence. Referring back to the description of turbulence being caused by "eddies" in the atmosphere, this structure function only applies when r is larger than the smallest eddy size, l_0, and smaller than the largest eddy size, L_0, also known as the inner or Kolmogorov scale and outer scale respectively. The inner scale is the limit where the the viscosity of the fluid becomes important and the dissipation of the energy due to these

effects starts to have an impact. The inner scale is related to the viscosity, v, of the fluid and the kinetic energy, ε, of the turbulence by [20, 21]

$$l_0 = 7.4 \left(\frac{\mathrm{v}^3}{\varepsilon} \right)^{1/4}. \tag{1.6}$$

In Earth's atmosphere, this value usually ranges from a few millimeters to a few centimeters from the ground to the troposphere.

The outer scale is the length limit where the turbulent flow is no longer isotropic and assumption 2 is no longer valid. This value tends to range from a few meters to hundreds of meters in the atmosphere. When near the ground, below approximately 1km elevation, this value tends as $L_0 \approx 0.4h$, where h is the height above ground [22].

A more useful form of structure constant changes the velocity structure constant to the refractive index structure constant. As mentioned earlier, small changes in atmosphere change the index of refraction of the path which light traverses. The refractive index, n, in the atmosphere varies with pressure, temperature and wavelength in approximately the following way [18]:

$$n - 1 = 77.7(1 + 7.52 \times 10^{-3}\lambda^{-2})(P/T)10^{-6}, \tag{1.7}$$

for optical wavelengths and where λ is in micrometers, pressure, P, is in millibars and temperature is in Kelvin. An important step to convert these quantities is by using conservative passive additives [18, 22–24]. Using Equation 1.7 and passive additives, the index of refraction structure is determined to be

$$D_n(r) = C_n^2 r^{2/3}, \tag{1.8}$$

when $l_0 < r < L_0$ and C_n^2 is the refractive index structure constant. This quantity is now related to the strength of turbulence.

We now find a function that will be useful for our experiments in Chapter 3. An assumption is used that the turbulence generated can be described by a refractive index spatial power spectrum [25, 26]. The final form of this power spectrum is given by

$$\Phi_N(K) = 0.033 C_N^2 (K^2 + K_0^2)^{-11/6} \exp\left(-\frac{K^2}{K_m^2} \right), \tag{1.9}$$

where K is the three dimensional spatial wave number, $K_0 = 2\pi/L_0$ and $K_m = 2\pi/l_0$. With respect to spatial frequencies (useful for our purposes) this can be written as

$$W_N(\mathbf{f}) = (2\pi)^3 \Phi_N(2\pi\mathbf{f}). \tag{1.10}$$

The variance of the angle of arrival (AoA) is related to this power spectrum function, and we now have a way of determining L_0, l_0 and C_n^2 by calculating the variance and fitting the following model to the data [25]

$$\sigma_{AoA}^2 = 1.19 C_N^2 \delta h \int_0^\infty f^3 \left(f^2 + \frac{1}{L_0^2}\right)^{-11/6} \exp\left(-l_0^2 f^2\right) \left[\frac{2J_1(2\pi w f)}{(2\pi w f)}\right]^2 \mathrm{d}f, \tag{1.11}$$

where J_1 is a Bessel function of the first kind and w is the diameter of the pupil which the beam passes through before being focused and measured. The term in square brackets is added to take into account the effect of the pupil, in this case, a circular aperture.

One last important parameter that must be considered is Fried's coherence length [27, 28], commonly symbolized as r_0. This value, represents the maximum diameter of a collector, such as a telescope, before the atmospheric turbulence significantly reduces its performance. For a plane wave traveling through the atmosphere it can be calculated as [15]

$$r_0 = \left[0.423 k^2 \sec(\beta) \int_0^L C_n^2(z) \mathrm{dz}\right]^{-3/5}, \tag{1.12}$$

where L is the path length and β is the zenith angle and $k = 2\pi/\lambda$. For a spherical wave, it becomes:

$$r_{0sph} = \left[0.423 k^2 \sec(\beta) \int_0^L C_n^2(z) \left(\frac{z}{L}\right)^{5/3} \mathrm{dz}\right]^{-3/5}. \tag{1.13}$$

The r_0 value can also correspond to the size of a transmitter where atmospheric turbulence significantly reduces its transmission abilities as will be the case for a satellite uplink transmitter. In other words, this length is the maximum size of a transmitter or collector which is limited in performance by diffraction. Any device larger than this will not have any increased image or signal quality as the atmosphere will now limit transmission quality. Common values for this length in the atmosphere can be around 10cm for an average night and around 20cm for a really good night with a clear sky.

1.3 Adaptive Optics Applied to Quantum Links

Adaptive optics is a technique used to improve an optical signal that undergoes some sort of deformation as it propagates. It has been used in astronomy to improve the quality of images recorded with telescopes [29, 30], in optometry to obtain useful images of the retina [31], to improve optical communications signals [32, 33] and has even been proposed to assist in destroying space debris [34]. Two great review articles and a book on adaptive optics are given in [15, 35, 36]. The principle of adaptive optics is to measure the distortion

along the path the light is to travel, and apply a correction to the light so that by the time it passes through the disturbance, it arrives pristine. Many different ways have been developed to implement adaptive optics, possessing advantages and disadvantages for each situation [37–41].

Although adaptive optics might be useful for our application of propagating single photons to a satellite by applying the correction to the beam before sending it, that is not the focus of our use of the technique here. We are interested in using an adaptive optics system to determine the affect of altering the spatial properties of the pump beam in the process of spontaneous parametric down conversion which is used as a single photon source.

For a satellite uplink, we face more atmospheric interference than if a downlink was used, however, by having an uplink we are able to keep the source on the ground, and therefore have the ability to use various sources for different experiments (see Figure 1.1). If the source were on the satellite, as in a downlink, one could not swap it when a different experiment is to be performed. There are two possible ways we can use adaptive optics for our scheme. First of all, we can apply corrections to the pump beam mode shape to hopefully correct for any atmospheric disturbances the photon beam created through spontaneous parametric down conversion may experience while passing through the atmosphere. This is possible since the beams created must contain the characteristics of the pump beam (more discussion on this topic in Section 1.4). This differs from the usual scheme since we are manipulating the pump instead of the beam which will pass through the atmosphere. The second method is to use a combination of adaptive optics and the spatial correlations of spontaneous parametric down conversion to develop a pointing scheme as discussed in Chapter 2. Both of these schemes will help increase the transmittance of photons from a ground station to the satellite and hopefully make each pass of the satellite more successful in generating key.

There are many different ways of implementing an adaptive optics system, but the discussion here will be limited to a Micromachined Membrane Deformable Mirror (MMDM) and a Shack-Hartmann Wavefront Sensor.

1.3.1 Zernike Polynomials

The wavefront of a propagating light wave can be easily represented by a power series of polynomials known as the Zernike Polynomials [42]. These polynomials are especially useful as they are orthonormal over a circle and easily represented in polar coordinates [43]. As most telescopes and optical apertures are circular, this is especially beneficial. It

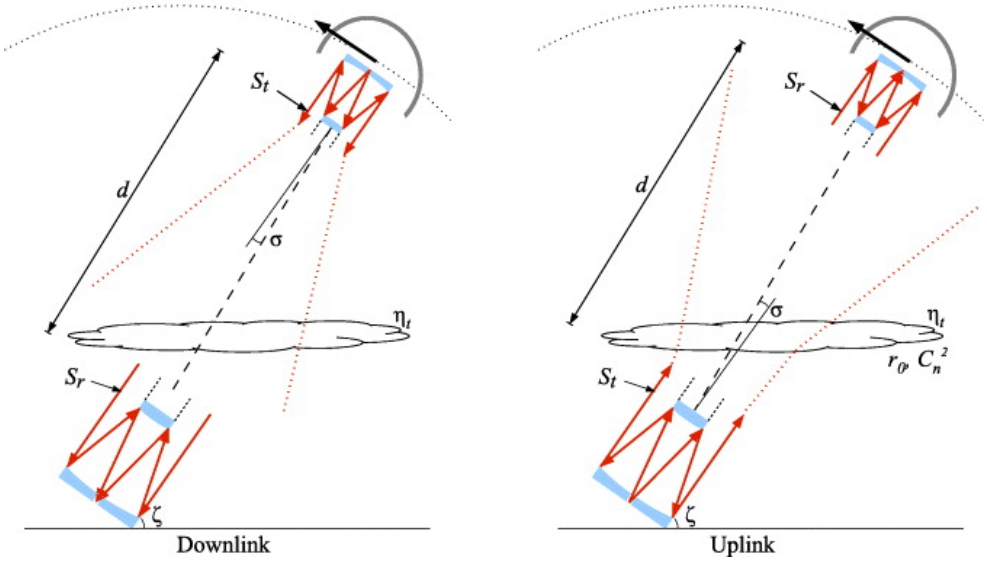

Figure 1.1: Atmospheric turbulence affecting a satellite downlink as compared to a satellite uplink. Figure used with permission from [5]. Having the atmosphere at the beginning of the transmission line causes a larger spread of the beam than having the atmosphere at the end. This causes larger pointing errors for an uplink which adaptive optics can be useful in solving. In this figure, S_t is the transmitter's surface, S_r is the receiver's surface, σ is the pointing error, d is the distance between the satellite and the ground station, ξ is the elevation angle from the ground, η_t is the atmospheric transmittance, and r_o and C_n^2 are as described above.

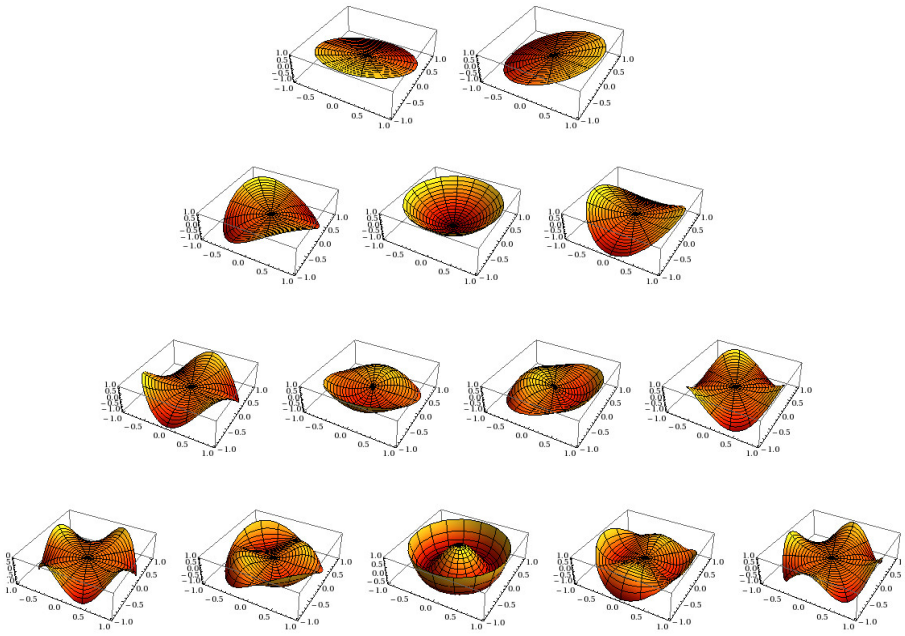

Figure 1.2: Three dimensional representation of the Zernike polynomials up to order 4 with order increasing as you move down and frequency increasing as you move from left to right.

has also been shown that this polynomial series is well structured to model the effects of wavefront distortion caused by atmospheric turbulence [44, 45]. The Zernike polynomial series is given as

$$\begin{aligned} Z_n^m(\rho,\varphi) &= R_n^m(\rho)\cos(m\varphi),\ \ m \geq 0, \\ Z_n^m(\rho,\varphi) &= R_n^m(\rho)\sin(m\varphi),\ \ m < 0, \end{aligned} \tag{1.14}$$

with

$$R_n^m(\rho) = \begin{cases} \displaystyle\sum_{k=0}^{(n-m)/2} \frac{(-1)^k(n-k)!}{k!((n+m)/2-k)!((n-m)/2-k)!}\rho^{n-2k} & n-m \text{ even} \\ 0 & n-m \text{ odd} \end{cases} \tag{1.15}$$

Figures 1.2 and 1.3 show 3 dimensional and 2 dimensional representations of the Zernike polynomials, respectively, up to order 4 (order is given by the n value and frequency is given by the m value which varies from $-n$ to n in steps of 2).

The Zernike terms can be related to common optical aberrations as seen in Table 1.1. In the next section we explore one device capable of implementing these polynomial representations onto an optical wavefront.

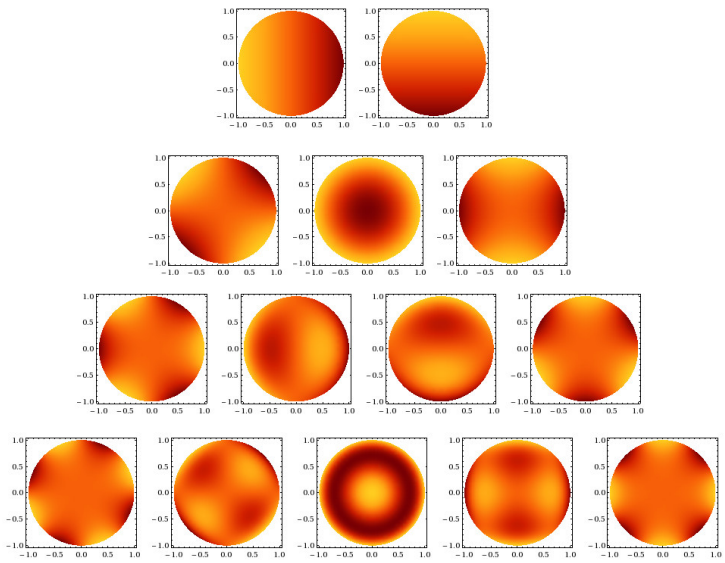

Figure 1.3: Two dimensional representation of the Zernike polynomials up to order 4 with order increasing as you move down and frequency increasing as you move from left to right.

Order (n)	Frequency (m)	Aberration
1	1	Tilt
2	0	Focus
2	2	Astigmatism
3	1	Coma
4	0	Spherical aberration

Table 1.1: Order and frequency of different Zernike terms and their associated physical aberration.

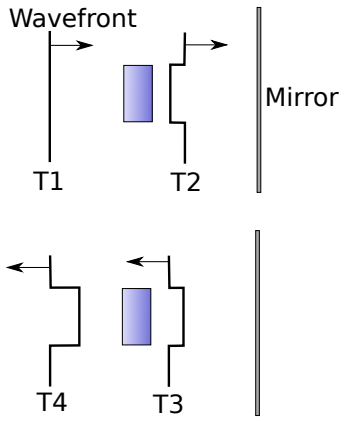

Figure 1.4: Position of a wavefront as it passes through a piece of glass twice reflecting off a mirror in between. The mirror is a regular silvered mirror. Each of the T's represents the next step in time sequentially.

1.3.2 Wavefront Correction

The goal of the deformable mirror is to perform phase conjugation which will reverse the effect of the turbulent medium the light is to propagate through. As seen in [15], if a piece of glass is placed in front of a plane wave and the wave then reflects off a mirror and passes through the glass again, the wave will be distorted as shown in Figure 1.4. The glass has a higher index of refraction than the air and therefore delays the portion of the wavefront which passes through it. The effect is amplified on the second pass through the glass. If the mirror were to apply some sort of distortion to the wavefront to correct for the glass, the aberration can be removed as shown in Figure 1.5

In order to describe Figures 1.4 and 1.5 mathematically we will assume that the input wave was a plane wave described by $\mathbf{E}_1(x,y,z,\omega) = \mathbf{A}_0(x,y,z)e^{ikz-i\omega t}$ [46] (apertures will be neglected in this discussion). As the wave passes through the piece of glass, it picks up a phase and becomes

$$\mathbf{E}_2(x,y,z,\omega) = \mathbf{A}_0(x,y,z)e^{i(kz+\varphi(x,y,z))-i\omega t}. \tag{1.16}$$

If the wave now reflects off the ordinary mirror in Figure 1.4 the momentum portion of the wave is flipped and is described as

$$\mathbf{E}_3(x,y,z,\omega) = \bar{R}\cdot\mathbf{A}_0(x,y,z)e^{i(-kz+\varphi(x,y,z))-i\omega t}, \tag{1.17}$$

where $\bar{R}$ is an amplitude factor which is dependent on the reflectivity of the mirror. After the wave passes through the glass once more, the phase from the distortion is doubled from

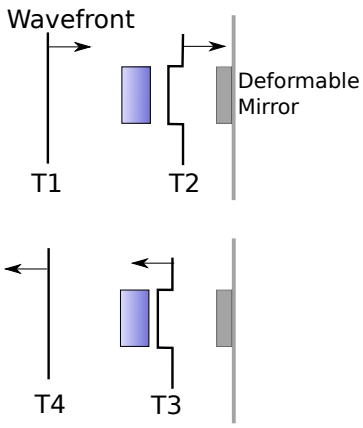

Figure 1.5: The mirror in this setup has been designed to correct the deformation that the glass puts on the wavefront.

the second pass and the final departing wave is:

$$\mathbf{E}_4(x,y,z,\omega) = \bar{R}\cdot\mathbf{A}_0(x,y,z)e^{i(-kz+2\varphi(x,y,z))-i\omega t}. \tag{1.18}$$

Now, if the reflective mirror is able to change shape as in Figure 1.5, the wave after the reflection, $\mathbf{E}'_3(x,y,z,\omega)$ is rather given as

$$\mathbf{E}'_3(x,y,z,\omega) = \bar{R}'\cdot\mathbf{A}_0(x,y,z)e^{i(-kz-\varphi(x,y,z))-i\omega t}. \tag{1.19}$$

It can be seen that the mirror conjugated the aberration phase as well. The $\bar{R}'$ factor could be slightly different in this case depending on the mirror and is now denoted with a prime. Now the wave will pass through the glass piece and become

$$\mathbf{E}'_4(x,y,z,\omega) = \bar{R}'\cdot\mathbf{A}_0(x,y,z)e^{i(-kz-\varphi(x,y,z))+i\varphi(x,y,z)-i\omega t} = \bar{R}'\cdot\mathbf{A}_0(x,y,z)e^{-ikz-i\omega t}. \tag{1.20}$$

After passing through the glass piece two times and reflecting off the phase conjugating mirror, the final wave is just a simple plane wave as it was in the beginning with a slightly different amplitude affected by $\bar{R}'$ and propagating in the opposite direction. This is a fairly simple example, but the phase can take on complicated forms and the phase conjugating mirror will then have to implement a much more spatially-complex phase, usually implemented by a series of Zernike polynomials.

1.3.3 Micromachined Membrane Deformable Mirror

There are many ways to implement phase conjugation techniques in adaptive optics, but for the purpose of this thesis, I will focus on Micromachined Membrane Deformable Mirrors as this is the piece of equipment that we use.

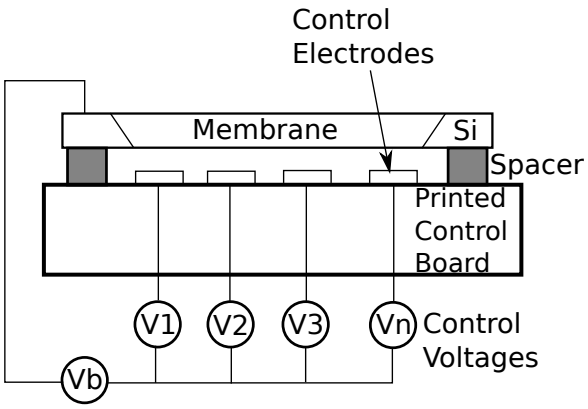

Figure 1.6: Structure of a micromachined membrane deformable mirror [51]. The voltage Vb represents the bias voltage, generally the membrane mirror is grounded. Vn is the n^{th} control voltage depending on how many actuators are in the mirror.

Micromachined membrane deformable mirrors can be made through the processes of silicon bulk micromachining [47, 48] or surface micromachining [49, 50]. Bulk micromachining involves etching away parts of a unit of substrate whereas surface micromachining involves the process of surface deposition. The structure of the mirror consists of a thin membrane (commonly made of silicon nitride), $\sim 1\mu$m thick, on a silicon chip suspended above electrodes on a printed circuit board set out in any array of patterns as determined by the manufacturer. The membrane surface is coated with a metal, aluminum in many cases, for a reflective surface which creates the mirror. The electrodes act as electrostatic actuators which pull on the membrane surface directly above them, causing the mirror to deform and change shape as in Figure 1.6

The deformation or curvature of the membrane can be described by [15]

$$\nabla^2 z(x,y) = \frac{\partial^2 z(x,y)}{\partial x^2} + \frac{\partial^2 z(x,y)}{\partial y^2} = -\frac{P(x,y)}{T}, \tag{1.21}$$

where $P(x,y)$ is the pressure at the location (x,y) and T is the tension on the membrane. The pressure is caused by the electrostatic actuator pulling on the membrane at each location. By varying the number of actuators and their layout, different patterns can be implemented onto the membrane. A common actuator pattern is a set of concentric circles, which make implementing the Zernike Polynomials quite simple.

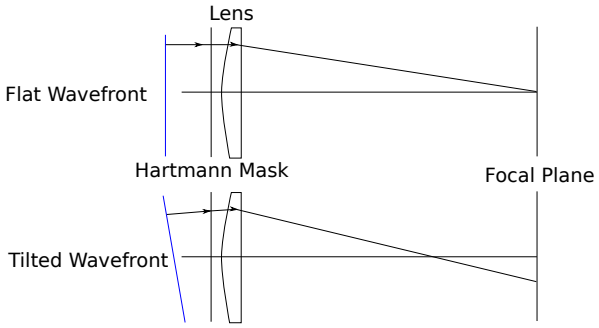

Figure 1.7: The top image shows a flat plane wavefront entering the Hartmann mask. The lens then focuses the beam onto the center of the position sensitive detector. The bottom image shows a tilted plane wavefront entering the Hartmann mask. This ray will not enter the lens parallel to the axis and will be focused onto a different location on the PSD related to the angle of arrival. This method includes the Hartmann mask and the lens added behind by Shack and Pratt in 1971.

1.3.4 Shack-Hartmann Wavefront Sensor

In order to ensure that the shape that is implemented on the wavefront is actually what is required, there must be a way to measure the wavefront. There are many techniques to accomplish this task, we use a Shack-Hartmann wavefront sensor here, thus I will limit my discussion to this device [48, 52, 53].

The original Hartmann technique was developed by J. Hartmann [54, 55] and consisted of a screen with many small holes arranged in a specific pattern which was placed in front of a position sensitive device (PSD). A lens focuses the light onto the PSD but the light passes through the mask first and when it goes through each hole it creates an array of points of light on the sensor. The location of the light on the PSD is related to the angle of the incoming wavefront when it passes through the mask. This technique did lead to a few problems such as diffraction as the beam passed through the holes.

In 1971, a technique was proposed placing lenses behind the holes and later, using an array of lenses which helped alleviate some of these problems [56]. This new sensor is known as a Shack-Hartmann wavefront sensor. Generally these masks are mounted onto a CCD camera where there are a group of pixels which are devoted to each lens in the lenslet array. These pixels measure the position of the incident light spot from a particular lenslet and once all the data is taken, a wavefront is reconstructed from the different angles where the light was detected.

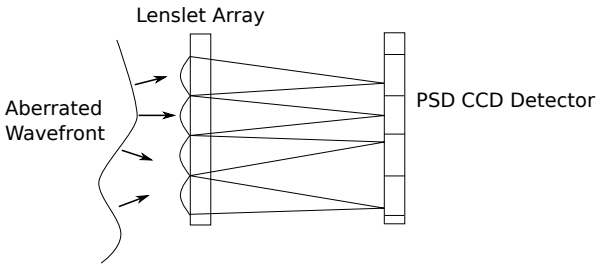

Figure 1.8: Two dimensional representation of the lenslet array showing how the different angles of arrival of the wavefront at each lens leads to a different position on the CCD detector. These positions are recorded and the wavefront is reconstructed from this data.

1.4 Spontaneous Parametric Down Conversion

The source used in Chapter 2 uses the nonlinear process of spontaneous parametric down conversion (herein referred to as SPDC) to create single photon pairs. For the purpose of this thesis, I will focus on type-II SPDC in a barium borate (BBO) crystal. For this derivation and analysis of the classical portion of the following discussion, the approach taken in [57] and [58] will be used. For the quantum portion the approach given by [59] and [60] will be used.

The starting point for this discussion will begin with Maxwell's Equations in free space ($\rho = 0$, $\mathbf{J} = 0$):

$$\nabla \cdot \mathbf{E} = 0, \tag{1.22}$$

$$\nabla \cdot \mathbf{B} = 0, \tag{1.23}$$

$$\nabla \times \mathbf{E} = -\frac{\partial \mathbf{B}}{\partial t}, \tag{1.24}$$

$$\nabla \times \mathbf{B} = \frac{1}{c^2}\frac{\partial \mathbf{E}}{\partial t}, \tag{1.25}$$

where $c = 1/\sqrt{\mu_0 \epsilon_0}$.

From these equations, we must now change them into the equations for electromagnetic waves in matter. The polarization of the fields now must be taken into account. Making the substitutions $\mathbf{D} = \epsilon_0 \mathbf{E} + \mathbf{P}$ and $\mathbf{H} = \mathbf{B}/\mu_0 + \mathbf{M}$ we now have

$$\nabla \cdot \mathbf{D} = 0, \tag{1.26}$$

$$\nabla \cdot \mathbf{B} = 0, \tag{1.27}$$

$$\nabla \times \mathbf{E} = -\frac{\partial \mathbf{B}}{\partial t}, \tag{1.28}$$

$$\nabla \times \mathbf{H} = \frac{\partial \mathbf{D}}{\partial t}, \tag{1.29}$$

where $\mathbf{P}$ and $\mathbf{M}$ are the electric and magnetic polarization vectors respectively.

We now wish to find the wave equation for homogeneous, isotropic, and non-magnetic media (that which is used in our SPDC source). To do this we apply the curl operator ($\nabla\times$) on Equation 1.28 and use Equation 1.29 and the identity $\nabla \times (\nabla \times \mathbf{E}) = \nabla(\nabla \cdot \mathbf{E}) - \nabla^2\mathbf{E}$

$$\nabla(\nabla \cdot \mathbf{E}) - \nabla^2\mathbf{E} = -\epsilon_0\mu_0\frac{\partial^2\mathbf{E}}{\partial t^2} - \mu_0\frac{\partial^2\mathbf{P}}{\partial t^2}. \tag{1.30}$$

Since we made the assumption of homogeneous and isotropic media, $\mathbf{D} = \epsilon\mathbf{E}$ which means Equation 1.26 is equivalent to $\nabla \cdot \mathbf{E} = 0$ and we can now consider the fields by separate components, Equation 1.30 simplifies to

$$\nabla^2 E - \frac{1}{c_0^2}\frac{\partial^2 E}{\partial t^2} = \mu_0\frac{\partial^2 P}{\partial t^2}, \tag{1.31}$$

and thus we have the relevant wave equation.

When light interacts with a linear medium the polarization vector goes as $\mathbf{P} = \epsilon_0\chi\mathbf{E}$ where χ is the (linear) susceptibility of the material. This in general is true even for non-linear media when $\mathbf{E}$ is sufficiently small. When $\mathbf{E}$ starts to get large in non-linear materials, $\mathbf{P}$ develops a non-linear relation to $\mathbf{E}$. Since the electric field in a non-linear media is still relatively small, $\mathbf{P}$ can be expanded in a Taylor series around $\mathbf{E} = 0$ to give

$$\mathbf{P} = \epsilon_0[\chi^{(1)}\mathbf{E} + \chi^{(2)}\mathbf{E}^2 + \cdots]. \tag{1.32}$$

For the purpose of this discussion, we will only consider second order non-linear effects.

1.4.1 Phase Matching

Consider a field with two frequency components,

$$E(t) = E(\omega_1)e^{-i\omega_1 t} + E(\omega_2)e^{-i\omega_2 t} + c.c. \tag{1.33}$$

(where "*c.c.*" represents the complex conjugate of the preceeding terms). If we consider the second order terms there are five distinct frequency combinations which come out:

$$\begin{aligned} \omega_1 + \omega_2, \quad \omega_1 - \omega_2, \\ 2\omega_1, \quad 2\omega_2, \\ 0. \end{aligned} \tag{1.34}$$

For the purpose of this section, we will focus on the $\omega_1 + \omega_2$ term which corresponds to parametric down conversion. This now gives the second order non-linear polarization component as

$$P_{NL}(\omega_3) \propto \chi^{(2)}E(\omega_1)E(\omega_2). \tag{1.35}$$

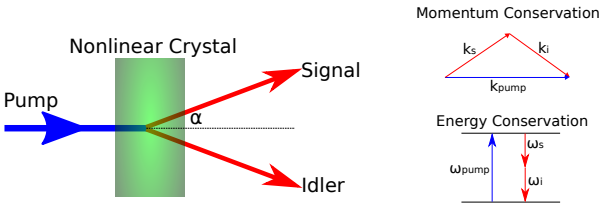

Figure 1.9: Spontaneous parametric down conversion from a nonlinear crystal. The energy and momentum phase matching conditions are illustrated to the right.

Now if we consider waves 1 and 2 to be plane waves with $\mathbf{k}_i$ ($i\epsilon\{1,2,3\}$) being their wave vectors, we have $E(\omega_i) = A_i e^{-i\mathbf{k}_i\cdot\mathbf{r}}$ and Equation 1.35 can be given as

$$P_{NL}(\omega_3) \propto \chi^{(2)} A_1 A_2 e^{-i\mathbf{k}_3\cdot\mathbf{r}}, \tag{1.36}$$

where it is important that

$$\omega_1 + \omega_2 = \omega_3, \tag{1.37}$$

$$\mathbf{k}_1 + \mathbf{k}_2 = \mathbf{k}_3, \tag{1.38}$$

so that energy and momentum are conserved. These are the frequency and phase matching conditions, which are very important, and determine what frequencies and modes can and cannot be created through the second order non-linear process described here. Although it is natural to look at the equations above and assume two waves are summed to give a third, the time reverse also holds, where one wave is split into two, given that Equations 1.37 and 1.38 are obeyed. If we think of this in light of quantum mechanics, it can be thought of as an incoming wave mixing with two vacuum states. Here the initial wave is annihilated and two single photon states are created from the vacuum states. Before we continue to the quantum analysis, let us see why it is necessary.

One more important consideration in type-II SPDC is the polarizations of the photons, which are also correlated. The main consideration for this discussion is linearly polarized light. Light which enters the crystal will be in some polarization (linear for our discussion) state which can be defined by the two components, horizontal and vertical, as seen in Figure 1.10. The state can be horizontally polarized, vertically polarized or in a superposition of both. The direction of polarization is determined by which transverse direction the electric field of the electromagnetic wave oscillates. We will define two types of polarization which are related to the optical axis of the crystal in which SPDC occurs. The field which oscillates in the direction along which the refractive index of the crystal is highest will be known as the extraordinary wave and the field which oscillates in the direction which the

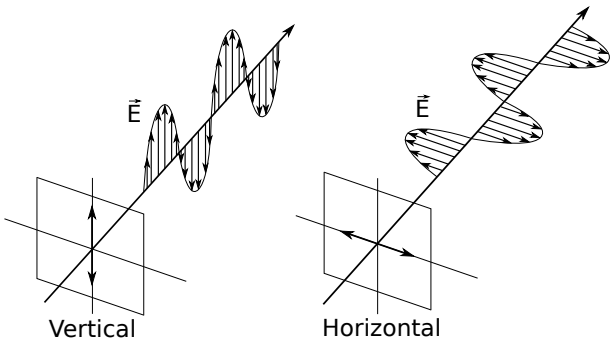

Figure 1.10: Linearly polarized light in the horizontal and vertical states. The polarization is determined by the oscillation direction of the electric field.

refractive index of the crystal is lowest will be known as the ordinary wave. (In the regime relevant to us, these two directions are orthogonal.)

For Type II SPDC, in order to meet the phase matching conditions with respect to the crystal, the polarization scheme is given as $p_e \rightarrow s_e i_o$ or $s_o i_e$. This means the pump photon should be in the extraordinary polarization state and the daughter photons will be created in opposite polarization states of each other. This can be useful for many experiments since if you know the polarization of one of the daughter photons, you automatically know the state of the other without even measuring.

1.4.2 Coupled Wave Theory

Let us now recall Equation 1.31. For simplicity the following substitution is made

$$\mathcal{S} = -\mu_0 \frac{\partial^2 P_{NL}}{\partial t^2}. \tag{1.39}$$

Remembering we are only considering second order non-linearities $P \propto \chi^{(2)} E^2$, we'll consider the electric field now as a whole to be the superposition of three waves with frequencies ω_1, ω_2, and ω_3 and complex amplitudes E_1, E_2, and E_3

$$E(t) \propto \sum_{j=\pm1,\pm2,\pm3} E_j e^{i\omega_j t}, \tag{1.40}$$

with $\omega_{-j} = -\omega_j$ and $E_{-j} = E_j^*$. If Equation 1.40 is substituted into 1.39 we get the following

$$\mathcal{S} \propto \chi^{(2)} \sum_{j,l=\pm1,\pm2,\pm3} (\omega_j + \omega_l)^2 E_j E_l e^{i(\omega_j+\omega_l)t}. \tag{1.41}$$

Putting this back into the wave equation, we find three equations similar to that of the Helmholtz equation:

$$(\nabla^2 + k_1^2)E_1 \propto \chi^{(2)}\omega_1^2 E_3 E_2^*, \tag{1.42}$$

$$(\nabla^2 + k_2^2)E_2 \propto \chi^{(2)}\omega_2^2 E_3 E_1^*, \tag{1.43}$$

$$(\nabla^2 + k_3^2)E_3 \propto \chi^{(2)}\omega_3^2 E_1 E_2. \tag{1.44}$$

This is where we find the need for the quantum mechanical description. Because we want to study SPDC, the initial conditions for this system will only have amplitude in the pump wave (say E_3). This means that all of the above equations will be identically 0 as E_1 and E_2 are zero. To resolve this issue, we move into the realm of quantum mechanics.

1.4.3 Quantum Description of SPDC

Let us now consider instead of classical waves, light as photons. In order to fully describe SPDC we need to consider the quantum vacuum fluctuations of input modes. This quantum mechanical property cannot be explained in classical physics but leads to spontaneous parametric down conversion which is the creation of two lower energy photons from one higher-energy photon. Historically, the two photons created from SPDC are known as the signal and the idler photons. The pump mode will begin as a strong, single-mode coherent state, $|\alpha\rangle_p$. The signal and idler modes will begin in the vacuum state. The interaction Hamiltonian which couples the three fields is given as

$$\mathcal{H}_{\text{int}} = -\frac{\epsilon_0}{3}\chi^{(2)} \int_V \mathrm{d}V E_s^{(-)} E_i^{(-)} E_p^{(+)} + E_p^{(-)} E_s^{(+)} E_i^{(+)}, \tag{1.45}$$

where the electric field operators are given by

$$E_n^{(+)} = i\sqrt{\frac{\hbar\omega_n}{2\epsilon_0 V}} a_n e^{-i(\omega_n t + k_n z)}, \quad E_n^{(-)} = -i\sqrt{\frac{\hbar\omega_n}{2\epsilon_0 V}} a_n^\dagger e^{i(\omega_n t - k_n z)}. \tag{1.46}$$

In these operators, a_n is the annihilation operator for the n^{th} state and $a_n^\dagger$ is the creation operator for the n^{th} state. From the Hamiltonian it is obvious that the second term will not contribute to this process as there are annihilation operators acting on the vacuum state which gives $a|0\rangle = 0$. Acting the Hamiltonian on the state, it evolves as

$$\begin{aligned} |\psi(t)\rangle &= e^{-i\mathcal{H}_{int}t/h} |0\rangle_s |0\rangle_i |\alpha\rangle_p \\ &= |0\rangle_s |0\rangle_i |\alpha\rangle_p + \frac{it\epsilon_0\chi^{(2)}}{3\hbar} \int_0^t \mathrm{d}t' \int_V \mathrm{d}V E_s^{(-)} E_i^{(-)} E_p^{(+)} |0\rangle_s |0\rangle_i |\alpha\rangle_p + \cdots \end{aligned} \tag{1.47}$$

where the other terms are ignored as we will work to first order for simplicity. Thus,

$$\begin{aligned}
|\psi(t)\rangle &\approx \int_0^t \mathrm{d}t' \int_V \mathrm{d}V E_s^{(-)} E_i^{(-)} E_p^{(+)} |0\rangle_s |0\rangle_i |\alpha\rangle_p \\
&\approx \frac{it\epsilon_0\chi^{(2)}}{3\hbar}\sqrt{\frac{\hbar^3}{2\epsilon^3 V^3}}\sqrt{\omega_i\omega_s\omega_p} \\
&\quad \int_0^t \mathrm{d}t' \int_V \mathrm{d}V a_s^\dagger e^{i(\omega_s t' - k_s z)} a_i^\dagger e^{i(\omega_i t' - k_i z)} a_p e^{-i(\omega_p t' - k_p z)} |0\rangle_s |0\rangle_i |\alpha\rangle_p .
\end{aligned} \tag{1.48}$$

Now the prefactors will be dropped for simplicity so the action of the raising and lowering operators can be seen.

$$\begin{aligned}
|\psi(t)\rangle &\propto \int_0^t \mathrm{d}t' \int_V \mathrm{d}V a_s^\dagger e^{i(\omega_s t' - k_s z)} a_i^\dagger e^{i(\omega_i t' - k_i)} a_p e^{-i(\omega t' - k_p z)} |0\rangle_s |0\rangle_i |\alpha\rangle_p \\
&\propto \int_0^t \mathrm{d}t' \int_V \mathrm{d}V \alpha e^{i(\omega_s+\omega_i-\omega_p)t'} e^{-i(k_s+k_i-k_p)z} |1\rangle_s |1\rangle_i |\alpha\rangle_p .
\end{aligned} \tag{1.49}$$

where $a^\dagger |0\rangle = |1\rangle$ and $a|\alpha\rangle = \alpha|\alpha\rangle$. From this it can be seen that one pump photon has been annihilated and the signal and idler photons have been created. If the interaction time is assumed to be very long in comparison to the optical frequencies, the temporal integral can be approximated as

$$\lim_{t\to\infty} \int_0^t \mathrm{d}t' e^{-i(-\omega_s-\omega_i+\omega_p)t'} = 2\pi\delta(\omega_s+\omega_i-\omega_p). \tag{1.50}$$

This equation shows the energy conservation ($\omega_p = \omega_s + \omega_i$) brought out from the quantum calculations. This is the same energy conservation as shown in Equation 1.37. The pump photon frequency was fixed when we made the assumption about the single mode coherent state, but the signal and idler frequencies are left open. They can be determined by the phase matching conditions of the crystal used for SPDC, and for the experiment in Chapter 2 they will be degenerate, i.e. $\omega_s = \omega_i$.

To look at the spatial integral, first assume that the volume where the interaction takes place is bounded by L_x, L_y, and L_z. The integral is given as

$$\int_V \mathrm{d}V e^{i(-\mathbf{k}_s-\mathbf{k}_i+\mathbf{k}_p)\cdot\mathbf{r}}, \tag{1.51}$$

where $\mathbf{r}$ is the three dimensional spatial coordinate vector. This integral is maximized when

$$\Delta k = k_p - k_i - k_s = 0. \tag{1.52}$$

To observe the effects of not having $\Delta k = 0$ we will take the integral over one spatial direction to see what arises:

$$\int_0^{L_y} \mathrm{d}y e^{-i\Delta k_y y} = -\frac{i}{\Delta k_y}(1 - e^{-i\Delta k_y L_y}) \tag{1.53}$$

$$= e^{-\frac{i\Delta k_y L_y}{2}} L_y \mathrm{sinc}\left(\frac{\Delta \mathrm{k_y L_y}}{2}\right). \tag{1.54}$$

This shows that as the k vectors move away from perfect phase matching, the SPDC process falls off as a sinc function. Equations 1.50 and 1.52 are the same phase matching and energy and momentum conserving functions as those obtained when treating the process of SPDC classically.

1.5 Discussion

Through the sections above, I have explored some disparate theories and models, all of which will be necessary in following chapters. The scope of this thesis is the study of acquisition, pointing and tracking systems for a QKD satellite and the effects which could cause problems. Thus we can tie the study of atmospheric turbulence and adaptive optics together (although this may have been obvious already). The study of SPDC is here as we would like to see if a new pointing technique can be achieved by understanding the spatial correlations in this process. This also brings together adaptive optics and SPDC since we would like to manipulate the pump with equipment generally used in adaptive optics. Throughout this thesis, these topics will be touched upon again and the theories studied here will be applied.

Chapter 2

Spatial Correlations in Spontaneous Parametric Down Conversion

As discussed in Chapter 1, a satellite uplink comes with many problems due to atmospheric turbulence. Adaptive optics is a very promising technique that can be used to help solve some of these problems. In order to implement adaptive optics on the pump beam, which is well defined in polarization and is local and easy to operate on, we need to understand how manipulation of the pump beam wavefront affects the photons created through SPDC. We need to understand two main concepts, first of all we need to know how the mode transfer works between the pump beam and the created daughter beams. Second of all we would like to know how changing the pump beam affects the spatial correlations of the daughter photons. The second idea mentioned will be studied more thoroughly in this chapter.

2.1 Momentum-Position Studies of the SPDC Photons

As we saw in Section 1.4, momentum conservation is an important aspect of SPDC. The spatial correlations between photons created through SPDC have been studied in many different ways [61–66] and many experiments have been implemented to test out various properties such as improving coincidence rates [67], testing the EPR paradox [68], and image formation [69].

The correlations between the pump, signal, and idler photons are fairly well modeled and we are reminded that

$$\mathbf{k}_p = \mathbf{k}_s + \mathbf{k}_i. \tag{2.1}$$

The bi-photon state which is created through SPDC also takes into account many other parameters such as the crystal length that SPDC occurs in, the size of the waist of the pump beam as well as the optical axis of the crystal which can help determine the spreading angle of the down converted photons. The experiment detailed in this chapter aims to explore the spatial properties of the down converted photons and their relation to the pump beam. It will begin with a theoretical model study of the state created in SPDC and then numerical simulations are conducted to observe the correlations. The experiment attempts to verify the model proposed in the following section and determine the usefulness of these findings.

2.2 Theoretical and Numerical Models of SPDC Spatial Correlations

2.2.1 Spectrally Single Mode

The energy and momentum conservation conditions upheld by SPDC are the basis to study the spatial correlations here. We would like to find an approximate analytical condition which demonstrates the strength of the spatial correlations between the daughter photons in SPDC. We would also like to find the effects of the pump laser on the down converted photons. We will begin by looking at the bi-photon wave function as given by [70, 71]

$$\psi(\mathbf{k}_{s\perp},\omega_s;\mathbf{k}_{i\perp},\omega_i)=\frac{\mathcal{N}L}{2}A_p(\mathbf{k}_{s\perp}+\mathbf{k}_{i\perp},\omega_s+\omega_i)\mathrm{sinc}\left(\Delta\mathrm{k_z}(\mathbf{k_{s\perp}},\omega_\mathrm{s};\mathbf{k_{i\perp}},\omega_\mathrm{i})\frac{\mathrm{L}}{2}\right), \tag{2.2}$$

where $\mathcal{N}$ is a normalization constant to be determined further on, L is the length of the crystal and A_p is the pump amplitude function. We will assume that the pump amplitude function is in a factorable form, where there are no spatiotemporal correlations

$$A_p(\mathbf{k}_\perp,\omega)=A_p^{\mathrm{temp}}(\omega)A_p^{\mathrm{sp}}(\mathbf{k}_\perp), \tag{2.3}$$

Both parts of this function will be taken in a Gaussian form

$$A_p^{\mathrm{temp}}(\omega) = \frac{\sqrt{\tau_p}}{\sqrt[4]{\pi}}\exp\left(-\frac{\tau_p^2}{2}(\omega-2\omega_0)^2\right), \tag{2.4}$$

$$A_p^{\mathrm{sp}}(\mathbf{k}_\perp) = \frac{\omega_p}{\sqrt{\pi}}\exp\left(-\frac{\omega_p^2}{2}\mathbf{k}_\perp^2\right). \tag{2.5}$$

To simplify the model, we will use a Gaussian approximation of the sinc function [72, 73]

$$\mathrm{sinc}x\approx\exp(-\frac{1}{5}x^2), \tag{2.6}$$

which now allows us to write the bi-photon wavefunction as

$$\Psi(\mathbf{k}_{s\perp},\omega_s;\mathbf{k}_{i\perp},\omega_i)=\frac{\mathcal{N}L}{2}A_p^{temp}(\omega_s+\omega_i)A_p^{sp}(\mathbf{k}_{s\perp}+\mathbf{k}_{i\perp})e^{\Delta k_z(\mathbf{k}_{s\perp},\omega_s;\mathbf{k}_{i\perp},\omega_i)\frac{L}{2}}. \tag{2.7}$$

We now must work with the phase mismatch, Δk_z, to find a form which matches our wavefunction. We know from Chapter 1 that the phase mismatch is given as

$$\Delta\mathbf{k}=\mathbf{k}_{p\perp}-\mathbf{k}_{s\perp}-\mathbf{k}_{i\perp}. \tag{2.8}$$

We will choose perfect phase matching of the pump photon frequency to be $\omega_p=2\omega_0$ and it will propagate along the z axis, $\mathbf{k}_{p\perp}=0$. The signal and idler photons will be given as $\omega_s=\omega_i=\omega_0$ and will propagate at an angle α with respect to the z axis. The directions of these photons will then be given by $\mid\mathbf{k}_{s0\perp}\mid=\mid\mathbf{k}_{i0\perp}\mid=\frac{\omega_0}{c}\sin(\alpha)$ and moving away from each other (note for the remainder of this discussion, we will assume $c=1$). With these conditions in mind, the phase matching becomes

$$\Delta k_z(\mathbf{k}_{s0\perp},\omega_0;\mathbf{k}_{i0\perp},\omega_0)=k_{pz}(\mathbf{k}_{s0\perp}+\mathbf{k}_{i0\perp},2\omega_0)-k_{sz}(\mathbf{k}_{s0\perp},\omega_0)-k_{iz}(\mathbf{k}_{i0\perp},\omega_0)=0. \tag{2.9}$$

Because the phase matching function includes a Gaussian wave form (in the pump mode) the phase matching function will disappear very quickly as one moves away from the ideal collection positions. We will therefore make the paraxial approximation to the phase mismatch which will give the following form

$$\Delta k_z(\mathbf{k}_{s\perp},\omega_s;\mathbf{k}_{i\perp},\omega_i)\approx d_s(\omega_s,\omega_i)(\mathbf{k}_{s\perp}-\mathbf{k}_{s_0\perp})+d_i(\omega_s,\omega_i)(\mathbf{k}_{i\perp}-\mathbf{k}_{s_0\perp}), \tag{2.10}$$

where

$$d_\mu(\omega_s,\omega_i)=\left.\frac{\partial\Delta k_z(\mathbf{k}_{s\perp},\omega_s;\mathbf{k}_{i\perp},\omega_i)}{\partial k_{\mu y}}\right|_{\substack{\mathbf{k}_{s\perp}=\mathbf{k}_{s0\perp}\\ \mathbf{k}_{i\perp}=\mathbf{k}_{i0\perp}}},\quad \mu=s,i \tag{2.11}$$

(note: we will simplify the discussion further by only discussing correlations in the y direction).

Now we can re-write the bi-photon wave function in closed form

$$\begin{aligned}\psi(\mathbf{k}_{s\perp},\omega_s;\mathbf{k}_{i\perp},\omega_i) &= \frac{\mathcal{N}L}{2}A_p^{\text{temp}}(\omega_s+\omega_i)\\ &\times \exp\left(-\frac{w_p^2}{2}(\mathbf{k}_{s\perp}+\mathbf{k}_{i\perp})^2-\frac{L^2}{10}(d_s(\mathbf{k}_{s\perp}-\mathbf{k}_{s_0\perp})+d_i(\mathbf{k}_{i\perp}-\mathbf{k}_{i_0\perp}))^2\right).\end{aligned} \tag{2.12}$$

Because the pump source in this experiment will be a continuous wave laser, one more simplification can take place. With a continuous wave laser we have the conservation of energy in the simple form $\omega_p=\omega_s+\omega_i$ which then gives

$$A_p^{temp}(\omega_p,\omega_s,\omega_i)=\delta(\omega_p-\omega_s-\omega_i). \tag{2.13}$$

As a first step to observe the correlations, the bi-photon wave function given in Equation 2.12 with the simplification in Equation 2.13 is compared to the bivariate normal distribution probability density function

$$f(x,y) = \frac{1}{2\pi\sigma_x\sigma_y\sqrt{1-\rho^2}} \exp\left(-\frac{1}{2(1-\rho^2)}\left(\frac{x^2}{\sigma_x^2} + \frac{y^2}{\sigma_y^2} - \frac{2\rho xy}{\sigma_x\sigma_y}\right)\right), \tag{2.14}$$

where ρ is the correlation factor. Again only operating on correlations in the y direction gives

$$\rho_y^2 = \frac{(w_p^2 + \frac{1}{5}L^2 d_{sy} d_{iy})^2}{(w_p^2 + \frac{1}{5}L^2 d_{sy}^2)(w_p^2 + \frac{1}{5}L^2 d_{iy}^2)}. \tag{2.15}$$

From this function, we can see that there will be no correlations as the numerator vanishes ($\rho_y \to 0$), but it is easy to see that when $d_{sy} = d_{iy}$ there are perfect correlations ($\rho_y = 1$). To make this a little more explicit

$$\frac{\partial \Delta k_z(\mathbf{k}_{s\perp}, \omega_s; \mathbf{k}_{i\perp}, \omega_i)}{\partial k_{sy}} = \frac{\partial \Delta k_z(\mathbf{k}_{s\perp}, \omega_s; \mathbf{k}_{i\perp}, \omega_i)}{\partial k_{iy}}. \tag{2.16}$$

This would mean that in Type I degenerate frequency down conversion, the spatial correlation is perfect since the left and right sides are the same. Although this does not hold for Type II, it is very close.

2.2.2 Spectrally Multimode

Up until now we have assumed that the down converted photons were spectrally multimode i.e. $\omega_s = \omega_i = \omega_0$ exactly. We will now take into account a spreading of the frequencies of the signal and idler frequencies. We still must use the condition that $\omega_i = \omega_p - \omega_s$ since this is energy conservation and cannot be violated. The phase mismatch can now be approximated up to first order in frequency as well as transverse wave vectors

$$\Delta k_z(\mathbf{k}_{s\perp}, \omega_s; \mathbf{k}_{i\perp}, \omega_i) \approx \beta_s(\omega_s - \omega_0) + \beta_i(\omega_0 - \omega_s) + d_s(\omega_s, \omega_i)(\mathbf{k}_{s\perp} - \mathbf{k}_{s_0\perp}) + d_i(\omega_s, \omega_i)(\mathbf{k}_{i\perp} - \mathbf{k}_{i_0\perp}), \tag{2.17}$$

where ω_0 is the signal photon central frequency. The term $\beta_s = \left.\frac{\partial \Delta k_z(\mathbf{k}_{s\perp}, \omega_s; \mathbf{k}_{i\perp}, \omega_i)}{\partial \omega_s}\right|_{\substack{\omega_s = \omega_0 \\ \omega_i = \omega_0}}$ and similar for β_i. Now, the bi-photon density matrix can be written as

$$\begin{aligned} \rho(\mathbf{k}_{s\perp}, \mathbf{k}_{i\perp}; \mathbf{k}'_{s\perp}, \mathbf{k}'_{i\perp}) &= \left(\frac{\mathcal{N}L}{2}\right) A_p^{sp}(\mathbf{k}_{s\perp} + \mathbf{k}_{i\perp}) A_p^{sp}(\mathbf{k}'_{s\perp} + \mathbf{k}'_{i\perp}) \\ &\times \int \mathrm{d}\omega_s \mathrm{sinc}\left(\frac{1}{2}L\Delta k_z\right) \mathrm{sinc}\left(\frac{1}{2}L\Delta k'_z\right). \end{aligned} \tag{2.18}$$

Using the following relation which was found by Dr. Piotr Kolenderski to apply especially well to these circumstances (not a universal expression)

$$\int_{-\infty}^{\infty} \mathrm{sinc}(ax+b)\mathrm{sinc}(cx+d) \approx \frac{\pi}{\mid c \mid} \mathrm{sinc}\left(\frac{ad-bc}{c}\right), \tag{2.19}$$

the result of Equation 2.18 is

$$\rho(\mathbf{k}_{s\perp}, \mathbf{k}_{i\perp}; \mathbf{k}'_{s\perp}, \mathbf{k}'_{i\perp}) = \left(\frac{\mathcal{N}L}{2}\right) \frac{2\pi}{\mid L\beta \mid} A_p^{sp}(\mathbf{k}_{s\perp} + \mathbf{k}_{i\perp}) A_p^{sp}(\mathbf{k}'_{s\perp} + \mathbf{k}'_{i\perp}). \tag{2.20}$$

This shows that correlations between the propagation directions of the signal and idler photons depend on the characteristics of the pump beam, mainly in this case the beam width.

2.2.3 Numerical Modeling

The first step that must be taken is to calculate the cut angle of the crystal for our wavelength and spread angle criterion. We will be modeling a system which has a central down conversion wavelength of 810nm and a spread angle relative to the z axis of 3 degrees. To do this, we require the phase mismatch function Δk_z. From Chapter 1 and the above section, we end up with

$$
\begin{aligned}
\Delta k_z(k_{sx}, k_{sy}, k_{ix}, k_{iy}, \omega_s, \omega_i, \theta) &= \frac{(k_{sx}+k_{ix})\sin(\theta)\cos(\theta)(1-\frac{n_e(\omega_s+\omega_i)}{n_o(\omega_s+\omega_i)})}{\sin^2(\theta)+\frac{n_e(\omega_s+\omega_i)}{n_o(\omega_s+\omega_i)}\cos^2(\theta)} \\
&+ \frac{\sqrt{((\omega_s+\omega_i)^2 n_e(\omega_s+\omega_i)-(k_{sy}+k_{iy})^2)\left(\sin^2(\theta)+\frac{n_e(\omega_s+\omega_i)}{n_o(\omega_s+\omega_i)}\cos^2(\theta)\right)-\frac{n_e(\omega_s+\omega_i)}{n_o(\omega_s+\omega_i)}(k_{sx}+k_{ix})^2}}{\sin^2(\theta)+\frac{n_e(\omega_s+\omega_i)}{n_o(\omega_s+\omega_i)}\cos^2(\theta)} \\
&- \sqrt{\omega_s^2 n_o(\omega_s)-k_{sx}^2-k_{sy}^2}-\frac{k_{ix}\sin(\theta)\cos(\theta)\left(1-\frac{n_e(\omega_i)}{n_o(\omega_i)}\right)}{\sin^2(\theta)+\frac{n_e(\omega_i)}{n_o(\omega_i)}\cos^2(\theta)} \\
&- \frac{\sqrt{(\omega_i^2 n_e(\omega_i)-k_{iy}^2)\left(\sin^2(\theta)+\frac{n_e(\omega_i)}{n_o(\omega_i)}\cos^2(\theta)\right)-\frac{n_e(\omega_i)}{n_o(\omega_i)}k_{ix}^2}}{\sin^2(\theta)+\frac{n_e(\omega_i)}{n_o(\omega_i)}\cos^2(\theta)}, \qquad (2.21)
\end{aligned}
$$

where

$$
n_o(\omega) = 2.7359 + \frac{0.01878}{\left(\frac{2\pi}{\omega}\right)^2 - 0.01822} - 0.01471\left(\frac{2\pi}{\omega}\right)^2 + 0.0006081\left(\frac{2\pi}{\omega}\right)^4 - 0.00006740\left(\frac{2\pi}{\omega}\right)^6, \qquad (2.22)
$$

$$
n_e(\omega) = 2.3753 + \frac{0.01224}{\left(\frac{2\pi}{\omega}\right)^2 - 0.01667} - 0.01627\left(\frac{2\pi}{\omega}\right)^2 + 0.0005716\left(\frac{2\pi}{\omega}\right)^4 - 0.00006305\left(\frac{2\pi}{\omega}\right)^6, \qquad (2.23)
$$

are the Sellmeier equations for BBO and wavelength is in micrometers.

To find what cut angle yields the maximized phase matching conditions, we plot the sinc function from Equation 2.2 as a function of θ as seen in Figure 2.1. The function

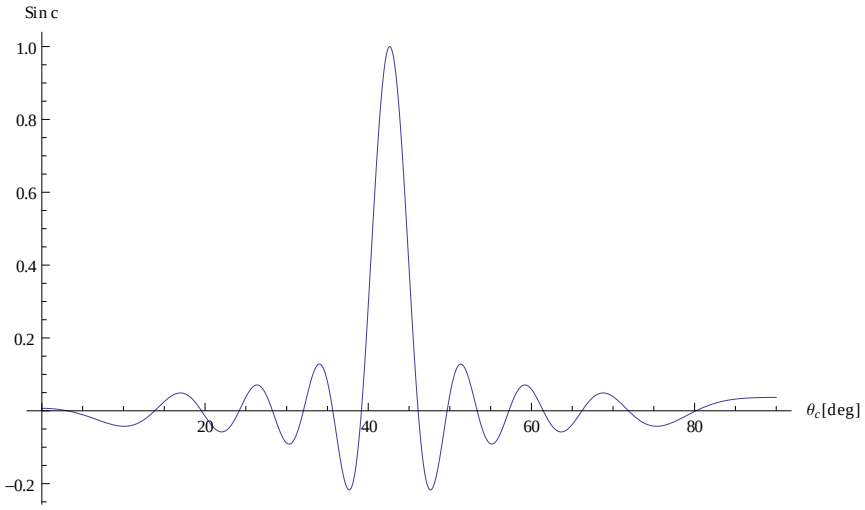

Figure 2.1: Sinc function showing the optimal cut angle for the parameters chosen at 42.632°. This comes from the phase matching function Δk.

ends up being maximized with a cut angle of 42.632 degrees. Although L appears in the sinc function argument, it has negligible impact on the calculation for the cut angle of the crystal. For this calculation, a value of 1000μm was used.

Now to observe visually the correlations between the signal and idler photons, the pump profile as well as that of the crystal must be combined. To create a 2-dimensional representation of the crystal profile, a table of values of the sinc function with respect to k_{iy} and k_{sy} will be made over some range of values around the spread angle of 3 degrees. Now L does have a significant impact on the profile of the crystal and therefore must be taken into account. Three profiles with three different crystal lengths are shown in Figure 2.2.

To make the pump profile we use the Gaussian profile shape given as

$$P(k_{px}, k_{py}, w_p) = e^{-\frac{w_p^2}{2}(k_{px}^2+k_{py}^2)}. \tag{2.24}$$

Again we make a 2-dimensional plot over k_{px} and k_{py} for different pump widths. These profiles can be seen in Figure 2.3.

By now multiplying these "masks" together, the directional correlations will be revealed. Figure 2.4 shows the correlations with various pump sizes and crystal lengths as shown above. The correlation factors shown in Table 2.1 are $(1-\rho)$ from above, and therefore lower numbers have higher correlations.

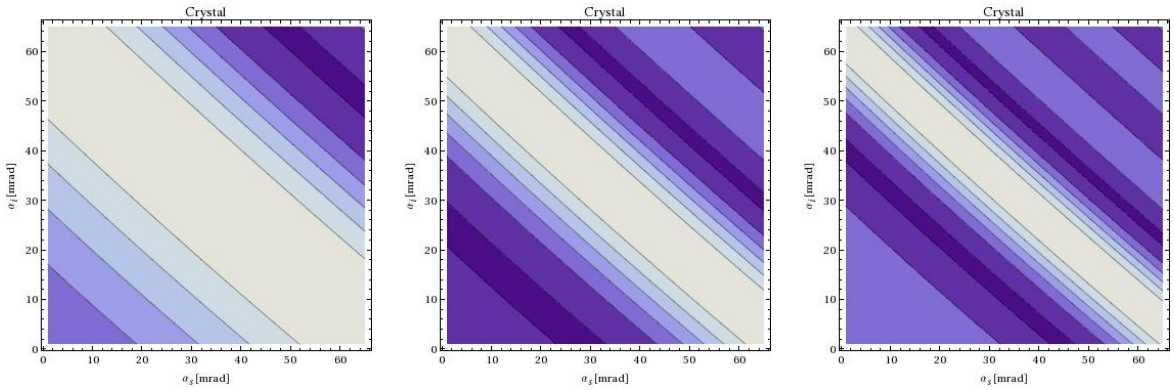

Figure 2.2: These images represent the crystal phase matching "mask" for three different crystal lengths, 500μm, 1000μm and 1500μm.

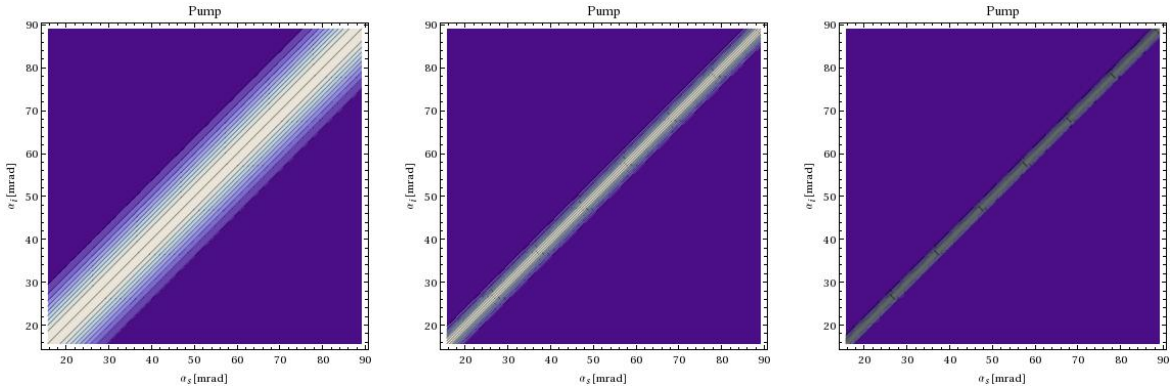

Figure 2.3: These images represent the pump beam phase matching "mask" for three different waist diameters, 20μm, 70μm, and 150μm.

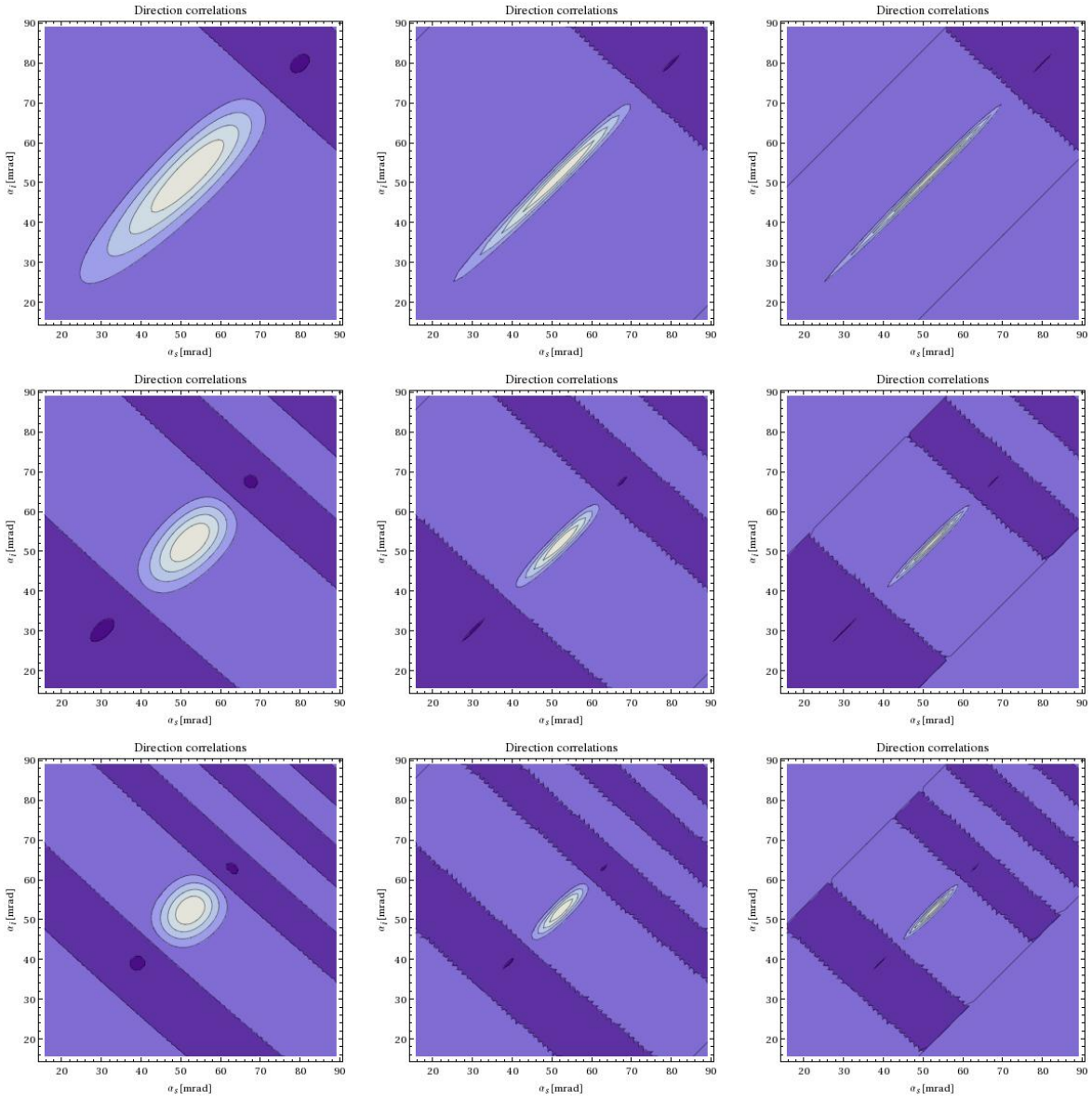

Figure 2.4: Directional correlations for varying pump waist size and crystal length. Table 2.1 lists the correlation factors for the various examples. From the pictorial representation it is obvious that with reducing the length of the crystal and increasing the pump beam waist, the correlations grow stronger. (Beam waist increases to the right and crystal length increases going down)

Beam Width → Crystal Length ↓	$20\mu m$	$70\mu m$	$150\mu m$
$500\mu m$	0.32	0.63	0.75
$1000\mu m$	0.15	0.49	0.65
$1500\mu m$	0.09	0.39	0.58

Table 2.1: Correlation values for the various cases in Figure 2.4. From this data the beam with the largest waist and the smallest crystal length creates the strongest correlations.

Now we want to develop a function which will give us the probabilities of measuring the signal photon on an array of photon detectors given the measurement of the idler photon collected by a fiber. Initially, we begin with the square of the bi-photon wave function, Equation 2.12, including the spectrally multimode phase mismatch, Equation 2.17 given as

$$\begin{aligned} \mid \Psi(\mathbf{k}_{s\perp}, \omega_s; \mathbf{k}_{i\perp}, \omega_i) \mid^2 &= \mathcal{N} \exp\left(-w_p^2(k_{sy} + k_{iy})^2\right. \\ &- \frac{L^2}{5}(d_s(k_{sy} - k_{sy0}) + d_i(k_{iy} - k_{iy0}) + \beta_s(\omega_s - \omega_0) + \beta_i(\omega_0 - \omega_s))^2 \\ &- \left.\frac{(2\omega_0 - \omega_s - p)^2}{j^2}\right). \end{aligned} \tag{2.25}$$

The last term in the expression given in Equation 2.25 is added since the idler photon goes through a frequency filter. This filter is centered at 810nm and has a FWHM of 10nm. The values of p and j are determined by a Gaussian fit to the experimentally measured data obtained from the Thorlabs website. To make our calculations simpler, a model is generated which will make the integration faster and simpler, then the appropriate substitutions will be made. The model used is given here

$$\begin{aligned} \mid \Psi(\mathbf{k}_{s\perp}, \omega_s; \mathbf{k}_{i\perp}, \omega_i) \mid^2 &= \exp(-ak_{iy}^2 - bk_{iy} - ck_{iy}k_{sy} - dk_{sy} - mk_{sy}^2 \\ &- fk_{iy}\omega_s - g\omega_s - hk_{sy}\omega_s - n\omega_s^2 + t), \end{aligned} \tag{2.26}$$

where t is the normalization consideration. Using a coefficient list function in Mathematica,

the values of each of these variables is determined and listed in Equation 2.27.

$$
\begin{aligned}
a &= -\left(-w_p^2 - \frac{L^2 d_i^2}{5}\right), \\
b &= -\left(\frac{2}{5} L^2 d_i (k_{sy0} d_s + k_{iy0} d_i + (-\beta_i + \beta_s)\omega_0)\right), \\
c &= -\left(-\frac{2}{5}(5w_p^2 + L^2 d_s d_i)\right), \\
d &= -\left(\frac{2}{5} L^2 d_s (k_{sy0} d_s + k_{iy0} d_i + (-\beta_i + \beta_s)\omega_0)\right), \\
m &= -\left(-w_p^2 - \frac{L^2 d_s^2}{5}\right), \\
f &= -\left(\frac{2}{5}(\beta_i - \beta_s) L^2 d_i\right), \\
g &= -\left(\frac{2(5p + (\beta_i - \beta_s) j^2 L^2 (-k_{sy0} d_s - k_{iy0} d_i + \beta_i \omega_0 - \beta_s \omega_0))}{5j^2}\right), \\
h &= -\left(\frac{2}{5}(\beta_i - \beta_s) L^2 d_s\right), \\
n &= -\left(-\frac{1}{j^2} - \frac{1}{5}(\beta_i - \beta_s)^2 L^2\right), \\
j &= \left(\frac{2\pi}{36}\right) / 2.35482, \\
p &= 7.78, \\
t &= -\frac{5p^2 - 20p\omega_0 + 20\omega_0^2 + j^2 L^2 (k_{sy0} d_s + k_{iy0} d_i - \beta_i \omega_0 + \beta_s \omega_0)^2}{5j^2}.
\end{aligned}
\tag{2.27}
$$

We also must now take the derivatives of the phase matching function with respect to

k_{sy}, k_{iy}, ω_s, and ω_i to insert into the equation

$$d_s(k_{sy0}, k_{iy0}, \omega_0, \theta) = \frac{k_{sy0}}{\sqrt{-k_{sy0}^2 + \omega_0^2 n_o(\omega_0)}} - \frac{k_{iy0} + k_{sy0}}{\sqrt{(-(k_{iy0} + k_{sy0})^2 + 4\omega_0^2 n_e(2\omega_0)) \left(\frac{\cos^2(\theta) n_e(2\omega_0)}{n_o(2\omega_0)} + \sin^2(\theta)\right)}}, \tag{2.28}$$

$$d_i(k_{sy0}, k_{iy0}, \omega_0, \theta) = \frac{k_{iy0}}{\sqrt{(-k_{iy0}^2 + \omega_0^2 n_e(\omega_0) \left(\frac{\cos^2(\theta) n_e(2\omega_0)}{n_o(2\omega_0)} + \sin^2(\theta)\right)}} - \frac{k_{iy0} + k_{sy0}}{\sqrt{(-(k_{iy0} + k_{sy0})^2 + 4\omega_0^2 n_e(2\omega_0)) \left(\frac{\cos^2(\theta) n_e(2\omega_0)}{n_o(2\omega_0)} + \sin^2(\theta)\right)}}, \tag{2.29}$$

$$
\begin{aligned}
\beta_s(k_{sy0}, k_{iy0}, \omega_0, \theta) &= -\frac{2\omega_0 n_o(\omega_0) + \omega_0^2 n_o'(\omega_0)}{2\sqrt{-k_{sy0}^2 + \omega_0^2 n_o(\omega_0)}} \\
&- \frac{\left(\sqrt{(-(k_{iy0}+k_{sy0})^2 + 4\omega_0^2 n_e(2\omega_0))\left(\frac{\cos^2(\theta) n_e(2\omega_0)}{n_o(2\omega_0)} + \sin^2(\theta)\right)}\left(\frac{\cos^2(\theta) n_e'(2\omega_0)}{n_o(2\omega_0)} - \frac{\cos^2(\theta) n_e(2\omega_0) n_o'(2\omega)}{n_o^2(2\omega_0)}\right)\right)}{\left(\frac{\cos^2(\theta) n_e(2\omega_0)}{n_o(2\omega_0)} + \sin^2(\theta)\right)^2} \\
&+ \frac{\left(\left(\frac{\cos^2(\theta) n_e(2\omega_0)}{n_0(2\omega_0)} + \sin^2(\theta)\right)(4\omega_0 n_e(2\omega_0) + 4\omega_0^2 n_e'(2\omega_0)) + (-(k_{iy0}+k_{sy0})^2 + 4\omega_0^2 n_e(2\omega_0))\left(\frac{\cos^2(\theta) n_e'(2\omega_0)}{n_o(2\omega_0)} - \frac{\cos^2(\theta) n_e(2\omega_0) n_o'(2\omega_0)}{n_o^2(2\omega_0)}\right)\right)}{\left(2\left(\frac{\cos^2(\theta) n_e(2\omega_0)}{n_o(2\omega_0)} + \sin^2(\theta)\right)\sqrt{(-(k_{iy0}+k_{sy0})^2 + 4\omega_o^2 n_e(2\omega_0))\left(\frac{\cos^2(\theta) n_e(2\omega_0)}{n_o(2\omega_0)} + \sin^2(\theta)\right)}\right)}.
\end{aligned}
\tag{2.30}
$$

Note: In this form β_i is the exact same. The difference comes when taking the derivative before the substitution. Notice in the above expression that there are terms given as $n_{o\,\mathrm{or}\,e}'(\omega_o)$ or $n_{o\,\mathrm{or}\,e}'(2\omega_o)$. These terms will be different depending on whether ω_s or ω_i were in the initial arguments. For simplicity we will keep the above term as is, but keep this note in mind.

To find the probability density function of finding a photon on the signal side, given the collection of a photon on the idler side at k-vector k_{ic} with spread δk due to the finite size of the fiber, we integrate the model function given in Equation 2.26 over k_{iy} from $k_{ic} - \frac{\delta k}{2}$ to $k_{ic} + \frac{\delta k}{2}$ and over ω_s from $-\infty$ to ∞ which yields:

$$\begin{aligned} P(k_{sy}, L, w_p) &= \frac{\mathcal{N}}{\sqrt{-f^2+4an}} \exp\left(\frac{b^2 n + df^2 k_{sy} - cfgk_{sy} + mf^2 k_{sy}^2}{-f^2+4an}\right) \\ &\times \exp\left(\frac{-cfhk_{sy}^2 + c^2 n k_{sy}^2 - b(-2cnk_{sy} + f(g+hk_{sy})) - f^2 t}{-f^2+4an}\right) \\ &\times \exp\left(\frac{a(g^2 + 2ghk_{sy} - 4dnk_{sy} + h^2 k_{sy}^2 - 4mnk_{sy}^2 + 4nt)}{-f^2+4an}\right) \\ &\times \pi\left(-\mathrm{Erf}\left(\frac{-2f(g+hk_{sy}) + f^2(-2k_{ic}+\delta k) + 4n(b+2ak_{ic}+ck_{sy}-a\delta k)}{4\sqrt{n}\sqrt{-f^2+4an}}\right)\right. \\ &+ \left.\mathrm{Erf}\left(\frac{-2f(g+hk_{sy}) - f^2(2k_{ic}+\delta k) + 4n(b+2ak_{ic}+ck_{sy}+a\delta k)}{4\sqrt{n}\sqrt{-f^2+4an}}\right)\right), \end{aligned} \tag{2.31}$$

where

$$\mathcal{N} = \frac{\sqrt{4a - \frac{f^2}{n}}\sqrt{n}\sqrt{\frac{mf^2 - cfh + ah^2 + c^2 n - 4amn}{f^2\pi - 4an\pi}}}{2\pi e^{\frac{c^2 g^2 - 4amg^2 + b(4mfg - 2cgh) + d^2(f^2-4an) - 2d(cfg + bfh - 2agh - 2bcn) + b^2(h^2-4mn) + 4mf^2 t - 4cfht + 4ah^2 t + 4c^2 nt - 16amnt}{4(-cfh + ah^2 + c^2 n + m(f^2-4an))}}}. \tag{2.32}$$

To make this function slightly more useful, we will convert it to be in terms of horizontal distance to match with positions on the single photon detector array. In order to hold normalization, the function needs to be converted as such

$$\int_{-\infty}^{\infty} \left(\frac{\partial k_{sy}}{\partial d}\right) P(k_{sy}(d), L, w_p) \mathrm{d}d = 1. \tag{2.33}$$

In order to find $\frac{\partial k_{sy}}{\partial d}$ we will first relate k_{sy} to the angle from the z-axis

$$k_{sy}(\lambda_s, \alpha) = \frac{2\pi}{\lambda_s} \sin(\alpha). \tag{2.34}$$

Now since the down converted beam passes through a collimating lens, the angle of the light arriving into the lens is related to the distance by

$$\tan(\alpha) = \frac{d}{F_c}, \tag{2.35}$$

where F_c is the focal length of the collimating lens. Finally, the relation between k_{sy} and d can be given as

$$k_{sy}(\lambda_s, d) = \frac{2\pi}{\lambda_s} \sin\left(\arctan\left(\frac{d}{F_c}\right)\right), \tag{2.36}$$

and

$$\frac{\partial k_{sy}}{\partial d} = -\frac{2d^2\pi}{\left(1+\frac{d^2}{F_c^2}\right)^{3/2} F_c^3 \lambda_s} + \frac{2\pi}{\sqrt{1+\frac{d^2}{F_c^2}} F_c \lambda_s}. \tag{2.37}$$

In order to find the range of k vectors which will make it into the fiber, we also need the parameter δk

$$\delta k = \frac{2\pi}{\lambda_i} \cos(\alpha) \delta\alpha. \tag{2.38}$$

We now want to see the probability distribution over the pixels of the array. To do this, we integrate the probability density function in increments corresponding to the size of the pixels on the array. For the particular array used in this experiment, the active area was 20μm and the full pixel width was 100μm. Now we will look at the effects of changing the beam waist, the crystal length and the input pump angle on the probability of measuring the signal photon.

2.2.4 Effects of Changing the Beam Waist, Crystal Length and Input Pump Angle

To demonstrate the effects of changing the beam waist size and crystal length on the probability distributions of measuring the signal photon given a detection of the idler photon, I will show a similar picture as to that in Figure 2.4. Each bar in each plot represents one pixel and the height is the probability of measuring a photon on that pixel relative to the other pixels. As mentioned above, this is achieved by integrating Equation 2.31 over the array by pixel size.

From Figure 2.5 we can see the different effects changing these parameters has on the distribution on the array. To start with the crystal length, it appears to have a relatively negligible effect. There is a slight broadening of the distribution as the crystal gets shorter but the impact is not that great. This is good since shorter crystals give lower efficiency in SPDC. The pump waist size on the other hand has a very noticeable effect. By having a very broad pump beam, the photons focus more tightly on the center of the array. This is better since we want to resolve the spatial locations of these photons, so the tighter they gather on the array, the more discernible their spatial directions.

Now to observe the effects of the input angle of the pump beam on the array. To incorporate this into our function, we use the momentum conservation relation once again. Originally we assumed that k_p had no transverse components so we only had $k_s = k_i$ but

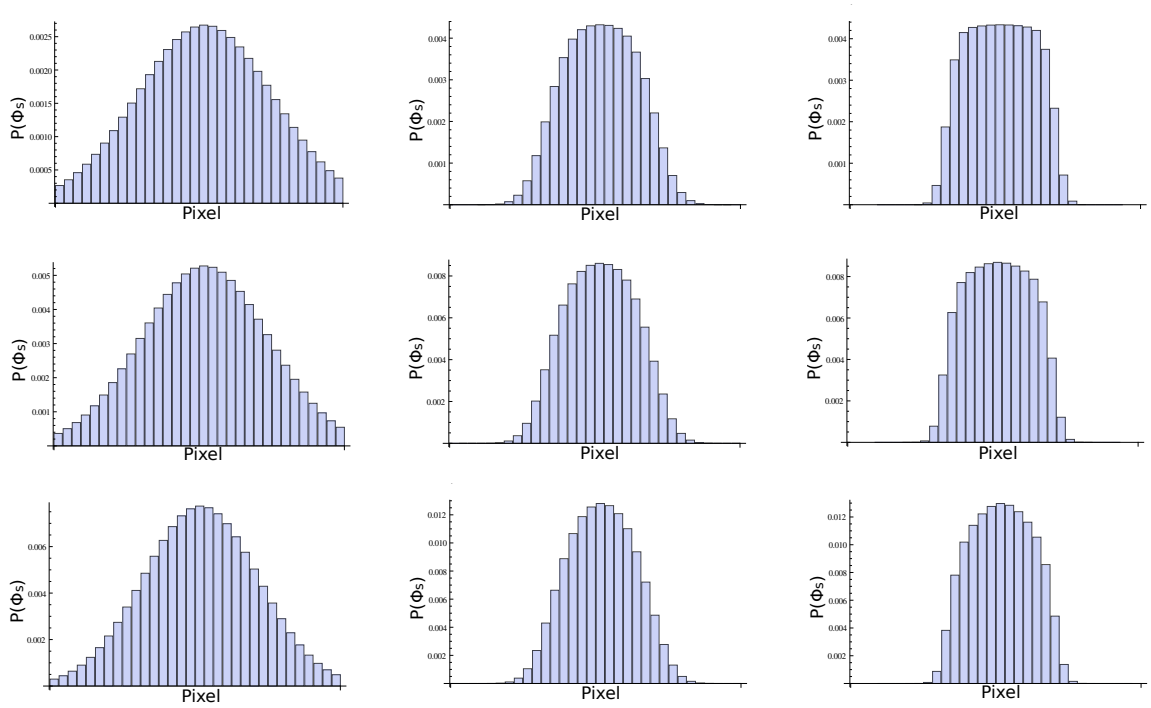

Figure 2.5: The diagram represents the probabilities of measuring the signal photon on each pixel on the array. The crystal length increases as you move down the chart (500μm, 1000μm, 1500μm) and the beam waist increases as you move towards the right (20μm, 70μm, 150μm).

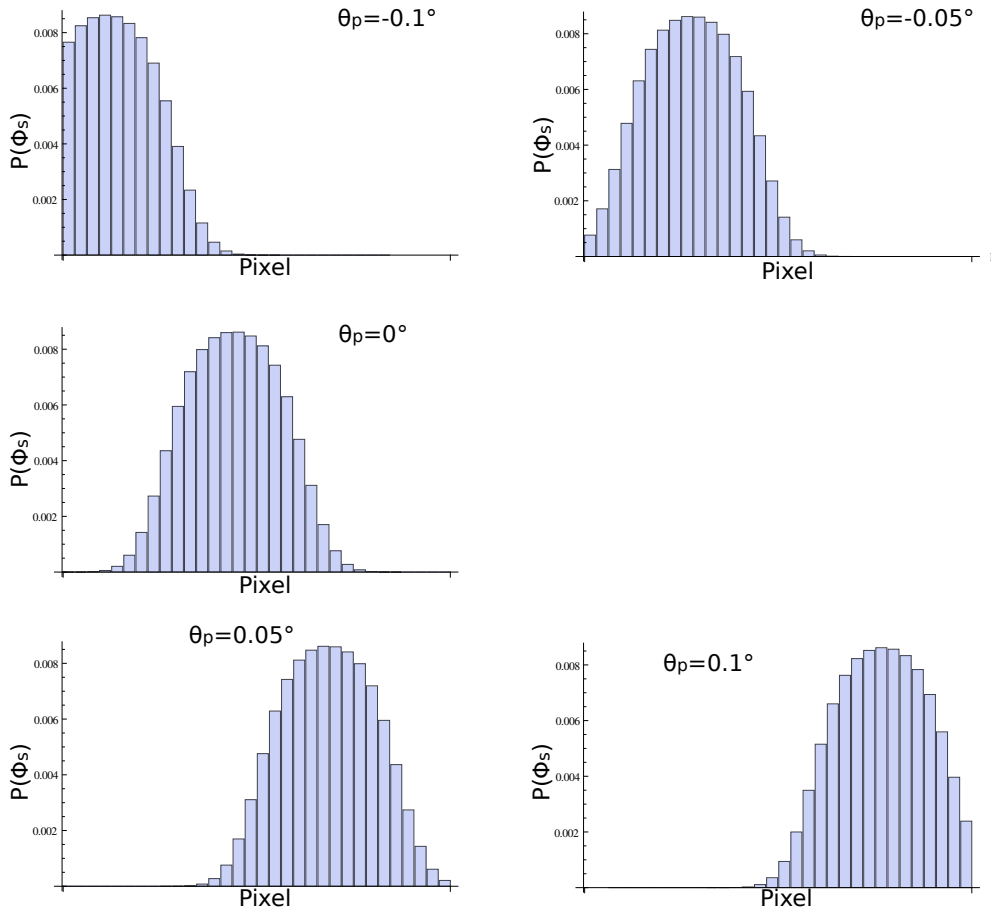

Figure 2.6: Theoretical signal photon distributions on the SPAD array for pump angles of $-0.1°$, $-0.05°$, $0°$, $0.05°$, and $0.1°$. The crystal length is 1000μm and the beam waist is 70μm.

in opposite directions. Now that we want to add a transverse component, we have

$$k_s - k_p = -k_i. \tag{2.39}$$

This means that instead of just having k_s as input into Equation 2.31 we use $k_s - k_p$ where we define k_p in the following way,

$$k_p(\lambda_p, \tau) = \frac{2\pi}{\lambda_p} \sin(\tau). \tag{2.40}$$

where τ is the pump input angle. Figure 2.6 shows the array at input pump angles from $-0.1°$ to $0.1°$. (The crystal length is 1000μm and the pump waist is 70μm in this case.)

From this analysis we can see that the center of the beam distribution seems to move 10 to 11 pixels over when the pump angle is changed by $0.1°$. It is noted that by changing the

input angle of the pump, there would be slight wavelength changes in the signal and idler beams, but to first order, we can neglect this effect. Now I will explain the experimental setup and we will compare the model and the experiment for varying the pump angle into the crystal.

2.3 Experimental Setup

The source of SPDC in this experiment is a type-II non-collinear degenerate source. The crystal is cut such that the down-converted photons each exit at 3°. The pump is a 404nm Toptica iWave laser and the daughter photons are both 808nm. A diagram of the setup can be seen in Figure 2.7 and the real setup can be seen in Figure 2.8. There are four main sections to this setup: the polarizing beam splitter and wave-plate section which allows the beam to go to the deformable mirror and back, The deformable mirror and Shack-Hartmann wavefront sensor section for wavefront modulation, after the crystal there is the signal arm which is detected by a Single Photon Avalanche Diode (SPAD) detector array, and finally the idler arm which is focused into a single mode 1550 fiber. We will begin by discussing each section individually.

2.3.1 Polarizing Beam Splitter

As mentioned above, the purpose of having the Glan-Taylor polarizing beam splitter and the wave-plate setup (Figure 2.9) is to allow the beam to propagate to the deformable mirror and back and then be separated off to go towards the crystal. The pump laser emits linearly polarized light (as discussed in Section 1.4.1). The initial half-wave-plate aligns the linearly polarized light in the horizontal state to allow for transmission through the polarizing beam splitter. The quarter-wave plate then transforms the linearly polarized light to circularly polarized light (rotating linear polarization). Initially it begins in either right or left circular polarization.

Each time circularly polarized light strikes a reflecting mirror surface, it flips from the right to the left, and vice-versa, polarization state. After the beam has reflected from the deformable mirror and back to the quarter-wave-plate it has reflected three times, which means it is in the opposite polarization state from which it started. After passing through the quarter-wave plate, it is now polarized in the vertical direction. This means that it will be reflected in the polarizing beam splitter and move in the direction towards the crystal.

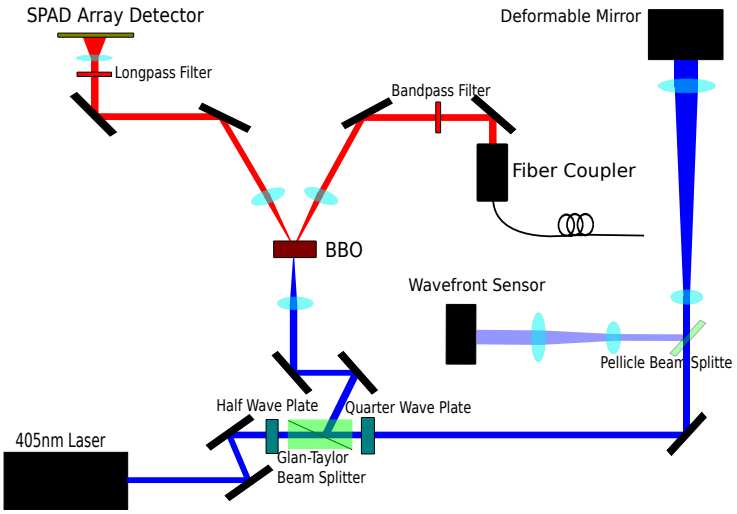

Figure 2.7: Diagram showing the setup for the spatial correlations in SPDC experiment

Parameter	Value
Aperture shape	Circular
Mirror coating	Aluminum
Aperture dimensions	15mm diameter
Number of electrodes	17
Control voltages	0...171V
Initial RMS deviation from plane	less than 0.1μm
Maximum deflection of the mirror center	9.4μm

Table 2.2: Parameters describing the OKOtech deformable mirror [51]

2.3.2 Deformable Mirror

The deformable mirror used in this setup is an OKOtech 17-channel micromachined deformable mirror with a built-in tip-tilt stage (Figure 2.10). A lot of deformable mirrors do not have enough motion in their actuators to compensate for tip-tilt errors so this mirror has one built in separate from the actuator structure. The parameters of our mirror are given in Table 2.2.

The electrostatic actuators for this specific mirror are arranged in concentric circles with one in the center, 4 in the next circle and 12 in the outside circle (See Figure 2.11). Having the actuators in a circular structure makes implementing the Zernike polynomials quite simple as they are defined in a circular manner.

Although due to time constraints we have not used the mirror to deform the wavefront

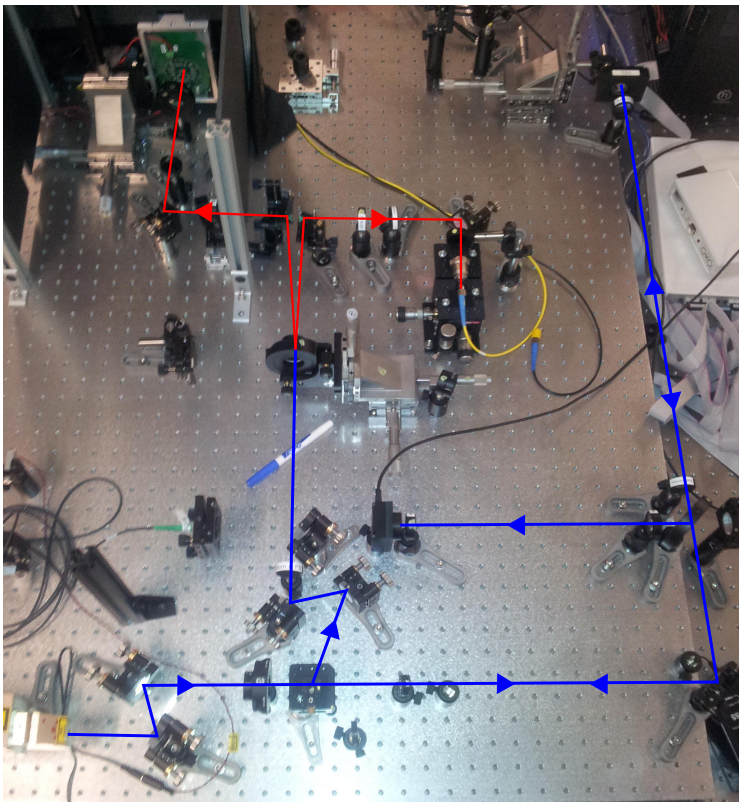

Figure 2.8: Actual setup for the spatial correlations in SPDC experiment. The blue lines represent the pump laser traveling from the laser, to the deformable mirror, back to the Glan-Taylor beam splitter and entering the crystal. The red lines represent the signal (right) and idler (left) photons exiting the crystal and propagating to their respective detectors.

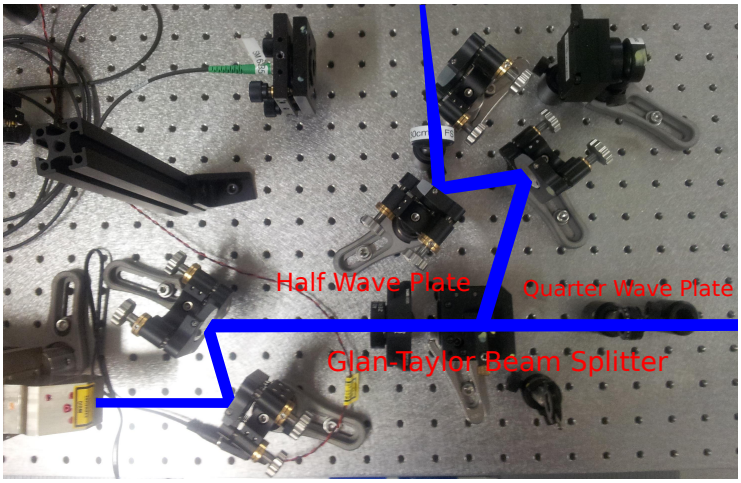

Figure 2.9: Beginning of the pump propagation path which contains a half-wave plate, a Glan-Taylor beam splitter and a quarter-wave plate. This setup allows us to manipulate the polarization of the light so we can send it to the deformable mirror, have it bounce back and then change directions in the beam splitter to move towards the crystal.

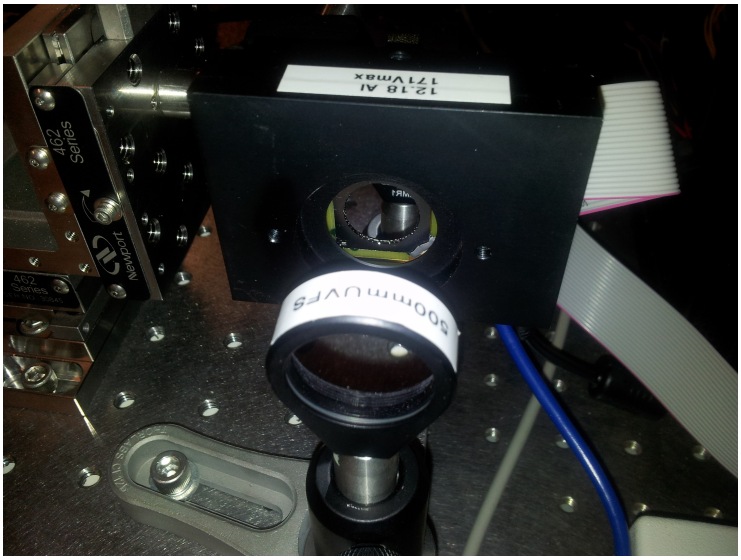

Figure 2.10: OKOtech 17-channel deformable mirror with built in tip-tilt stage.

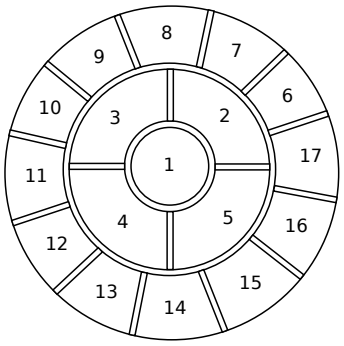

Figure 2.11: Electrostatic actuator layout in the deformable mirror.

for the SPDC experiment, we have had the mirror running and observed the effect of manipulating the various actuators. For the actual experiment, we had a mirror placed just after the quarter-wave plate which still maintained the polarization requirements (as detailed in Section 2.3.1) since there was still an odd number of mirror reflections.

In 2011, I traveled to Padua Italy where I worked on a setup very similar to the one in [67] (it was the actual setup, just in its beginning stages before the experiment was performed). While there I learned to use the Frontsurfer software which is used to control the deformable mirror. I also was able to see the mirror creating the various physical aberrations described in Chapter 1. The next stage of this experiment is to implement this deformable mirror into the setup and deform the wavefront and observe the effects on the spatial properties of the daughter photons of SPDC.

2.3.3 Fiber Collection of Idler Photon

The optics in the idler arm consist of two mirrors to direct the beam into towards the fiber, two lenses and an 810nm band-pass filter with a 10nm FWHM. The first lens is a 30cm focal length lens to collimate the idler beam after it exits the crystal. The second lens is an 11mm focal length aspheric lens to focus the light into the single mode fiber designed for light at 1550nm. We originally used a single mode fiber designed for light at 810nm but wanted to see if we could increase the counts. It turns out that the counts did not increase by a significant factor which demonstrated that the single mode fiber was coupled very well. To determine the spread of angles that will be collected from the down conversion crystal, we start at the fiber end and work backwards.

If we consider the core size of a single mode fiber at 810nm of 5.0μm and pass it through two lenses, one of 11mm focal length and one of 30cm focal length, the beam ends with a

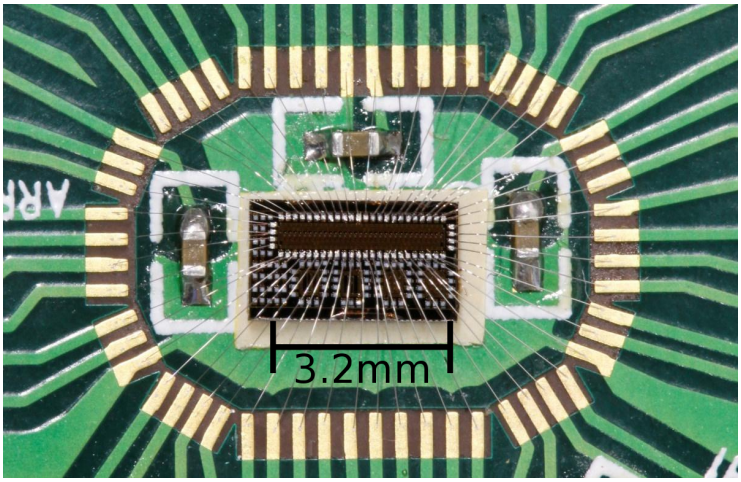

Figure 2.12: The 32-channel SPAD array used to detect the position of the signal photon.

waist of 140μm (keep in mind these are the diameters). Using the following formula [57]

$$\theta = \frac{\lambda}{\pi w_0}, \tag{2.41}$$

where w_0 is the beam waist, we find the divergence angle of the beam to be 0.004rad (note we multiplied by two to get the full divergence angle). This will be useful in the theory calculations. Once this side was aligned and coupled, we averaged 34000 counts per second on the idler side.

2.3.4 SPAD Array

Our method of observing the spatial correlations of the daughter photons created through SPDC is made possible by an array of single photon detectors as seen in Figure 2.12. This array contains 32 single photon avalanche diode detectors arranged in a line array of 32 pixels. Each pixel is 100μm $\times$ 100μm but has an active area of about 20μm $\times$ 20μm in the center of each pixel. This detector has a custom designed power supply which can be seen in the little black box in Figure 2.13. Table 2.3 lists the dark counts of each of the pixels.

The time taggers used in this experiment each have 16 channels for input signals. Because one channel on each time tagger is used for the idler photon detection, 30 channels remain for the SPAD array. Channels 9 and 30 had the highest dark count rates so these channels were not used. This means there are two gaps in the detection array in these positions.

The optics leading the signal beam towards the SPAD array are quite simple. There is a 30cm focal length spherical lens that collimates the beam. There are also two mirrors,

Pixel Number	Dark Counts per second
1	12000
2	1800
3	23000
4	1800
5	8800
6	2050
7	1700
8	2200
9	540000
10	2050
11	1950
12	33000
13	2070
14	2200
15	5600
16	2300
17	25500
18	5300
19	4200
20	2300
21	2100
22	2090
23	2050
24	96000
25	3600
26	2300
27	1800
28	1940
29	2030
30	97500
31	2600
32	1800

Table 2.3: Dark counts for each of the pixels in the SPAD array.

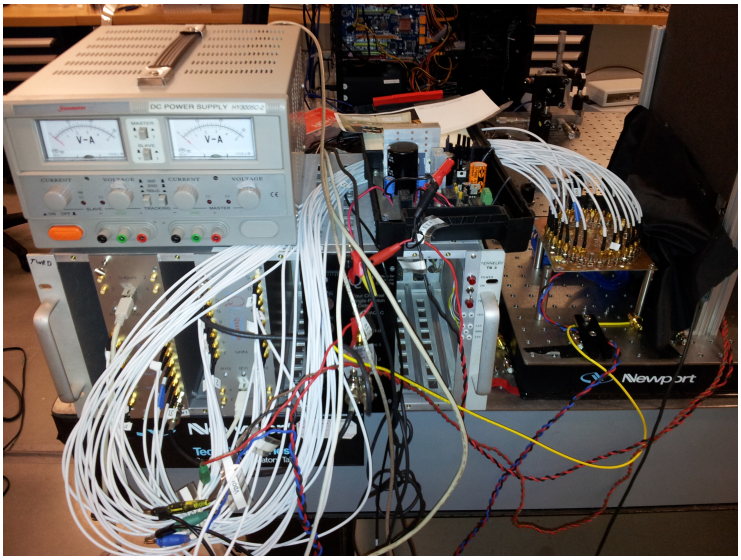

Figure 2.13: The majority of electronics in this picture are for the SPAD array. Each white cable is one channel from the array connecting to a time tag unit. There is also a 4 channel fiber coupled single photon detector which to which the idler side fiber connects.

one small prism mirror placed to pick off the beam departing at 3° and one round mirror to direct the beam towards the SPAD. There is a high-pass filter with a cutoff at 700nm to help remove background light placed in front of the SPAD as well. In order to increase counts received at the array and because it only spans in one direction, a 5cm focal length cylindrical lens is used to squeeze the beam in the y direction to project onto the array. This lens required precise orientation to make sure the photons were projecting parallel to the array and not at an angle.

The alignment of the array was accomplished by monitoring the coincidence counts as the array was mechanically scanned in the vertical direction at about 2μm per second. When a peak was found, the rotational orientation of the cylindrical lens was shifted slightly to determine the largest spread across the array. Again to make sure that the rotation of the cylindrical lens was aligned, the array was shifted horizontally and the coincidence counts were monitored to ensure the amount didn't drop, just the horizontal position on the array. When the rotational alignment was finished, the array would be scanned vertically one more time to ensure the position of maximum coincidence counts.

The LabVIEW program is designed to monitor the coincidence count rates between each channel on the array and the photon detected in the idler fiber. Since each arm of the down converted beams had a slightly different length, and the electronics were different on each side, there was a delay between the photon arrivals on each side. This meant that

the delay between each pixel and the idler fiber had to be determined and entered into the program. A LabVIEW program made by Dr. Piotr Kolenderski was able to find these delays for each case. I looked at the coincidences between each channel with this program and found the delays which are listed in Table 2.4. With the current setup, the signal photon detector always fires first. This means, for instance in channel 1, that the signal photon arrives 32.5ns before the idler photon. The error in the time of arrival, or jitter, for this experiment was 2ns so the coincidence window was set to 2ns. This means if a photon is detected on the idler side within 2ns of a detection on the signal side, it will be recorded as a coincidence count. Once all these components were aligned and set, we were able to start manipulating the pump beam to observe the spatial correlations of the photons.

2.3.5 Changing the Input Pump Angle

Because the deformable mirror has not been fully introduced into the setup yet, we needed a way to change the pump beam angle into the crystal. To accomplish this, we put a piece 1cm thick piece of BK7 glass in the beam path between the beam splitter and the first mirror towards the crystal. To first order, parallel beams entering a lens in different locations pass through the focal point at an angle. The beam was originally aligned in the focusing lens such that the beam passed through the center. This means that if we are able to shift the beam, it will then be focused down on the crystal at a slight angle. By putting the piece of glass in the beam path before the crystal, and turning it slightly, we were able to shift the beam.

To measure the angle at which it went through the crystal, a 50cm focal length lens was placed 50cm behind the crystal and a CCD camera imaged the beam after it passed through this crystal. With this setup as seen in Figure 2.14 we could measure the horizontal displacement of the beam and thus infer the angle at which the beam passed through the crystal. The angle could be determined as

$$\theta = \arctan\left(\frac{d}{0.5}\right). \tag{2.42}$$

With the piece of glass, we were able to get deviations on the CCD of 1mm in either direction which works out to a deviation angle of $\pm 0.1^\circ$. Each trial consisted of moving the beam spot on the CCD camera by 100μm and measuring the coincidences for 5 second increments over a period of 2 minutes. After all the runs were complete, a background measurement was done where the laser remained on, but the beam to the signal (array) arm was blocked so only background light was measured on the array. To get the distribution

Pixel	Delay (ns)[±1ns]
1	32.5
2	31.5
3	32
4	32
5	31.5
6	31.5
7	32.5
8	29
10	30
11	29
12	29.5
13	31
14	30
15	31
16	32.5
17	31.5
18	31.5
19	31.5
20	32.5
21	31.5
22	31.5
23	32.5
24	32.5
25	29.5
26	29
27	29.5
28	30.5
29	31
31	31
32	30

Table 2.4: The delays between the time tag of the signal and idler photons for each channel. These delays take into account path differences as well as electronic signal delays.

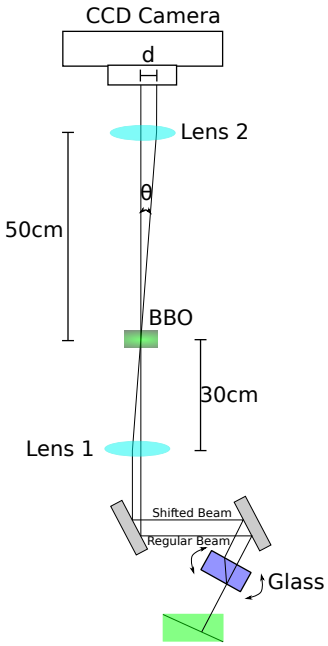

Figure 2.14: Measurement scheme to determine the pump angle from rotating a piece of glass in the optical path.

of photons on the array, the average of a run was calculated and the background was subtracted from the result. The results for 0°, ±0.046°, and ±0.10° can be seen in Figure 2.15.

In order to extract the peak from these plots, I fit a Gaussian function ($ae^{-\frac{(x-b)^2}{2c^2}}$) with Mathematica to the data and then extracted the b value which is the center of the Gaussian. Because the fit will give a decimal answer, it will be rounded to correspond with the nearest pixel. These centers of the experimentally determined centers and the theoretically determined centers are shown in Figure 2.16.

From the data in Table 2.5, it is noticed that the peaks do not align perfectly and also seem to work better in the negative direction. Upon analyzing Figure 2.16 this trend can be seen for the expanded data set as well. The experimental setup is currently under investigation to determine a possible source for this discrepancy. Possible sources of error could be related to the collimating optics after the down conversion. If these lenses are not very finely aligned, this can cause a problem in calculating the mapping between the detectors and the collimating lenses which might skew the experimental results. If they are not centered very well, this could also account for the difference between positive and negative pump input angles. These issues will be addressed in the next iteration of this

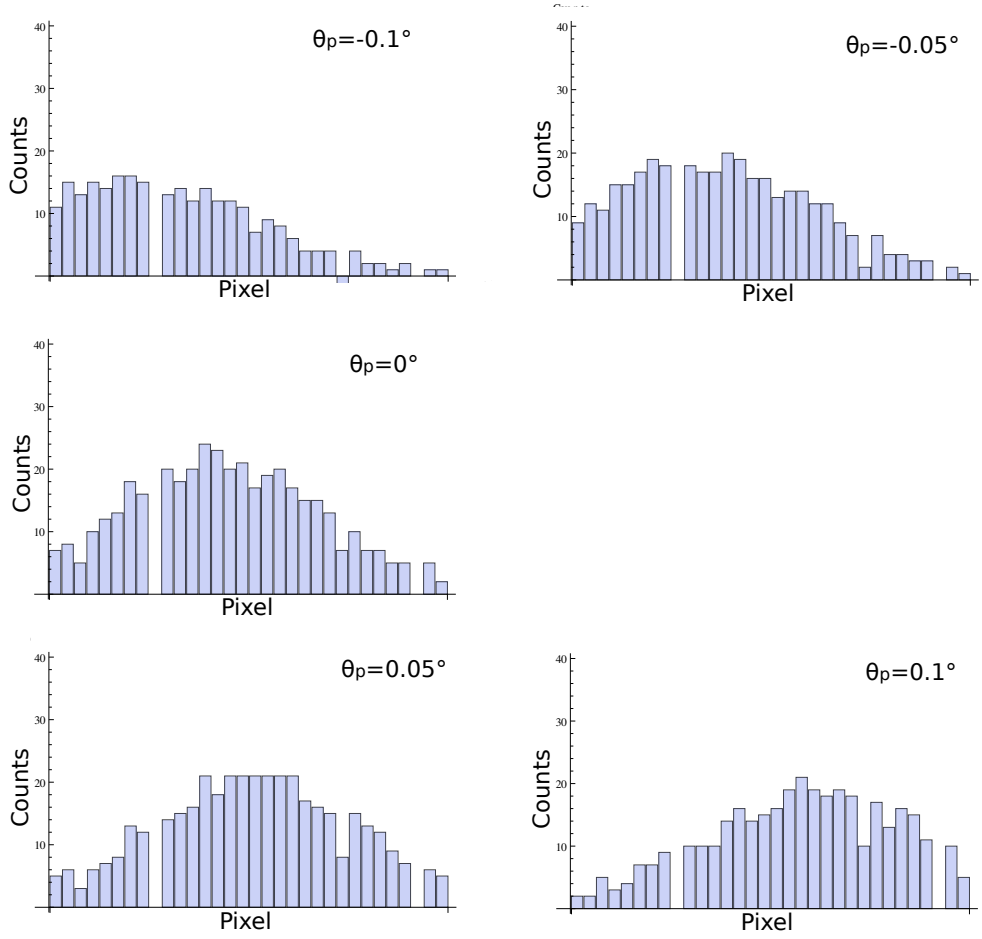

Figure 2.15: Experimental signal photon distributions on the SPAD array for pump angles of $-0.1°$, $-0.05°$, $0°$, $0.05°$, and $0.1°$. The crystal length is 1000μm and the beam waist is 70μm.

Input Pump Angle	Central Pixel (Theory)	Central Pixel (Experiment)
$-0.1°$	4	6
$-0.05°$	9	11
$0°$	15	15
$0.05°$	20	17
$0.1°$	25	20

Table 2.5: Center of signal photon distribution on the SPAD array for different pump input angles as determined by a Gaussian fit (rounded to the nearest pixel for a subset of the data).

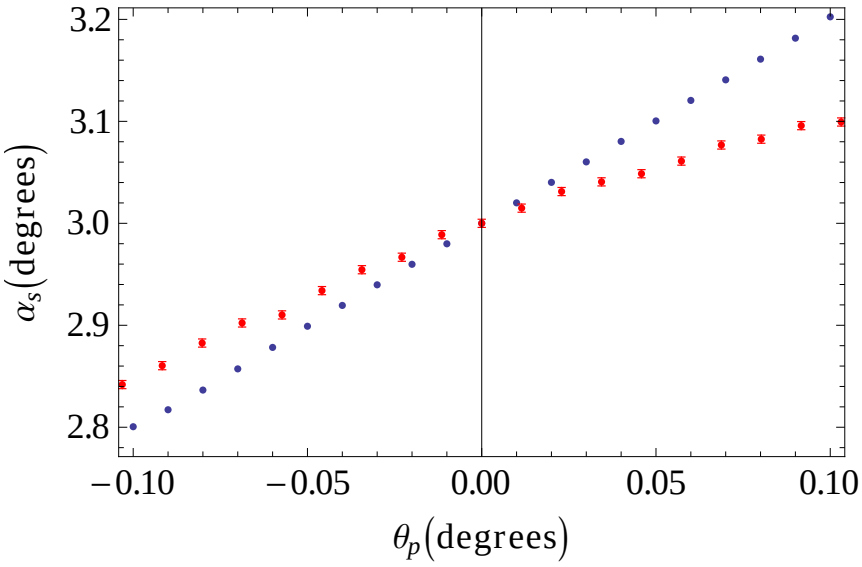

Figure 2.16: Theoretical results for signal angle versus pump input angle are given by the blue data points and experimental results are given by the red data points. Subset of data is given in Table 2.5.

experiment.

2.4 Discussion

The experiment presented above has great opportunity for growth and future results. Although the theory derived at the beginning of this Chapter and the data from the experiment do not match exactly, there are possible experimental reasons as to why this may be so. By examining the collimating lenses and retaking the data, we will have a better idea as to whether the theory and experiment are compatible.

The next phase of this experiment will be to incorporate the deformable mirror into the beam path and use it to alter the wavefront of the pump beam. We will then be able to determine the relationship between the wavefront of the pump beam and the spatial correlations of the down converted photons. For the theory side, it assumes a Gaussian beam for the calculations. I would like to incorporate the ability to use various wavefronts as can be created by the deformable mirror to see the theoretical relations in our model. Some work has been done on this type of theory and experiment by Monken *et al.* [69] and I believe the model we have shown above can be expanded to include these ideas.

The ultimate goal of this study into the spatial correlations of photons in SPDC is to see whether we can create a post-processing pointing scheme. If the coincidences on the array detector could be monitored locally and the photons of the other side sent a far distance, we can observe the shifting of the coincidence on the array as the long distance arm is affected by turbulence or other issues. Then using the correlations between the pump beam and the down converted beams, we could steer the photon in the far arm such that the coincidences move back to the center of the array.

To begin testing this scheme, I will first finish the experiment as it is setup now, but then will move the fiber coupled receiver a far distance away from the local setup (on the order of meters). Once this design is running, we can also introduce simulated turbulence through a mechanism such as given in Chapter 3. With this setup we could also test adaptive optics corrections to the beam propagating across the lab. So not only consider angle changes to the beams direction, but also wavefront influences to attempt to increase the signal.

Chapter 3

Laser Scintillation and Atmospheric Turbulence Testing on a Quad Photodiode Sensor

This chapter details an experiment done under contract of COMDEV Canada in 2013 and was submitted to the Canadian Space Agency in an altered form [74] with the following authors:

Chris Pugh, Brendon Higgins, Jean-Philippe Bourgoin and Thomas Jennewein.

I have obtained permission to reproduce this document in an altered form with additional details and new results as work for this Masters Thesis.

Author Contributions

Thomas Jennewein applied for the study of scintillation effects on the detector which COMDEV is studying for acquisition, pointing and tracking of a QKD satellite. Brendon Higgins helped design the LabVIEW program which records the data from the CMOS camera and the QUAD detector. Jean-Philippe Bourgoin assisted with creating figures for the report and with ensuring the laser for the experiment worked properly. I built the optical setup from a layout designed by Thomas Jennewein, performed the experiment and analyzed the data along with Thomas Jennewein.

3.1 Introduction

Any laser beam that passes through the Earth's atmosphere experiences scintillation due to atmospheric turbulence [4]. If one tries to use a beacon laser for acquisition, pointing and tracking of a satellite, an appropriate detector must be chosen which will not be negatively

affected by these scintillation effects. The scintillation will cause the received power at the detector to fluctuate and could cause errors in the received position reading, depending on how the detector is designed and operates. The purpose of the experiment presented here is to investigate the effects of scintillation on the selected detector and as we will see show that the detector does not respond negatively to simulated turbulence and intensity modulations and even under these conditions will still yield an accurate position reading.

3.1.1 Quad Detector

The device under test in this experiment is the QP50-6SD2 [75] quad photodiode array from Pacific Silicon Sensor Incorporated. This device has been chosen as a potential candidate for the fine pointing system in the satellite and thus needs to be tested under scintillation effects to demonstrate that it can still maintain accuracy.

The sensor is arranged in a circle with four photodiodes, one in each of the top-left, bottom-left, top-right, and bottom-right corners. There are also small gaps between each of the photodiodes forming a cross on the sensor. The device uses current-to-voltage amplifiers from each of the photodiodes and has three outputs. It can output the bottom minus top voltage, the left minus right voltage, and the sum voltage of all four quadrants. The voltage reading for the difference signals relates to the light intensity on each of the four quadrants. The gap between each of the photodiodes is 42μm. The maximum voltage output depends on the power supply voltage. For our power supply unit, this voltage is 12V which gave us a maximum output voltage of approximately 10.4V. The sign of the voltage output would depend on exactly where the beam was most intense.

COMDEV has customized the particular quad detector that was tested to suit our application. The quad detector will be attached to a movable system that will allow it to center the incoming beacon laser onto the sensor. The quantum signal will be in the center of the beacon and will need to reach the detectors in the back of the apparatus. For this purpose, a hole has been drilled into the center of the quad photodiode which will allow the quantum signal to pass through once the beacon is centered. The hole on the particular quad under test is about 600μm in diameter.

The quad sensor also has some great benefits that make it a good choice for this application. First of all, it has a high linear response to input intensity and a large dynamic range which makes it very versatile to various beam strengths. Secondly, due to it only having four analog outputs, it is very fast in calculating position and can create very fast feedback. This allows one to remove the slow processing layer of calculating the position.

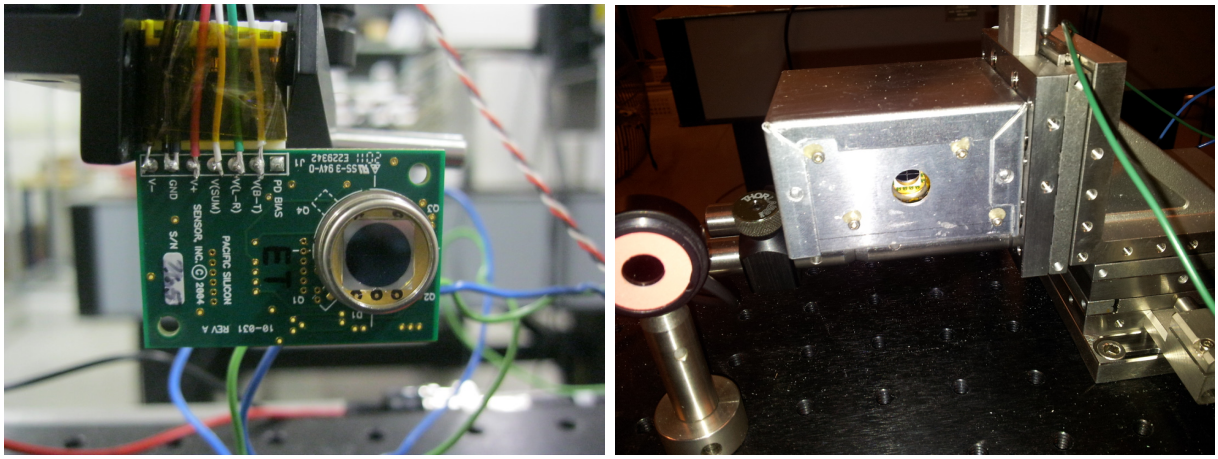

Figure 3.1: The quad detector on the right does not have a hole cut in the center but shows the photodiode section along with the circuit electronics for current to voltage amplification as well as the output cabling. On the right is the actual quad detector that was tested. It is enclosed in a metal box which also contains the photodiode detector for the quantum signal for testing purposes (no polarization detection). At the center is the hole where the quantum signal will pass through once the beacon laser is centered on the quad photodiode.

It also seems to be a good choice for this application as these types of devices are used quite often for tracking purposes in similar scenarios [6].

3.2 Experimental Setup

To test the effects of scintillation on the performance of the quad sensor, the following parameters were varied:

- Spot size – 1mm to 3mm
- Spot intensity – 260μW to 2.75mW
- Spot shape – Circular and elliptical

To change the spot size and the spot shape, lenses and an iris are used. For initial testing we used a beam size of 1mm diameter but then did further testing on a spot size of 3mm as in a prior study it was shown that the beam size will be roughly three times that of the hole size in the center of the quad detector. The lens which can be seen at the beginning of the setup in Figure 3.2 is used to collimate the very divergent beam exiting

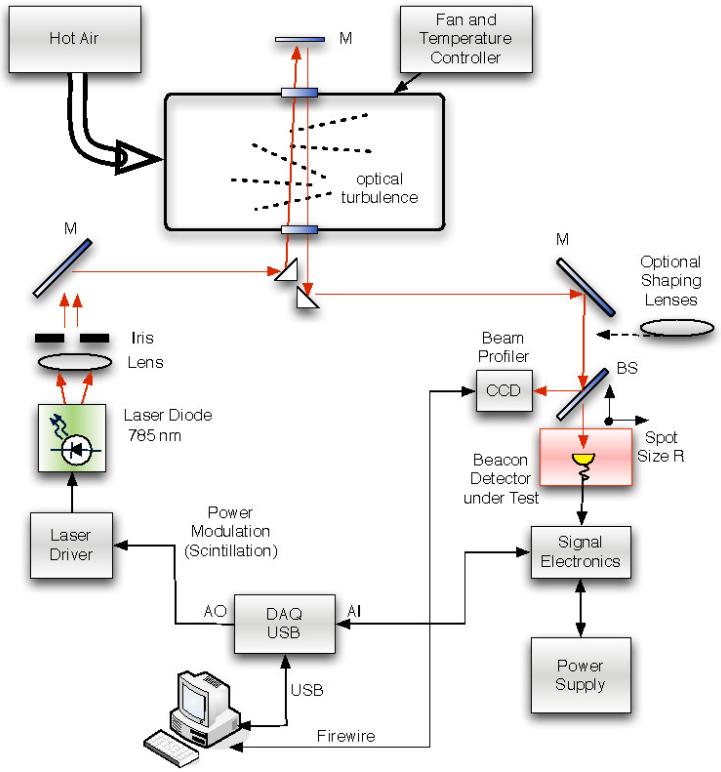

Figure 3.2: Experimental setup showing the turbulence chamber for positional shifting as well as the electronics to create the intensity modulation and record the data from the CMOS camera and the quad sensor. The optional shaping lenses included cylindrical lenses to change the beam shape from circular to elliptical.

the laser diode casing. Once this beam is collimated, an iris is used to set the spot size. This allowed the beam to be reduced to 2.5mm diameter. In order to achieve smaller beam sizes, spherical lenses were used which focused the beam onto the quad sensor. When an elliptical beam was required for testing, a cylindrical lens was used to condense the beam in one axis.

The setup incorporates two methods of creating synthetic atmospheric disturbances on the laser beam before the spot hits the detector. For positional disturbances (shifts the position of the beam on the detector) we use the turbulence box described in Section 3.3. To modulate the intensity, we use the Thorlabs laser diode as shown in Table 3.1 along with a laser controller. This unit takes an input voltage signal which modifies the intensity of the laser. One nominal wavelength, 785nm, was used for this experiment, although, the laser did slightly shift frequencies as it modulated in intensity.

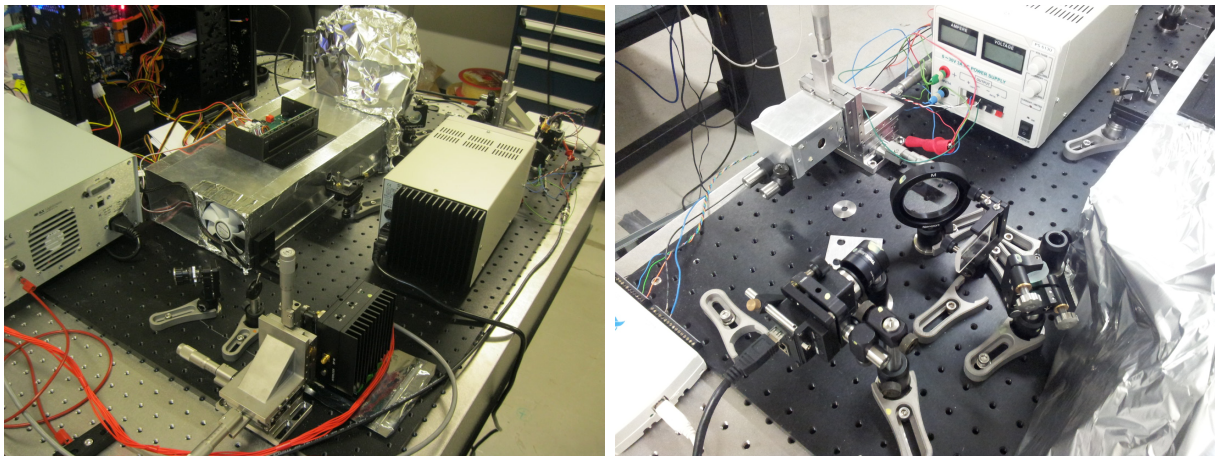

Figure 3.3: Left, the laser can be seen in the bottom, its beam then passing through the iris. The beam is then deflected with the mirror, to the prism mirror, where it enters the turbulence box. It is then reflected back from the other side, hitting the other prism to continue towards the detectors. Right, the beam enters from the right and passes through the beam splitter (the cylindrical lens is also seen here, creating the elliptical beam). The CMOS camera (bottom-left of image) and quad detector (top-left of image) are equal distances from the pellicle beam splitter. The filters can also be seen in front of the CMOS camera.

Equipment	Type	Model Number
Laser	Thorlabs Mounted 5.6mm Laser Diode	L785P090
Laser Mount	Temperature Controlled, Laser Diode Mount	TCLDM9
Laser Controller	ILX Lightwave Laser Diode Controller	LDC-3724C
Turbulence Generator	Custom Built	
Fan Controller	Kaze Master Flat	KM06-BK
Lenses	Various lenses from Thorlabs	
CMOS Camera	Basler Fast Frame Camera	A622f
QUAD Sensor	Pacific Silicon QUAD Sum and Difference Amplifier	QP50-6SD2
USB DAQ	National Instruments USB DAQ	NI USB-6211
Control Software	National Instruments LabVIEW	Version 2012

Table 3.1: Components for the laser scintillation test setup.

In order to see the effects of the distortions we apply to the laser on the quad sensor, we use a pellicle beam splitter (92% transmission to 8% reflection) to pick-off a small portion of the beam and send this portion to a CMOS camera. The data from the quad and CMOS sensors is saved and later analyzed to inspect the correlations.

The 8% pick-off was still very bright on the CMOS camera, so neutral density filters were used to reduce the beam intensity to a level where it was still detectable at the minimum laser intensity that was induced. This ensured the CMOS camera was always able to determine the position of the beam, therefore allowing the correlations to always be monitored. The beam intensities (above) were chosen for two reasons. First, the expected received signal at the satellite will be at or well below these levels, and second, this prevented the quad sensor from being saturated whilst the minimum intensity of the laser fluctuations was still detectable.

Having the CMOS camera as a reference sensor allows us to have a very detailed analysis of the beam shape due to the large number of pixels which the beam falls on. This allows us to determine the shape of the beam interacting with the quad sensor to ensure it performs well even when the beam is not optimal. Also, the CMOS allows us to record video which we can then analyze along with the recorded data.

3.2.1 Data Acquisition

Because the quad detector output voltage signals, an analog device was required to read in the signals such that a computer could monitor and record the output. For this purpose, a National Instruments USB data acquisition unit (USB DAQ) was used. This allowed for all three of the outputs from the quad detector to be monitored simultaneously, as well as output the generated noise signal to the laser amplifier for laser intensity modulation. When outputting the voltage signal for the intensity modulation signal, we hit the maximum output current from the USB DAQ and therefore to allow us to get the full range of intensity modulation we had a custom amplifier made.

To collect all of the data, as well as to control the equipment, a program was developed in National Instruments' LabVIEW. This program displays the input signals from the quad sensor via the USB DAQ, the normalized position on the quad sensor in the x and y directions, the normalized position of the spot on the CMOS camera, the actual video of the spot from the CMOS and the current frame rate of the CMOS.

To get the normalized position on the quad we read in the outputs as V_{lr} (left minus right voltage), V_{bt} (bottom minus top voltage) and V_{sum} (total voltage) and then calculate:

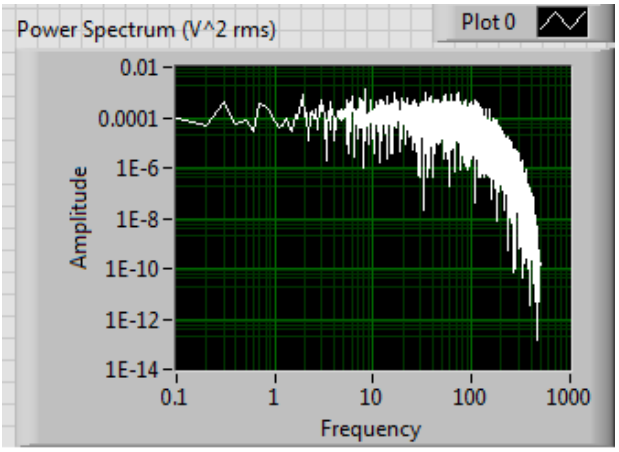

Figure 3.4: The generated noise spectrum from a white noise generator passed through a low-pass filter with a 100Hz cutoff. From this spectrum, the maximum amplitude would produce a minimum intensity output of the laser of 260μW, whereas the minimum applied amplitude (effectively 0) would correspond to a laser intensity of the maximum at 2.75mW.

$$X_{\text{norm}} = \frac{V_{\text{lr}}}{V_{\text{sum}} - V_{\text{back}}}, \quad Y_{\text{norm}} = \frac{V_{\text{bt}}}{V_{\text{sum}} - V_{\text{back}}}, \tag{3.1}$$

where V_{back} is the pre-measured total background level voltage of about 0.0005V.

The normalized position on the CMOS camera is determined from an algorithm very similar to the one described above, where the total area of the camera (number of pixels chosen to optimize beam size and frame rate) is split into four sections. Left minus right and bottom minus top section pixel intensities are read out. The normalization also divides by the total sum intensity on the CMOS.

The program also created a noise spectrum to apply to the laser unit to modulate the intensity. This profile was modeled after that measured in [4]. In LabVIEW, a white noise spectrum was generated and then passed through a 100Hz low-pass filter. The generated spectrum is shown in Figure 3.4.

3.3 Turbulence Generator

Testing transmission through long distance free space links to observe the effects on the propagating photons can be a difficult task to accomplish. One must find a proper location where they can have a large distance between the sender and the receiver, make sure they can get the equipment safely to each of the locations, be able to interact with each

location. This process can take a long time and can possibly be quite expensive. In 2006 Keskin, Jolissaint and Bradley [76] proposed a device to simulate atmospheric turbulence in a small device. This device is a small box using fans and temperature gradients to create turbulence. They provide a method for characterization to find the main variables associated with atmospheric turbulence as discussed in Chapter 1. Using the guidelines outlined in [76] I made a version of this turbulence box for use in this experiment. I present here the design specifications as well as the characterization data from my box.

3.3.1 Design and Construction

The walls and dividers in the box are made from aluminum sheets and are held together with aluminum tape. Figure 3.6 shows the dimensions of the box. It consists of five chambers, one in each corner and one in the middle where the beam propagates through. Two corner chambers are hot and cold air intake sections, and the other two corner chambers are air exit ducts. In order to determine the temperature in the chamber, four temperature sensors were placed along a line between the hot and cold air intake chambers. Small holes are drilled on the front and back in the center of the box to allow the laser beam to enter and exit the central mixing chamber.

To monitor the fan speed and the temperatures, a computer fan speed controller was used. This allowed up to four fans to be connected (only two were used) and up to four temperature sensors. Temperature measurements using this controller were limited to 100°C, so for sensing temperatures above that value, two Fluke Digital Multimeters were used. The cold air intake simply took room temperature air. For the hot air intake, a space heater was placed near the input fan and an aluminum foil tube directed the heat to the input. By surrounding the heater in aluminum foil, it allowed the hot air input to achieve a temperature of 125°C. Figure 3.5 shows the finished box with the laser entrance and exit holes drilled, and Figure 3.6 shows the schematics of the box.

3.3.2 Characterization

To characterize the turbulence generator, Keskin *et al.* [76] explain three different experiments to determine the parameters. For my generator, I performed the first two experiments since we had equipment readily available to accomplish this. The optical setup, which is the same for both experiments, can be seen in Figure 3.7. The diode laser is focused into a 635nm single mode fiber and then exits the fiber in the setup towards the turbulence box. The laser light is collimated after exiting the fiber with a 10cm focal

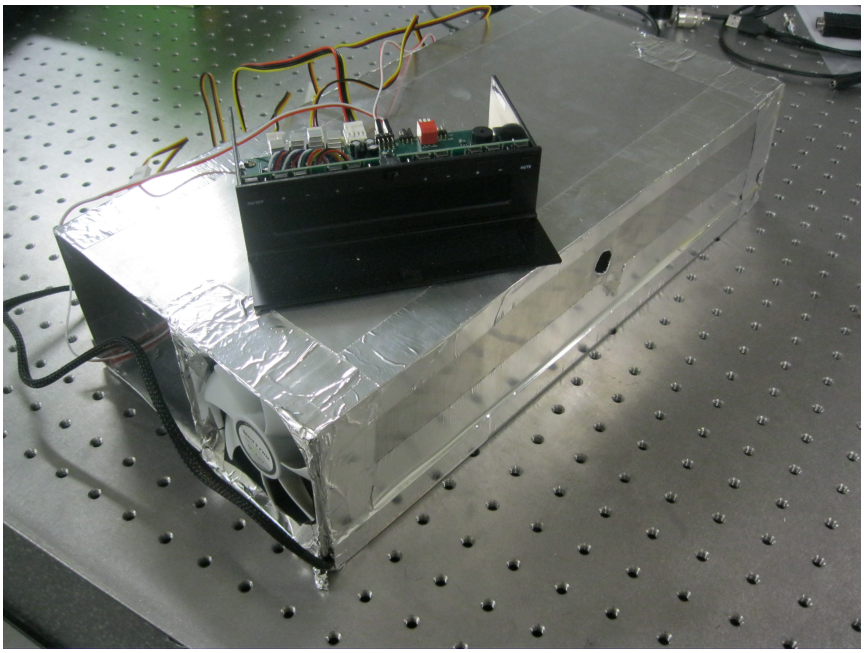

Figure 3.5: The completed turbulence box showing the fan controller and temperature monitoring unit and the box from a side-front view.

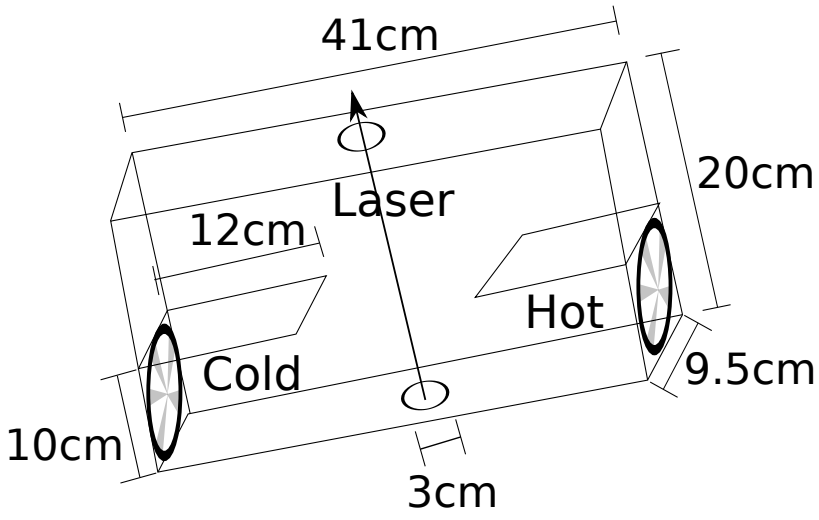

Figure 3.6: Schematic drawing of the turbulence box as viewed from the top.

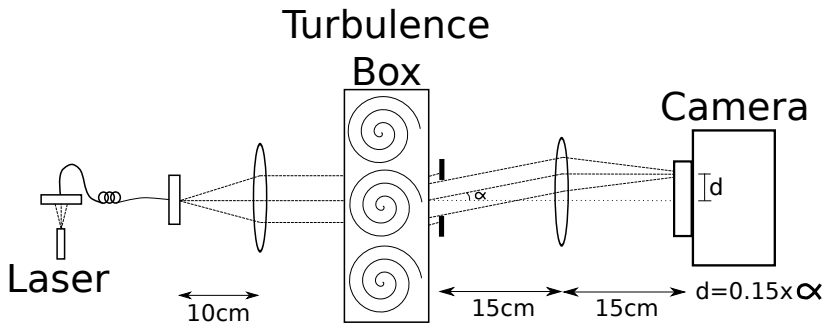

Figure 3.7: Optical setup for both the full-width at half-maximum and angle of arrival characterization experiments. In both cases the light was collimated with a 2" diameter, 10cm focal length lens and converged on the CMOS or CCD camera with a 2" diameter, 15cm focal length lens.

length lens. The beam is approximately 2.5cm in diameter when collimated. It then passes through the turbulence box and goes through an iris, which is used to simulate the aperture of a telescope. For these experiments, the iris ranges in size from 2cm diameter to 2mm. The light then passes through a 15cm focal length lens and is focused onto the CCD (for the full-width half-maximum experiment)/CMOS (for the angle of arrival experiment) camera. Absorptive neutral density filters are also used to ensure the camera is not saturated.

The laser source is a simple 635nm laser diode. The spectrum of this laser was measured with a Bristol Instruments spectrometer. Unfortunately the spectrometer requires an input range for the light to be measured which is split at 635nm. Because of this, I measured the diode in both regions above and below 635nm and averaged the results. Figure 3.8 shows the spectrum from the combined data. The resulting wavelength is 633nm.

3.3.3 Full Width at Half-Maximum Experiment

When observing light from a "distant" source, a common measurement is that of the point-spread function (PSF). This function shows how light from a point source spreads out as it travels from the object to the receiver. The useful measurement from this function, which is used to determine the resolution, especially for telescopes, is the full width at half-maximum (FWHM). This is the diameter of the PSF at half of the peak value. This measurement is performed over long exposure images to determine the effect of the atmosphere on the image.

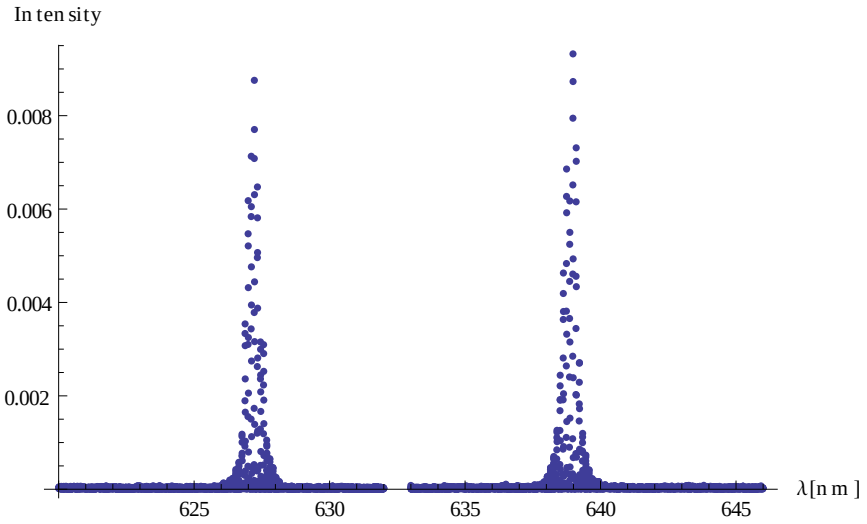

Figure 3.8: Laser diode spectrum from the Bristol Instruments spectrometer. The two spectra from each of the ranges above and below 635nm are pasted together and the average wavelength is used for the calculations.

The best resolution possible is limited by the diffraction of light as determined from the diameter of the transmitting telescope. Under circumstances of no turbulence, the FWHM of the PSF is simply λ/D with λ being the wavelength of light. When atmospheric turbulence is involved, the FWHM increases further depending on the Fried parameter of the turbulence. This effect is given by

$$\text{FWHM}_{\text{atmosphere}} \approx \frac{\lambda}{\text{r}_0}. \tag{3.2}$$

In the Kolmogorov regime, this now gives the measured FWHM to be

$$\text{FWHM} \approx \sqrt{(\text{FWHM}_{\text{telescope}})^2 + (\text{FWHM}_{\text{atmosphere}})^2} \tag{3.3}$$

$$\approx \frac{\lambda}{D}\sqrt{1 + \left(\frac{D}{r_0}\right)^2}. \tag{3.4}$$

When we have the outer scale $\text{L}_0 < \infty$, then FWHM $< 0.98\lambda/\text{D}$ so this measurement gives the upper bound on r_0.

For this experiment, 10s exposure images were taken on a Basler Scout scA640-120fm camera with no turbulence (box turned off and no heat gradient) and the fans set to $\approx$ 1500rpm and another set of images was taken with $\Delta T = 60°\text{C}$ and the same fan speed. The data was then analyzed in Mathematica (see Appendix A) where the FWHM

Quantity	Value[mm]
$r_0(\Delta T = 0)$	8.1 ± 0.4
$r_0(\Delta T = 60)$	1.6 ± 0.1
r_0	6.5 ± 0.5

Table 3.2: Calculated values for r_0 with two temperature differences, and the final r_0 calculated value for the box under these conditions.

and r_0 values were extracted. Figure 3.9 shows one example of the PSF before and after turbulence. Table 3.2 shows the averaged data from this experiment.

To find the r_0 of the system from the recorded data, we find the differences in r_0 values from the two samples. From this data, the calculated r_0 of the turbulence box for these parameters is 6.5mm $\pm$ 0.5mm. The drawback of this experiment is that it does not take the effect of the inner or outer scale into account (it assumes in the $L_0 \to \infty$ and $l_0 \to 0$ regime). Due to this, the real value of r_0 will definitely be smaller than the quoted value.

3.3.4 Angle-of-Arrival Experiment

The angle of arrival (AoA) is, in this experiment, the mean slope of the wavefront exiting the turbulence box, as shown in [76]

$$\alpha_p = \frac{d_x}{F_L} = \frac{\int\int P(x,y)\frac{\partial W}{\partial x}(x,y)\mathrm{dxdy}}{\int\int P(x,y)\mathrm{dxdy}}, \tag{3.5}$$

where $W(x,y)$ is the wavefront, $P(x,y)$ is the pupil function, d_x is the x coordinate of the centroid and F_L is the focal length of the imaging lens. The equation is similar for the y coordinate replacing x with y as appropriate.

To obtain useful information from this measurement, we require the variance of the AoA in the x and y directions. Keskin *et al.* modify Equation 1.11 to the application of this turbulence box, and find a similar equation relating the variance of AoA to $C_n^2\delta h$, L_0, l_0, and r_0:

$$\sigma^2_{\mathrm{AoA}}[x,y] = (2\pi)^{4/3}0.033C_N^2\delta h \int\int_{R^2} f_{x,y}^2(f^2 + L_0^{-2})^{-11/6}\exp\left(-l_0^2 f^2\right)\left[\frac{2J_1(\pi Df)}{\pi Df}\right]^2 \mathrm{d}f_x\mathrm{d}f_y \tag{3.6}$$

where D is the diameter of the pupil, $f = f_x^2 + f_y^2$, and $f_{x,y}$ being either f_x or f_y depending on which direction of AoA is being calculated.

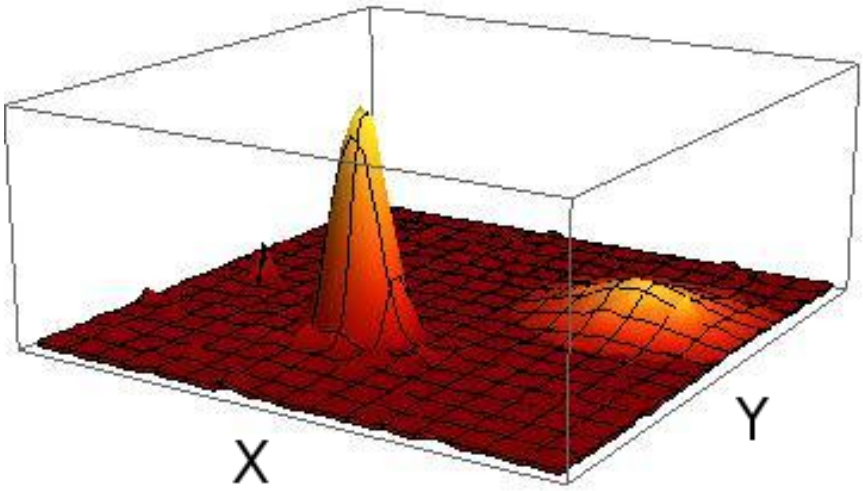

Figure 3.9: Sample spreading of the PSF between the two sets of conditions $\Delta T = 0$ (to the left) and $\Delta T = 60$ (to the right).

Under the infinite scale regime, where $L_0 = \infty$ and $l_0 = 0$, Equation 3.6 has an analytic solution given by

$$\sigma^2_{AoA}[x, y] = 2.8375 C_N^2 \delta h D^{-1/3} \quad (3.7)$$

$$= 0.1698(\lambda/D)^2 (D/r_0)^{5/3}. \quad (3.8)$$

Using the measured variances and chosen diameters of the pupil, the r_0 and $C_N^2 \delta h$ parameters can now be calculated (in the infinite scale regime). Table 3.3 displays the measured values for different temperature gradients.

Figure 3.10 shows the x and y variances plotted against each other for all experiments with temperature differences ranging from 0°C to 90°C and iris diameters from 2mm to 20mm, to determine the anisotropy of the turbulence box. The slope of the plot is 0.73 which shows that the turbulence box tends to perturb more in the x direction than in the y direction. This can possibly be understood because the fans only input air in the x direction thus causing more turbulence along that axis. Also, the x direction was longer inside the box, which could allow for larger eddies and a different effect due to the outer

ΔT ($^\circ C$)	$C_N^2 \Delta h X$ ($m^{1/3}$)	$r_0 X$ (mm)	$C_N^2 \Delta h Y$ ($m^{1/3}$)	$r_0 Y$ (mm)	$C_N^2 \Delta h$ (mean) ($m^{1/3}$)	r_0 (mean) (mm)
0	2×10^{-13}	1000	1×10^{-13}	700	2×10^{-13}	900 ± 800[1]
20	1.0×10^{-10}	7	9×10^{-11}	8	9×10^{-11}	7 ± 1
30	2.7×10^{-10}	3.9	2.2×10^{-10}	4.4	2.5×10^{-10}	4.2 ± 0.8
55	2.1×10^{-10}	4.4	2.3×10^{-10}	4.3	2.2×10^{-10}	4.3 ± 0.6
90	1.2×10^{-9}	1.7	9×10^{-10}	2.1	1.1×10^{-9}	1.9 ± 0.8

Table 3.3: Calculated r_0 and $C_N^2 \Delta h$ values from the AoA experiment

scale turbulent flows being larger.

Using Equation 3.6 it is also possible to extract the values of l_0 and L_0. To do this, the least squares fit between Equation 3.6 and the data is calculated. In order to remove the contribution of $C_N^2 \delta h$, each point in the calculation is divided by the minimum value (for the data, $d = 2$mm), normalizing the equation with respect to the smallest diameter pinhole setting

$$\sigma^2_{\text{norm}}(L_0, l_0, d) = \frac{\sigma^2_{\text{AoA}}(L_0, l_0, d)}{\sigma^2_{\text{AoA}}(L_0, l_0, d_{min})}. \tag{3.9}$$

This technique is given in [25]. Also, since the inner and outer scale are only related to the dynamics of the turbulence, and not the temperature, the value calculated for all the trials can be averaged to find a better value for these variables. The fan speed was constant in all the trials which kept the dynamic variables constant. Figure 3.11 shows one plot of the fit found. The inner scale for this turbulent box is $8.1\text{mm} \pm 4.4\text{mm}$ and the outer scale is $29\text{cm} \pm 17\text{cm}$. The value for the outer scale seems to be quite different from those reported of other boxes of this type [25, 76]. First, the outer scale is larger than the box itself which is physically not possible. It seems the fitting method may not have found the best fit to the data or was too mathematically complex for a simple minimization routine. The inner scale is matches quite well with that reported by [76].

For future implementations of this box, in order to have it properly characterized, the most significant improvement could be achieved by changing the temperature control. The space heater used has no ability to fix the temperature and allow for stable heating. This can be rectified by attaching some form of heater onto the outside of the fan on the hot air intake side of the box. From the overall analysis of this box, it would appear that the

[1] This value, although not feasible since the box is much smaller, demonstrates that without a temperature difference in the box, there is no turbulence.

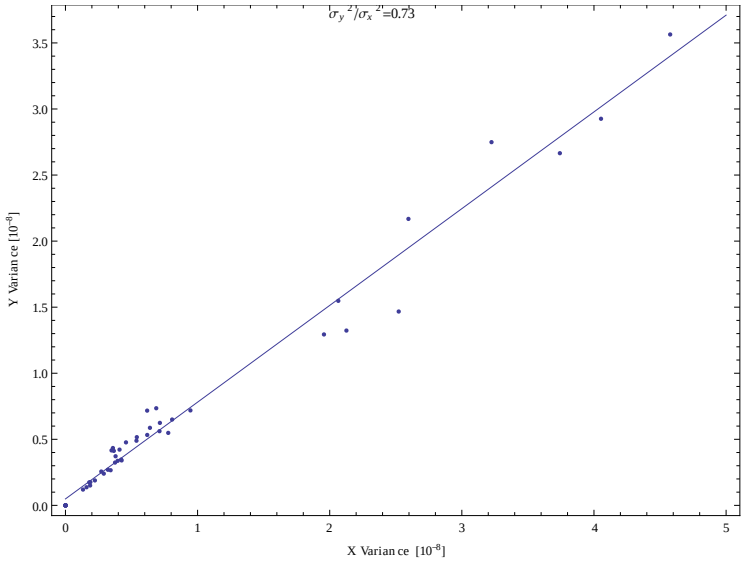

Figure 3.10: Isotropy of the turbulence box. The slope of the line is 0.73 showing a slight bias towards turbulence in the x direction.

turbulence created inside is much stronger than that of the real atmosphere. The fact that this box creates stronger turbulence than that of the real atmosphere is not necessarily a bad thing as it allows us to determine a lower bound on the expected performance of the quad sensor under scintillation. If the quad detector works with this turbulence, then it ensures sufficient performance with real atmospheric turbulence.

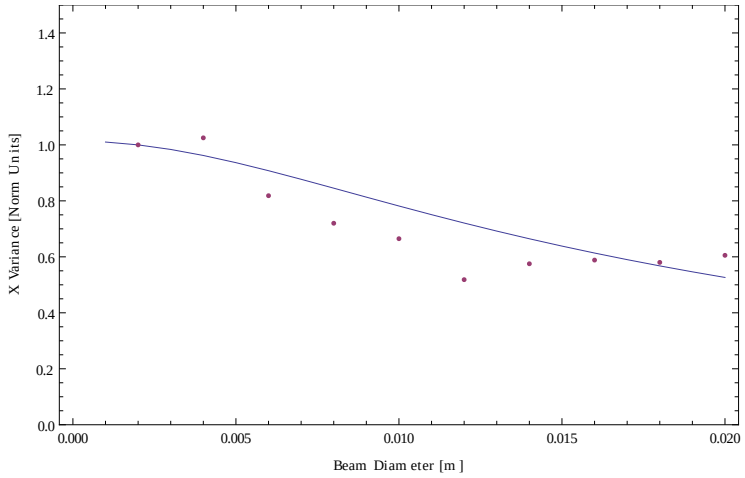

Figure 3.11: Least squares fit for the normalized Equation 3.6 to the experimental data at $\Delta T = 55\text{K}$.

3.4 Results

We now discuss the results of the various tests on the quad sensor with and without the turbulence box described above.

3.4.1 Characterization of System

One of the first things we did is measure the intensity on the quad and compare it to the modulation intensity created by the white noise generator. The power levels varied from $260\mu\text{W}$ to 2.75mW. For the intensity modulation, a voltage between 0 and 1.8V is applied to the laser controller which causes the fluctuations of the power levels. Figure 3.12 shows a time trace of the applied total measured intensity on the quad sensor compared to the applied voltage on the laser controller. It shows that there is a very strong correlation between the applied voltage and the measured results. The relationship between the modulation and measured signal goes as

$$\text{Output Power} = (2.75\text{V} - 1.38 \cdot \text{V}_{\text{mod}})\text{mW/V}, \tag{3.10}$$

(note that higher applied modulation voltage results in a lower beam intensity.)

The quad sensor gives a reading of -1.350V when the maximum modulation is applied and -7.300V when no modulation is applied. To find the relation between the intensity of the beam and the response on the quad sensor, two measurements were taken. One had

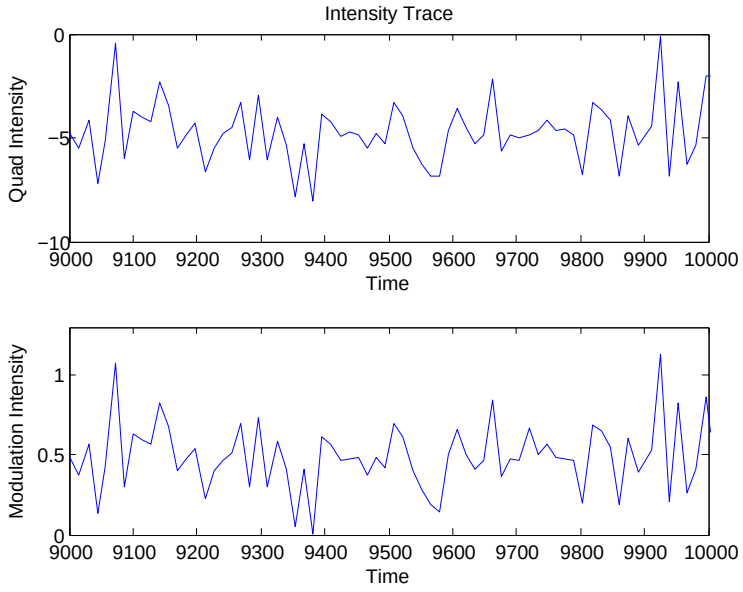

Figure 3.12: Trace showing the relation between the applied noise modulation voltage and the voltage sum recorded by the quad sensor. (Scale of the intensities is in V, and the scale of time is in milliseconds.) The relation between applied modulation voltage and beam intensity is $\text{Output Power} = (2.75\text{V} - 1.38 \cdot \text{V}_{\text{mod}})\text{mW/V}$.

the beam located on the center of the quad, and the other had the beam in one of the four quadrants. Figure 3.13 shows these two relations and the equations are

$$\text{Laser Intensity} = (-0.031\text{V} - 0.301 \cdot \text{V}_{\text{quad}})\text{mW/V}, \tag{3.11}$$

when the beam is in the center, and

$$\text{Lasaer Intensity} = (-0.00632\text{V} - 0.275 \cdot \text{V}_{\text{quad}})\text{mW/V}, \tag{3.12}$$

when the beam is in one of the quadrants.

In Figures 3.14–3.17, the quality of the Gaussian beam and the beam diameter (measured at 13.5% of maximum intensity) are shown for four different cases. To make the Gaussian quality measurement, a WinCamD CCD camera and DataRay software was used. The equation to calculate the quality of the Gaussian fit is:

$$\text{Fit} = 1 - \frac{\sum \text{Absolute Differences}}{\text{Gaussian Profile Area}}. \tag{3.13}$$

Fits which are closer to 1.00 approach ideal Gaussian curves. Each of the plots show measurements over 30 seconds. The DataRay program outputs the data only every second, even though the modulations are occurring at a much faster rate. By taking the measurement over 30 seconds, we catch most of the characteristics of the beam.

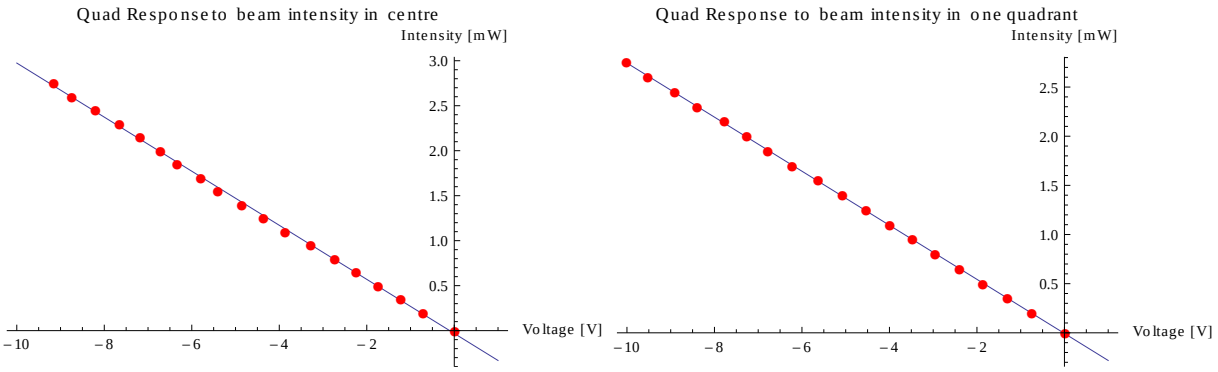

Figure 3.13: The plot on the left shows the relation between the sum voltage output of the quad sensor and the laser power when the beam is centered on the quad (right over the hole). The equation of the linear fit is $\text{Laser Intensity} = (-0.031\text{V} - 0.301 \cdot \text{V}_{\text{quad}})\text{mW/V}$. The plot on the right shows the same relation with the beam positioned in the top-right quadrant. The linear fit is given as $\text{Laser Intensity} = (-0.00632\text{V} - 0.275 \cdot \text{V}_{\text{quad}})\text{mW/V}$.

Overall the beam is relatively stable with few major fluctuations. In Figure 3.17 we see one major spike around the 20 second mark. This could be due to an intensity peak where saturation occurred on the CCD chip causing leaking onto other pixels, which would distort the beam shape from ideal.

3.4.2 Correlation Analysis Between the Quad and CMOS Sensors

To assess the quality of the quad sensor, the trace of the position reading with respect to the intensity and position modulation is analyzed and compared to that of the CMOS camera. The measure used here to determine correlations is the statistical p-value. The p-value can range from 0–1 with a low value, within 5% of zero for example, signifying a correlation between the signals. The detector is considered good if there seems to be no correlation between the modulation of the laser beam and the position reading on the quad sensor. Table 3.4 lists the p-values for the various signals. The first two rows of Table 3.4 show the relations between quad and CMOS x and y directions respectively. The p-values are all very close to zero ($\text{p} < 10^{-31}$) showing that the quad sensor and CMOS camera were very well correlated. The next four rows show the relations between the x and y directions on the quad and CMOS compared to the intensity noise modulation. Values we would like to see in this section would be above 0.05, showing no correlation. Six of the 24 measurements show some correlation between the two parameters, three for the quad and three for the CMOS. For the quad detector, the correlations are always in the y direction and for the CMOS it is in both. The last two rows of the table show very strong

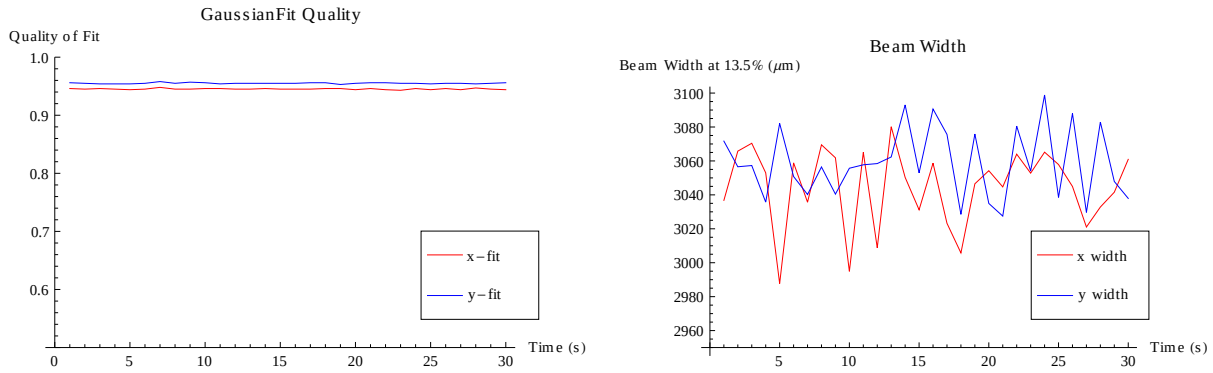

Figure 3.14: Quality of the Gaussian beam and the beam width over a time interval of 30 seconds. The intensity of the beam is constant, the turbulence box is turned off and the beam is circular.

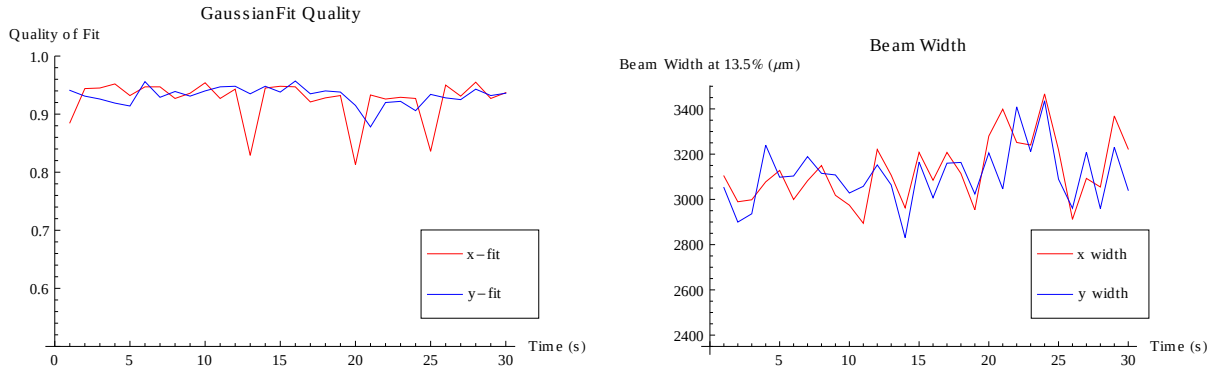

Figure 3.15: Quality of the Gaussian beam and the beam width over a time interval of 30 seconds. The intensity of the beam is modulated with the noise generator, the turbulence box is turned on and the beam is circular.

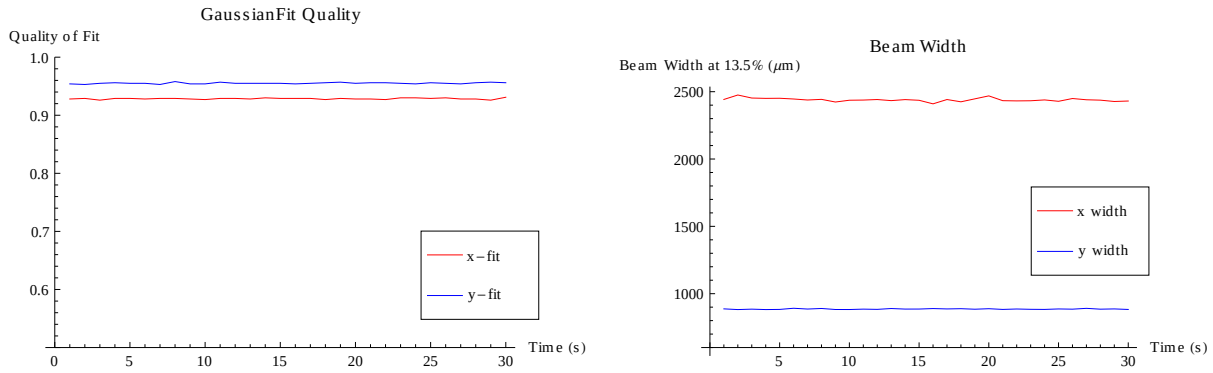

Figure 3.16: Quality of the Gaussian beam and the beam width over a time interval of 30 seconds. The intensity of the beam is constant, the turbulence box is turned off and the beam is elliptical.

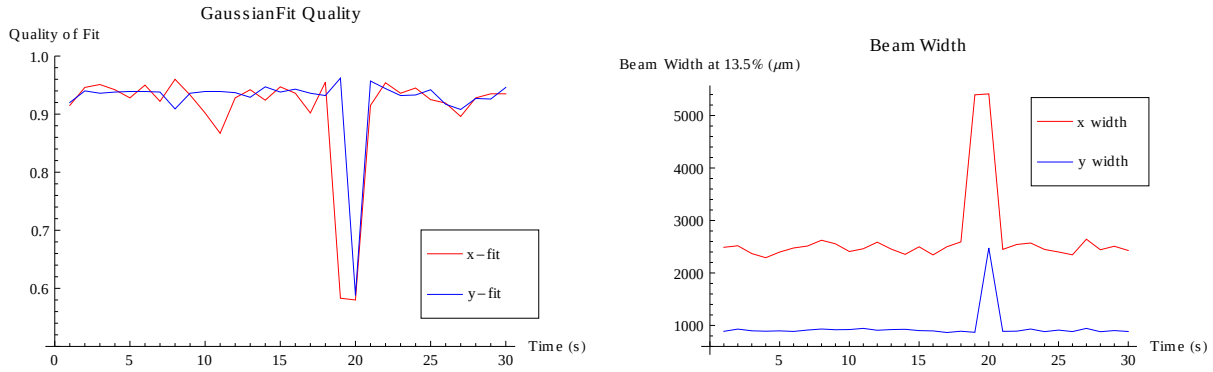

Figure 3.17: Quality of the Gaussian beam and the beam width over a time interval of 30 seconds. The intensity of the beam is modulated with the noise generator, the turbulence box is turned on and the beam is elliptical.

	Manual X-Axis Circular	Manual X-Axis Elliptical	Manual Y-Axis Circular	Manual Y-Axis Elliptical	Auto N/A Circular	Auto N/A Elliptical
QUAD X:CMOS X	0	0	0	0	1.1106E-313	3.1535E-260
QUAD Y:CMOS Y	5.951E-263	9.344E-031	0	0	5.0574E-280	6.2232E-304
QUAD X:NOISE	0.873	0.8606	0.057	0.2483	0.0978	0.2327
QUAD Y:NOISE	4.1499E-006	3.8528E-010	0.1195	0.317	0.0844	0.0141
CMOS X:NOISE	0.7843	0.9093	0.0391	0.1283	0.1505	0.126
CMOS Y:NOISE	0.8991	0.0706	0.1086	0.2719	0.0048	0.0123
QUAD SUM:NOISE	0	0	0	0	0	0
CMOS SUM:NOISE	0.0053	2.0838E-031	0.0028	6.1863E-004	1.9233E-070	1.4611E-050

Table 3.4: p-values for six different beam characteristics. "Manual" represents the mirror being moved by hand to displace the beam and "Auto" represents the turbulence box being used. The p-values represent the correlations between the two quantities separated by a colon in the first column. All the cases displayed in the table have the noise intensity modulation.

correlations between the sum on the sensors and the noise modulation, which agrees with expectation.

3.4.3 Correlation Analysis with Constant Intensity

To observe the system initially, there is no modulation in intensity on the beam, and the position intensity is created by moving the mirror before the beam splitter by hand. Figure 3.18 shows the modulation voltage intensity as a function of position for the quad sensor and the CMOS sensor. Figures 3.18–3.20 show results from moving only the screw on the mirror affecting the x direction and Figures 3.21–3.23 show results from moving the screw on the mirror affecting the y direction. Since there is constant intensity, Figures 3.18 and 3.21 have straight lines at zero intensity for modulation strength. By inspecting the motion of the beam on the CMOS, it is noticed that there is some motion orthogonal to the intended direction, which could be one possible reason for some of the dependencies we saw in p-values.

Figure 3.19 shows the correlations between each of the four possible x and y configurations of the quad sensor and the CMOS sensor. When moving the x direction we would expect a diagonal line in relation between the x coordinates of the CMOS and quad sensor which can be seen in the upper left plot. The bottom right shows relatively no movement in the y direction. Another noticeable feature of this data which was not anticipated is the

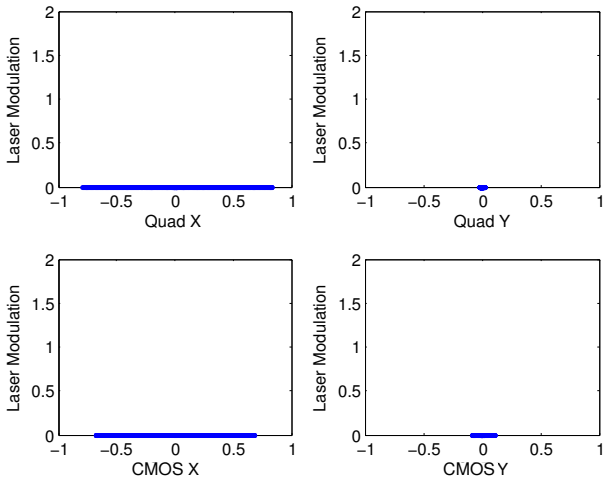

Figure 3.18: Moving the beam by hand and only in the x direction. The turbulence box is off and the laser is not being modulated in intensity (thus zero volts in Laser Modulation). Relations between the position on the quad sensor and the applied laser modulation are shown. The Laser Modulation scale is in volts.

slight wiggle in the upper right plot. A possible reason for this fluctuation could be due to a tilt in the camera angle relative to the quad sensor. This would create a slight dependence on the x direction of the quad sensor and the y of the CMOS sensor and vice-versa.

In Figure 3.20 one can see the CMOS and quad positions as a function of time. The bottom plot in the figure shows the total intensity on the quad sensor. The trace shapes are very similar between the CMOS and the quad, which is as expected. There is however a slight deviation, which has a few possible explanations. First, the area of the CMOS sensor was smaller than that on the quad. This led to the beam moving off part of the CMOS which would change the resulting location from the center-finding algorithm of the beam. The CMOS camera was also extremely sensitive to beam shape and profile changes which made accurate center-finding difficult. The small changes in intensity seen in the bottom plot can be attributed to moving through the hole on the quad where some of the light exits through to the back, as well as the gaps between each quadrant.

3.4.4 Correlation Analysis with Modulated Intensity

Now the noise modulation on the intensity is introduced to the laser beam, as well as using the turbulence box to create positional disturbances.

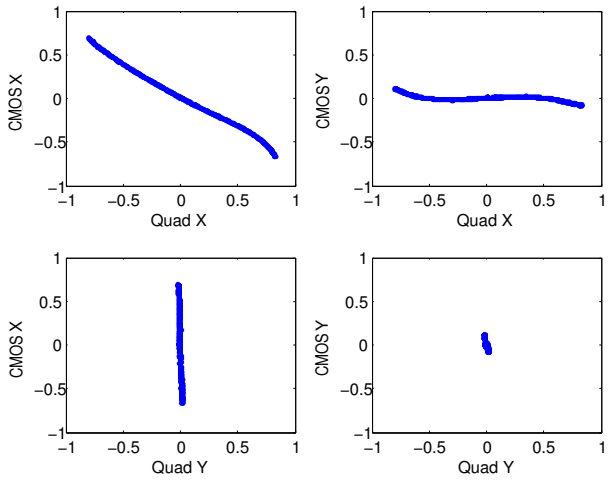

Figure 3.19: The beam is moved by the steering mirror manually in the x direction. The relationships between all four possibilities of position correlations between the quad sensor and CMOS sensor are shown.

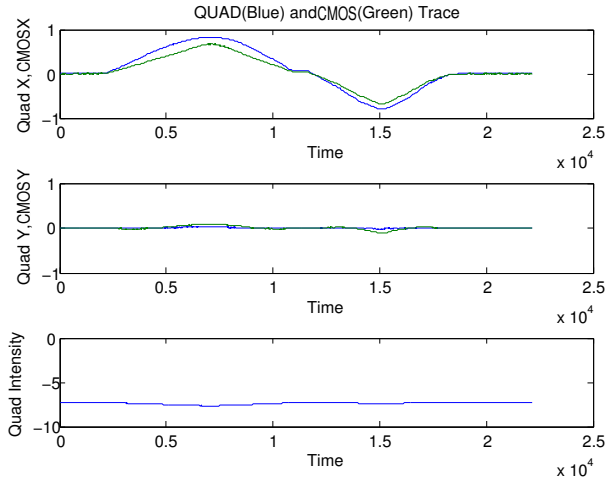

Figure 3.20: Trace data for the quad sensor and CMOS camera is shown for moving the beam in the x direction. The intensity is constant and the turbulence box is turned off. The intensity scale in the third plot is in volts. The time scale is in milliseconds

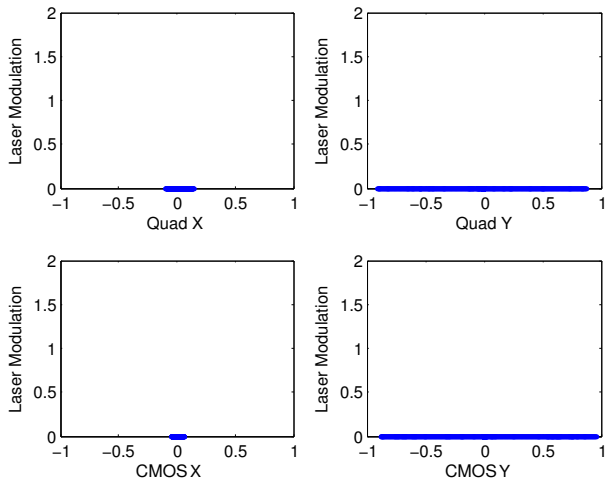

Figure 3.21: Moving the beam by hand and only in the y direction. The laser is not being modified in intensity and the turbulence box is off (thus zero volts in Laser Modulation). Relations between the position on the quad sensor and the applied laser modulation are shown. The Laser Modulation scale is in volts.

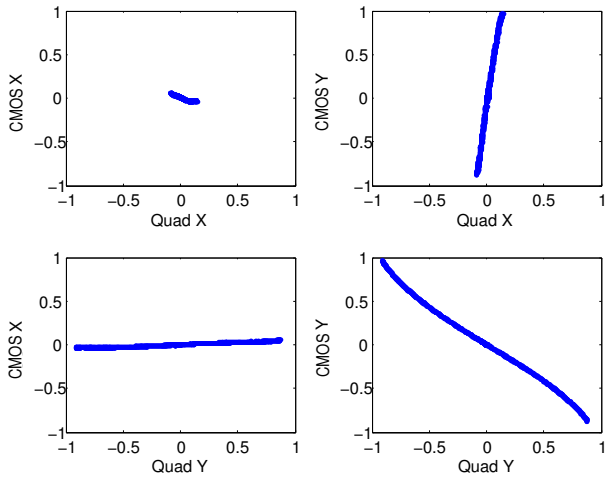

Figure 3.22: The beam is moved by the steering mirror manually in the y direction. The relationships between all four possibilities of position correlations between the quad sensor and CMOS sensor are shown.

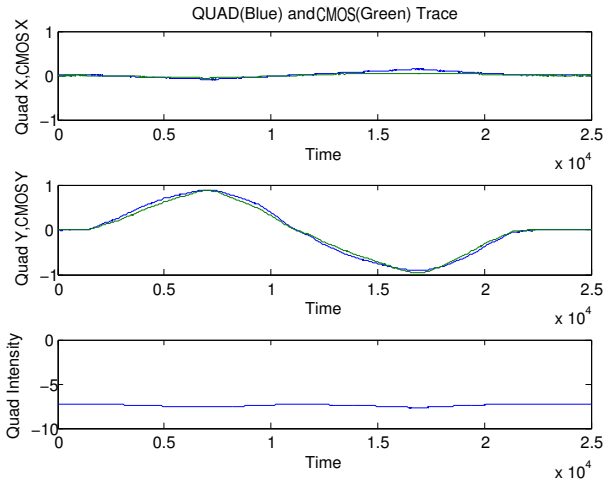

Figure 3.23: Trace data for the quad sensor and CMOS camera is shown for moving the beam in the y direction. The intensity is constant and the turbulence box is turned off. The intensity scale in the third plot is in volts. The time scale is in milliseconds

Without Turbulence

Figures 3.24–3.26 demonstrate movement only in the x direction and Figures 3.27–3.29 demonstrate movement only in the y direction.

In Figure 3.24, the laser modulation intensity is again plotted as a function of position on the quad and CMOS while scanning in the x direction. These plots show that there is minimal change in the quad y direction when the x direction is being manipulated. The CMOS does show some dependence in the y direction on x direction movements. The CMOS camera is much more sensitive to tiny changes as it is based on very small pixels, unlike the quad which is only based on four photodiodes. There is also again the possibility that the camera is not perfectly aligned to the orientation of the quad sensor. Note the distinct vertical lines in the upper left plot which is where the beam spent longer periods of time. The scans started in the center, moved to one side, then moved to the other side and back to the center (which is why the center vertical line is the thickest).

If the quad sensor worked just as well under intensity fluctuations as it does without, then it will be a good candidate for a pointing system on a satellite. In Figure 3.25 again the x position of the spot is moved on the CMOS and quad, but this time the intensity is modulated as well. The correlations are very strong as in Figure 3.19. There are some small differences and fluctuations along the line possibly explained as the frequency of modulation is somewhat higher than the frame-rate of the CMOS camera. The frequency modulation varied from 1 to 500Hz, whereas the frame-rate of the camera was only around

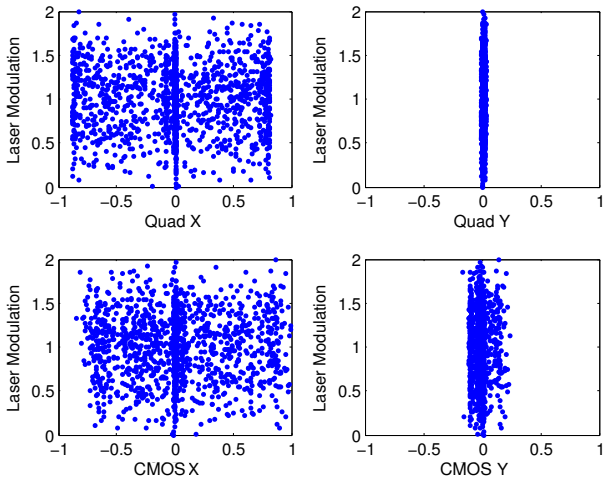

Figure 3.24: Noise modulation is now implemented on the laser intensity. The beam is scanned in the x direction. The scale of Laser Modulation is in volts.

72fps. This led to a slight delay of the camera from the quad sensor. However, even with this delay the correlations were still very strong.

Lastly in the x direction the time trace data is shown for the position of the x and y directions on the CMOS and quad. The positions again are strongly correlated and follow similar curves. The fluctuations in the CMOS path can again be attributed to the higher sensitivity and slower frame rate of the camera. One note is the bump in the CMOS y path in the latter half of the movement. Its origin is uncertain, but it could be due to normalization differences in the quad and CMOS algorithms (the beam leaving the CMOS active area causing a shift in the apparent position), or a physical bump of the mirror or camera. The bottom plot of Figure 3.26 helps demonstrate that even under strong intensity fluctuations, the position data is relatively unaffected.

It is noted that the movements in the y direction have slightly better correlations between the quad sensor and the CMOS camera than movements in the x direction. This is assumed to be due to the camera having a larger area in the y direction thus allowing more of the beam to stay on the camera active area during the movement.

With Turbulence

The turbulence box is now turned on the the system is allowed to settle. The box reaches a 30 degree Celsius temperature difference between the hot and cold air intake vents and the fans are each rotating at approximately 1500rpm. In Figure 3.30 the position correlations between the CMOS and quad are shown. The main features of this figure are the com-

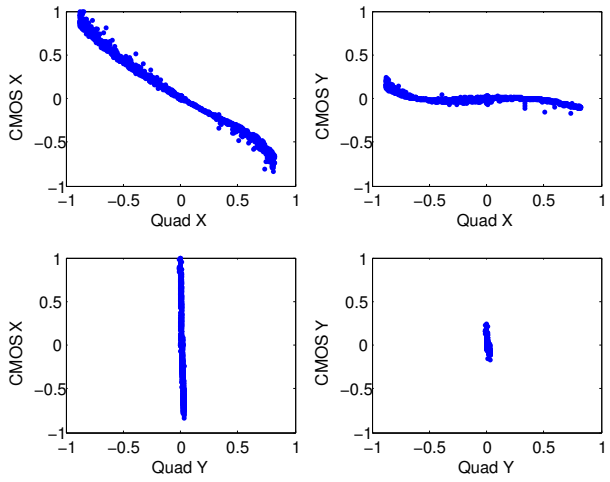

Figure 3.25: The beam is moved by the steering mirror manually in the x direction. The relations between all four possibilities of position correlations between the quad sensor and CMOS sensor are shown.

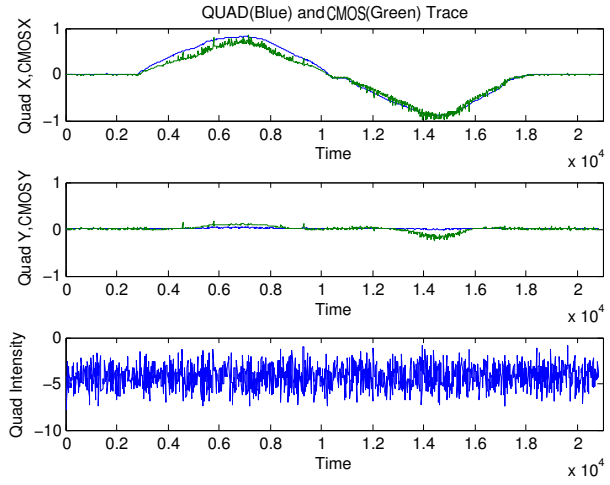

Figure 3.26: Trace data for the quad and CMOS while moving the beam in the x direction with random noise intensity modulation. The intensity scale is in volts for the third plot. The time scale is in milliseconds.

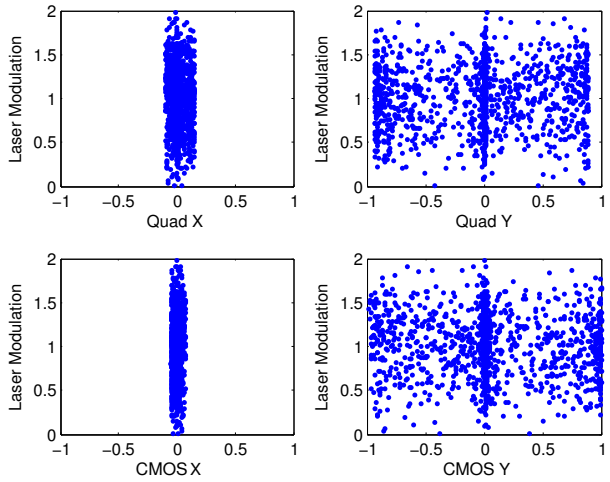

Figure 3.27: Noise modulation is now implemented on the laser intensity. The beam is scanned in the y direction. The scale of Laser Modulation is in volts.

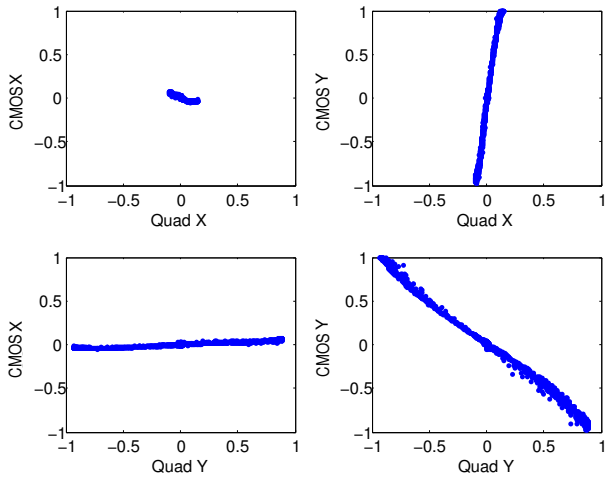

Figure 3.28: The beam is moved by the steering mirror manually in the y direction. The relations between all four possibilities of position correlations between the quad sensor and CMOS sensor are shown.

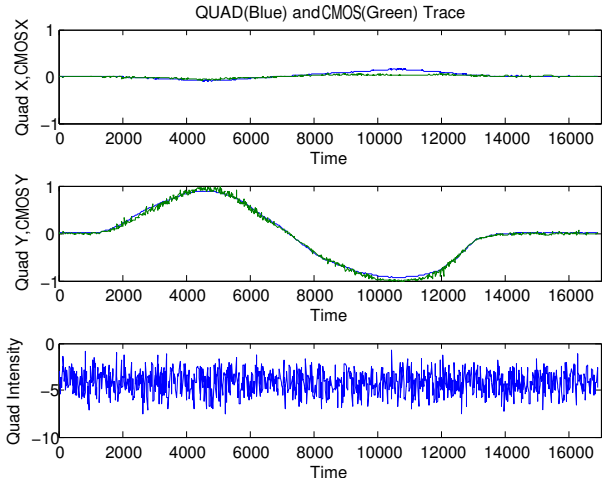

Figure 3.29: Trace data for the quad and CMOS while moving the beam in the y direction with random noise intensity modulation. The intensity scale is in volts for the third plot. The time scale is in milliseconds.

parison of the off diagonal plots compared to the diagonal plots. In the off diagonal plots, the pattern forms a circle showing very little if no correlation between the axes. However, in the diagonal photos, there is a distinct tendency to form a diagonal line. In the initial experiments with a slower frame-rate (≈24fps) this line was very difficult to see but as the frame-rate increased, the correlations emerged and became stronger. If the CMOS camera was able to achieve a higher frame rate (≈500fps) it is anticipated that the correlations would be very similar to those shown above when no turbulence box was present.

The trace data for an entire run with the turbulence box on and the intensity being modulated is shown in Figure 3.31. A zoomed in version on a small section is shown in Figure 3.32. The trace shows that the CMOS and quad positions follow each other very well. Increases in the frame rate of the camera improved the correlation in the traces as compared to the initial trials of the experiment. During these runs the camera was running at 24fps and the correlation in traces was very poor. The frame rate of the CMOS was determined by the size of the active area which the user defines, having the beam at 3mm put a limitation on the size of the active area we could minimize to which in turn put a restriction on the maximum frame rate. If the beam size were smaller, the active area could shrink in size and thus allow for a higher frame rate, which we anticipate would lead to even stronger correlations. Another feature, which is positive, is that the position traces seem to have no correlation to the total intensity measurement shown on the quad. This indicates that the position measurements have no correlation to the noise on the beam.

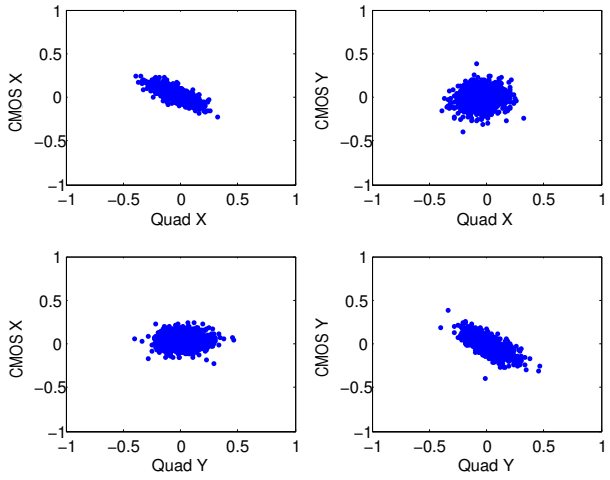

Figure 3.30: Correlations between the quad sensor and CMOS camera position with turbulence and intensity modulation.

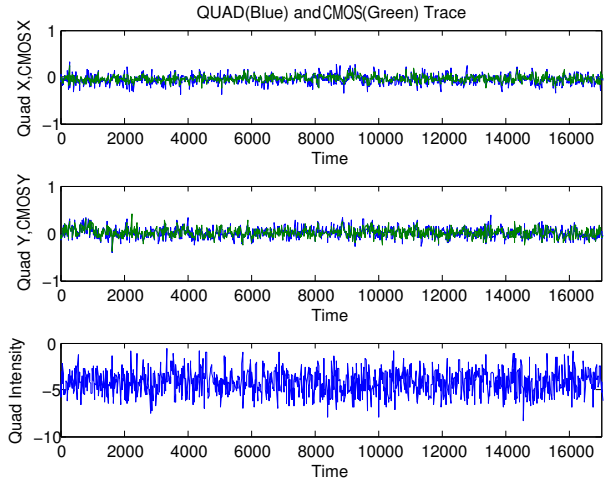

Figure 3.31: Trace data for the quad sensor and CMOS under conditions of simulated turbulence and intensity modulation. The intensity scale is in volts and the time scale is in milliseconds.

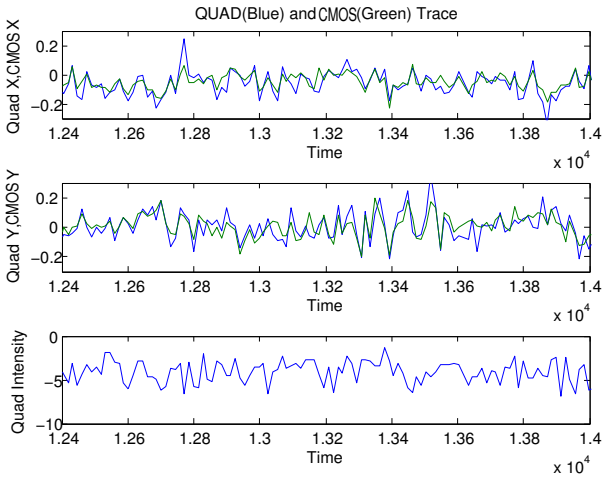

Figure 3.32: Zoomed-in image of Figure 3.31. The intensity scale is in volts and the time scale is in milliseconds.

Elliptical Beam

For the elliptical beam, new maximum and minimum powers were 3mW and 3μW respectively. Figures 3.33–3.36 represent the same tests as Figures 3.19–3.20 and 3.22–3.23, except now with the elliptical beam. The correlations are still very good between the CMOS position and the quad position.

Once the turbulence box and intensity modulation are turned on (Figures 3.37–3.39), the correlations are shown to be very similar to that of the circular beam. However, we note that the position traces do not follow each other quite as well as they did in the circular beam case. The y direction trace seems to follow better than the x direction case, which (as before) could be explained by the active area in the x direction being smaller than that of the y direction. The beam was oriented on the camera such that the major beam axis was along the x direction of the camera which leads to further errors from running off the active area. This problem was not understood until after the data was taken and analyzed and is why the beam was not oriented the other way.

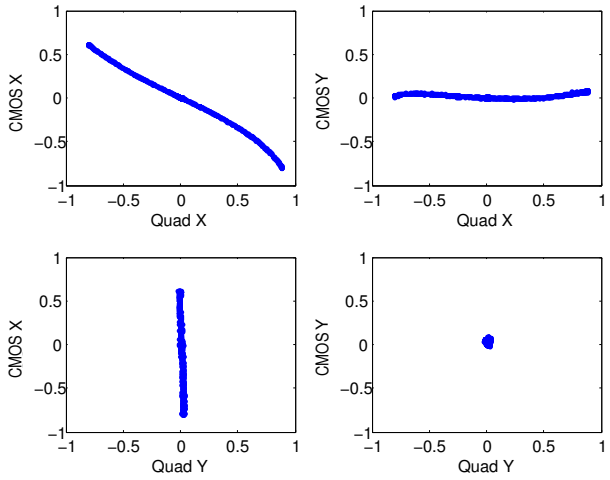

Figure 3.33: Position correlations between the quad and CMOS while moving the beam in the x direction with an elliptical beam. There is no intensity modulation or turbulence.

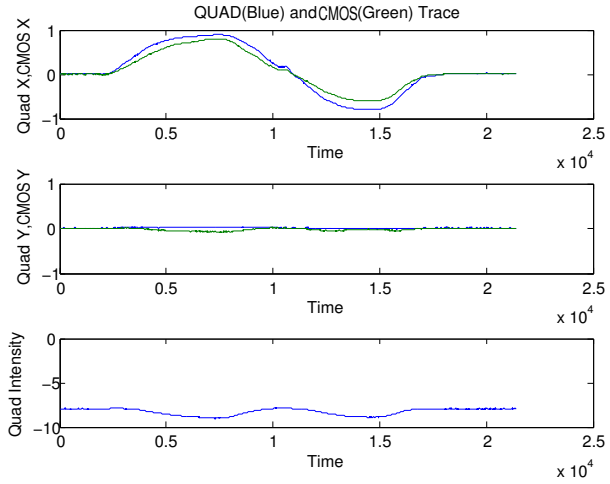

Figure 3.34: Position trace over time of the elliptical beam on the CMOS and quad while moving in the x direction with no intensity modulation or turbulence. The intensity scale on the third plot is in volts and the time scales are in milliseconds.

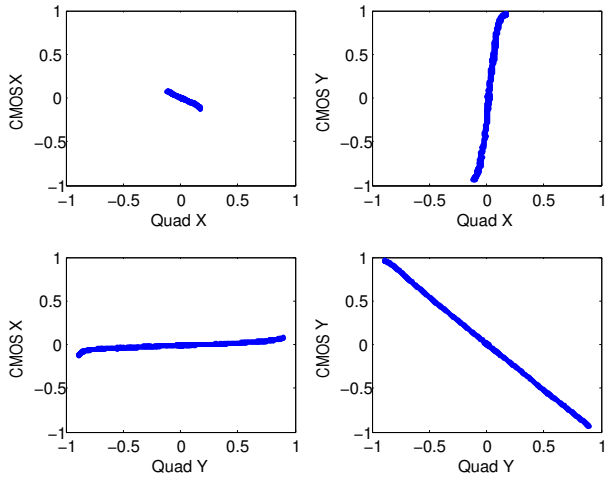

Figure 3.35: Position correlations between the quad and CMOS while moving the beam in the y direction with an elliptical beam. There is no intensity modulation or turbulence.

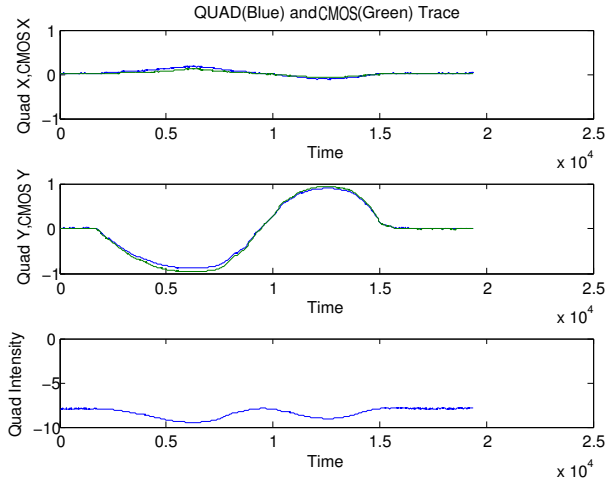

Figure 3.36: Position trace over time of the elliptical beam on the CMOS and quad while moving in the y direction with no intensity modulation or turbulence. The intensity scale on the third plot is in volts and the time scales are in milliseconds.

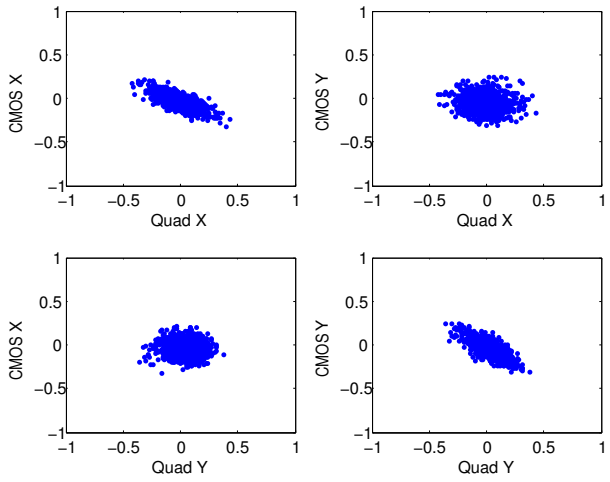

Figure 3.37: Position correlations between the quad and CMOS with an elliptical beam. There is intensity modulation and turbulence.

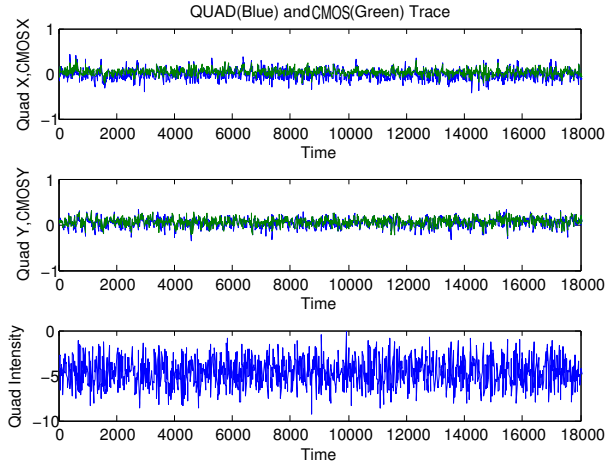

Figure 3.38: Position trace over time of the elliptical beam on the CMOS and quad while with intensity modulation and turbulence. The intensity scale on the third plot is in volts and the time scales are in milliseconds.

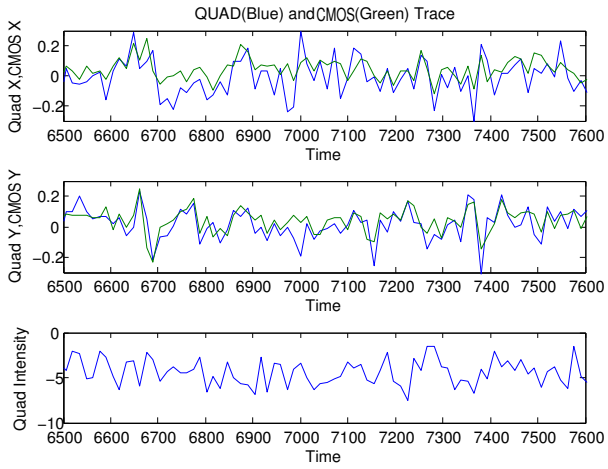

Figure 3.39: Zoomed-in view of Figure 3.38. Intensity scale in the third plot is in volts and the time scales are in milliseconds.

3.5 Discussion

The focus of this study was to determine the effect, if any, laser scintillation from passing through the atmosphere has on the performance of a quad position detector. As discussed in Chapter 1, there are many devices used for satellite acquisition, pointing and tracking, and the quad sensor tested here is a potential candidate. Through the study of perturbing a laser beam and comparing the results of the position on a CMOS camera with the quad sensor, it has been determined that this device performs well under scintillation effects.

A majority of the negative effects from this experiment seem to occur from inaccuracies of the CMOS camera. One problem was the decrease in performance on the x axis as compared to the y axis. One possible cause of this issue could be the fringe artifacts introduced by the beam splitter and attenuation optics. Since the beam splitter is oriented to reflect onto the CMOS camera in the horizontal direction, the fringes created will be close to vertical in orientation relative to the table. This would mean there would be more errors in the x direction as the distribution is not uniform across the pattern. These fringes were also very sensitive to frequency shifts and often changed as the laser frequency shifted with varying intensity.

Another issue, which could be improved with a switch in cameras or a smaller spot size, was the limitation on frame rate of the CMOS. This led to a slight lagging effect between the quad and CMOS readings. Unfortunately, with this particular quad sensor, we could not reduce the spot size as the hole in the center of the quad was on the order of a millimeter. With the camera used here, using a smaller active area would lead to a

faster frame rate and this was optimized for the spot used. Because the turbulence and intensity modulation occurred at rates on the order of hundreds of hertz, the roughly 72fps achieved by the camera was not enough to keep up with the modulations detected by the quad sensor.

It seemed that in some trials there was a correlation between the x and y axes of the position measurements. If this experiment were to be done again, it would be advantageous to ensure that the camera and quad were on identical planes thus purely separating out the x and y axes from each other.

One drawback observed when using this sensor is that the position reading from the quad sensor is only truly sensitive around the quad cross-hair, or the position of the hole. Because the beam used in this experiment was so large, this was not a problem, but with a smaller beam, this effect would be more pronounced.

Overall, the quad sensor, even with the hole, behaves in a very controlled manner. It appears to be very linear in response and does not show negative effects due to the scintillation or shape of the laser beam. Even the loss of intensity through the hole does not appear to affect it in a negative way. The quad, in fact, seems less sensitive to bad image effects than the CMOS causing its readings to fluctuate. It appears that the quad is actually more robust under random laser mode changes and fringe patterns than the CMOS, which is beneficial for pointing and tracking.

The next phase for testing the quad sensor would be to utilize one of the long distance free space links as discussed in Chapter 4. This would ensure that the sensor does actually perform the same under real turbulence conditions. Also, by implementing a stage system with the quad sensor, and using a tracking algorithm to keep the beam on the center of the quad, we can then inject the quantum signal into the laser system and test to see if the quad can track accurately and keep the quantum beam passing through the hole. This is the ultimate goal for this detector and is necessary if we are to use it for the satellite tracking system.

The turbulence box also has future use for many experiments. Many times it is very difficult to get equipment set up over the free space links and having a way to simulate turbulence in advance in the lab setting is of great benefit. This box will firstly be implemented into the system from Chapter 2 so the effects of turbulence can be observed on our pointing scheme as mentioned. This is the first step to incorporating real field parameters to this experiment before testing the schemes on functioning proto-types.

Before the box is placed into a functioning setup though, I believe it should be modified to make it more realistic, as well as easier to operate. The current heating mechanism is

challenging to operate and maintain a constant temperature. The dimensions of the box should also be reconsidered to allow for larger outer scale values closer to those that would be experienced in real circumstances.

Chapter 4

Contributions to the Mermin Parameter Violation Under Strict Locality Conditions Experiment

This chapter is based on an experiment completed in 2013 and the content has been submitted to a peer review journal in an expanded form with the following authors:

C. Erven, E. Meyer-Scott, K. Fisher, J. Lavoie, B. L. Higgins, Z. Yan, C. Pugh, J.-P. Bourgoin, R. Prevedel, L. K. Shalm, L. Richards, N. Gigov, R. Laflamme, G. Weihs, T. Jennewein, and K. Resch.

Author Contributions

C. Erven was the lead on this experiment and organized the various aspects of the project. He was also the creator of the software used for analysis of the experimental data. E. Meyer-Scott worked with the quantum random number generators and did theoretical analysis of count rates and violation of the inequalities. K. Fisher was involved in setting up the Pockels cells, building one of the receivers and assisting with the timing analysis. J. Lavoie designed, measured and built the source of the GHZ four-folds as well as had valuable insight into how to run the experiment as he had previous experience in three photon violations of the Svetlichny inequality. B. L. Higgins developed the space-time model on which the timing analysis is based for the locality conditions as well as in the functioning of the logic units. Z. Yan helped setup the RF links required for data transmission as well as helping with the electronics and functioning of the logic units. J.-P. Bourgoin helped with the infrastructure and trailer maintenance. R. Prevedel was very helpful with discussions and with work on the pockels cells. L. K. Shalm was also involved in designing the timing

analysis and ensuring we could work outside the locality loophole. L. Richards developed the software used to analyze the quantum random number generators. N. Gigov helped develop the software along with C. Erven. R. Laflamme and G. Weihs both helped fund the experiment as well as were available for discussion. T. Jennewein and K. Resch were the faculty leads and, as with C. Erven, helped in many different aspects of the project and with funding.

4.1 Overall Experiment Goals

The purpose of this overview is not to explain the detailed theory behind this experiment, but to give a brief background as to what the experiment aimed to show, and its significance.

In 1935, Einstein, Podolsky and Rosen published a paper stating that quantum mechanics was incomplete and that some other quantity (a local hidden variable) was required along with the wavefunction to explain nature [77]. Then in 1964 John S. Bell published his famous paper proving that any local hidden variable theory is incompatible with quantum mechanics [78]. Experimental confirmation of quantum mechanics [79] has been demonstrated by many (e.g. [80–82]).

However, all experimental "Bell" tests to date are subject to one or more caveats known as loopholes. Two major loopholes which have been studied are that of detector efficiency and locality. The detection efficiency loophole addresses the non unit efficiency of real–a deceptive universe may have it that detectors preferentially adhere to the rules of quantum mechanics and reject events which do not. This loophole has been independently closed in experiment [83]. The locality loophole is that information which will bias the measurement type can extend between the two measurement setups and always allow for positive quantum mechanical measurements to take place. In 1998, G. Weihs *et al.* performed an experiment where the condition of locality was enforced [84], which is an assumption made by the Bell theory. The experiment was performed showing no deviation from previous results, however with stronger evidence for the conclusion due to the locality condition being observed. The locality mentioned in this context encompasses both measurement locality (separation of measurements) and freedom of choice (basis choice separation with no influence able to travel between parties).

Experiments have also been done on Bell-type inequalities, experimentally verifiable proofs of quantum mechanics, with more than two particles [85, 86]. Multi-particle inequalities such as the Mermin inequality [87] or the Svetlichny inequality [88] have been a

popular topic of research as they represent a stricter "all or nothing" condition as compared to a 2-particle Bell test. A common three particle system to violate these inequalities has been proposed by Greenberger, Horne and Zeilinger (GHZ) [89].

To date no experiment has been done to violate a three particle Bell-type inequality while closing any loophole. Here, we violate a 3-particle Mermin inequality using a GHZ state while closing the locality loophole by setting up receivers spread throughout the Research and Technology park on the University of Waterloo North Campus. Figure 4.1 shows a map of the locations where the receivers are located relative to the building where the source is held. Two of the photons are distributed to trailers (Bob and Charlie) and one is held locally at the source after passing through a long delay fiber.

The receivers need to be able to choose their measurement basis with strict independence after the source creates the state, and they must also be far enough apart that a light-speed signal could not communicate these decisions to any other site before it measures its photon (this is the locality portion of the experiment). The location called Randy is where Alice's measurement basis choice is made, to keep her choice away from the source such that the locality conditions are satisfied despite the measurement physically taking place beside the source.

The magnitude of this project required contributions of many students and professors to be a success. Although the project lasted more than two years from conception to completion, I started working on it in the summer of 2012 and we completed the experiment portion in March of 2013. In this time, I had many different tasks to complete. A few of the major ones are listed in the sections below with other more mundane yet still important tasks including shoveling snow around the trailers in the winter, organizing plowing of the road to Bob when it snowed, and equipping the trailers with supplies to allow them to be comfortable for personnel to sit in them for the long nights of experiments. I was also stationed in Bob most nights of experimentation, monitoring counts and ensuring nothing went wrong in that trailer. Even though in some of the tasks below data was not possible to show or not relevant, they appear here because each of them took a decent amount of time to accomplish.

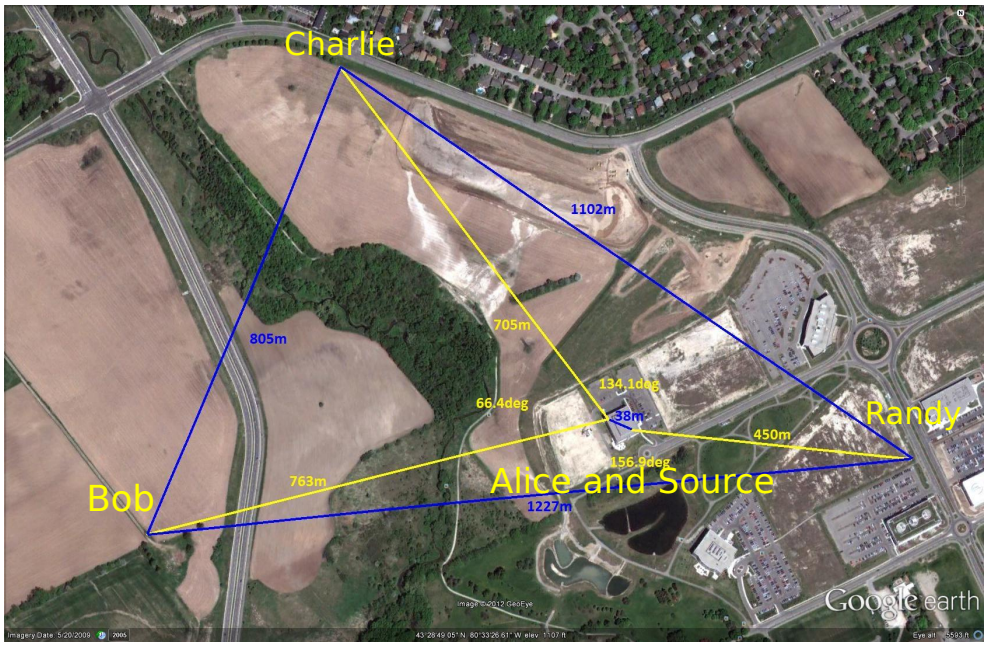

Figure 4.1: Map showing part of the University of Waterloo North Campus with the location of the three trailers holding the two optical receivers (Bob and Charlie) and the quantum random number generator (Randy) for Alice's basis choice. The building in the center is where Alice and the source are located, with a dome on the roof where the photons for Bob and Charlie were sent out.

4.2 Delays in Fibers

The photon source for this experiment was located in a lab on the first floor of the RAC 1 building on the University of Waterloo North Campus. In order to send the photons out to the trailers where the receivers were located, optical fibers ran from the source to a dome located on the roof of the RAC 1 where the sender telescopes were mounted. Because of the strict timing requirements in this experiment, we required the delay of each part of the setup to be accurately determined, including the time taken for the photons to travel from the source to the sender telescopes.

There were four fibers running up to the dome from the lab, two of which would be used in the final experiment. The procedure to obtain the time of photon travel through the fiber is explained here.

This test requires two local short fibers, the fibers to be tested, an SPDC source, a single photon detector, and a time tagger unit. The first delay which much be measured is the delay of the two short local fibers and the setup in general. To do this, we couple the two beams from SPDC into the fibers and attach the other end of the fibers to the single photon detector. The detector is then linked to the time tagger unit where the arrival time of the photons is output to a computer. Software analyzes the arrival time of the photons and will measure the coincidence count if the arrival times are within 1 nanosecond. The delay in one channel is then scanned in 0.1 nanosecond increments to find the peak of coincidence counts and the delay is inferred from the result. The plot for the local setup delay along with a line at the FWHM can be seen in Figure 4.2. A curve is then superimposed on to the data points and the values at the FWHM are averaged to obtain the delay offset.

Since the fibers going to the roof had already been laid, I had to find their delays as they were. Firstly, I left one fiber from the SPDC source connected to the photon detector. I attached the other fiber to the end of one of the fibers running to the roof. In the dome, I coupled two of the fibers together so the photon would make a round trip from the source, to the roof and back. The other end of the fiber that was coupled in the dome is then attached to the photon detector. The time tags are again analyzed and the delay offset is swept in 0.1 nanosecond increments. The resulting delay is then the delay from both the fibers that were coupled together. Since in the real experiment, the photons will only be going to the dome and not back, we needed to find the delay of each fiber individually. To do this, I recorded the delays of all the combinations of fibers connected and formed a system of equations to solve for the delay in each fiber. The measured data can be seen in Figure 4.3 and the resulting individual fiber delays can be seen in Table 4.1. The

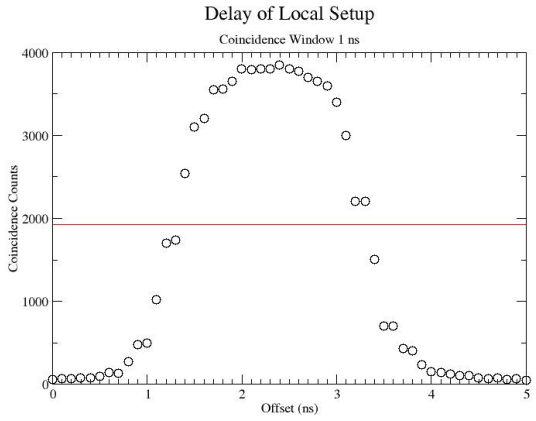

Figure 4.2: Data for the delay of arrival of the photons just from the local fibers and electronics.

Fiber	Delay
42	422 ± 3ns
43	420 ± 3ns
44	420 ± 3ns
45	421 ± 3ns

Table 4.1: Delays from the fibers going from the source in the lab to the roof, derived from data plotted in Figure 4.3.

fibers were labeled 42, 43, 44, and 45. The delays of the two fibers which were used in the experiment (42 and 44) were crucial parameters of the space-time model.

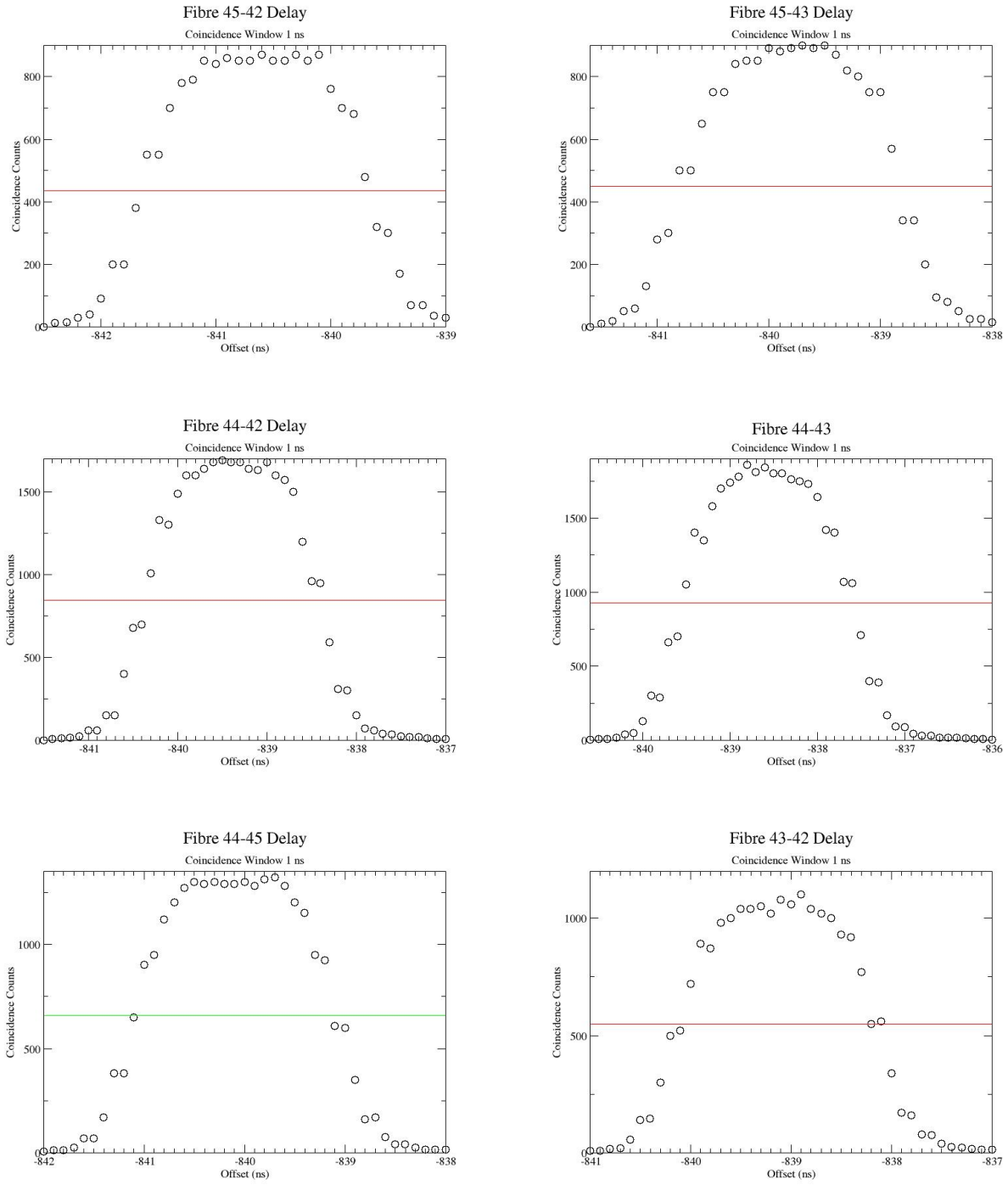

Figure 4.3: Delays between the photon arrivals of all the possible fiber combinations between the lab and the roof. This was then set into a system of linear equations and the delay for each fiber was found.

4.3 Receiver Stabilization

One of the major problems with housing the receivers for this experiment in trailers is stabilization. Initially, the receivers were on stands which were freestanding on the trailer floor. It quickly became apparent that any movement in the trailer caused the alignment to shift and photon counts would drop to zero. The experiment was not possible with the stand directly contacting the floor. Discussions with E. Meyer-Scott, C. Erven, K. Resch, T. Jennewein, J.P. Bourgoin and myself, concluded that the receiver should be decoupled from the trailer because personnel had to be in the trailer for monitoring the setup as well as tweaking alignment throughout the experiment.

We cut holes through the floor of the trailer and dropped 4×4 wooden posts into concrete blocks specially designed to hold these posts. A platform was then built on these posts which was no longer in contact with the trailer. The steel stand was then fastened to the wooden platform to prevent movement. The posts and final platform can be seen in Figure 4.4.

After this platform was installed by E. Meyer-Scott, J.P. Bourgoin and myself, counts were no longer affected by movement within the trailer.

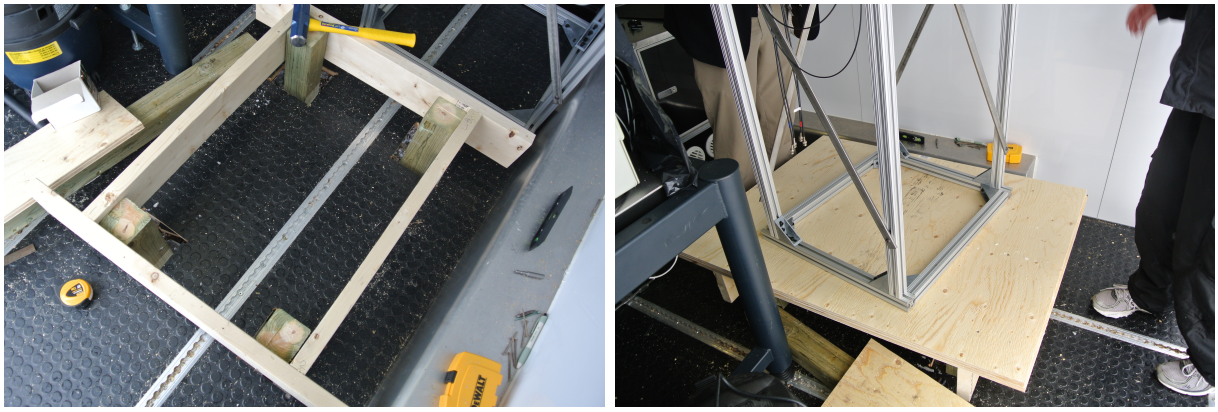

Figure 4.4: Platform designed and built to decouple the receiver from the trailer to prevent the receiver from moving during the experiment when people are in the trailer.

4.4 Classical Communication Channel

The software, which was written by C. Erven specially for this experiment, allowed real time analysis of the Mermin parameter, to determine whether or not it was being violated. However, in order for this to work, the time tags from Bob and Charlie had to be sent from the trailers back to the main computer in the lab through a classical link. I was tasked with finding a suitable solution to sending this data from each of the trailers back to the lab. Initially, I implemented three ASUS RT-AC66U routers, one located at each trailer and one in the dome to create an internal network. We used TP-LINK 2.4GHz antennae for the routers, with two antennae connected to the router in the dome, and one to each router at Bob and Charlie. This allowed a maximum upload speed from the trailers to the central computer of around 15Mbps[90], but was not reliable and often cut out, or did not work at all from start-up of each experimental attempt.

After much frustration and many test runs to keep the link working, K. Resch found an alternative company which sells industrial high speed internet equipment. After discussions with the technician at UBNT [91], we purchased two NanoStation M sender/receivers, one for each trailer, and the Rocket M sender/receiver for the dome. The Rocket M was attached to an AirMax Sector for an antenna, which has a 120 degree signal spread, covering the two trailers from the dome. We still used one of the ASUS RT-AC66U routers as a hub in the dome to allow the computer in the lab to connect to the internal network. Once I implemented this system, I tested the speed and found around 30Mbps upload speed from the trailers consistently. We also had 100Mbps download speed to the trailers with internet capabilities. Figure 4.5 shows the Rocket M inserted into the AirMax Sector aiming into the field towards the two trailers.

Figure 4.5: The Rocket M attached to the Airmax Sector antenna aiming out towards the two trailers. The antenna covered 120 degrees which easily encompassed the two trailers that required a classical data link.

This system allowed for real time analysis of the Mermin parameter and always was able to keep up with the data streaming from the trailers to the computer in the lab. It also allowed for responsive remote desktop connections between the computers in the trailers and the computer at the dome for telescope alignment at the beginning of each experimental run.

4.5 GPS Coordinates

Constructing the space-time model of this experiment requires the GPS coordinates for each of the relevant locations. This includes the location of Bob, Charlie, Randy, the dome, the receiving antenna from Randy to the lab, and the source. Because the source was located inside the building, the coordinates at each corner of the building were recorded and following a schematic diagram of the building, the coordinates for the crystal in the lab were calculated.

The GPS units used were Spectrum Instruments, Inc. Intelligent Reference TM-4's[92]. The software that is normally used with these instruments does not output the coordinates to a high enough precision for our application, so I developed software to collect the GPS data from the serial output data based on the custom software written by C. Erven for the

Location	Latitude (° N)	Longitude (° W)	Elevation (m)
Bob	43.477495	80.564536	330.1
Charlie	43.483830	80.560289	329.2
Randy	43.478300	30.549260	330.0
Dome	43.478907	80.555169	336.4
RAC RF Receiver	43.478717	80.554490	319.3
RAC NW Corner	43.478941	80.555278	329.2
RAC NE Corner	43.479114	80.554750	313.1
RAC SW Corner	43.478516	80.554976	328.7
RAC SE Corner	43.478623	80.554445	316.6
Source/Alice (derived)	43.478737	80.554759	320.8

Table 4.2: GPS coordinates for the various locations in the GHZ experiment needed for the timing diagram analysis to ensure closing the locality loophole.

main experiment.

To make an accurate measurement and account for some drift in the coordinates, I set the GPS receiver at each of the coordinates and waited for the unit to lock. Then I set the program running for approximately 10 minutes, recording the coordinates during that time. Once complete, the average of the coordinates was determined for each location. We used the factory specifications of 5m accuracy, for the positional uncertainty in our space-time model. Table 4.2 displays the averaged coordinates for each of the locations.

4.6 Discussion

Under the direction of Dr. C. Erven, we were able to complete this project with the results to be published soon (manuscript in preparation). The value measured for the Mermin parameter is 2.77 ± 0.08, violating the inequality bound of 2 by more than 9σ. The locality conditions were met and had tolerances of 263 ± 28ns for measurement locality and 304 ± 25ns for freedom-of-choice. Setting up all the infrastructure was part of the reason this experiment took so long to complete as many problems arose as we went along. The locality loophole is a challenging problem to overcome and took a very detailed space-time analysis to ensure that all the distances and delays in the experiment adhered to the restrictions. Having the Alice receiver located in the same lab as the source with the basis switching being received from an external source (Randy), caused many problems in itself,

and it would seem that placing Alice in another trailer in future multi-particle experiments could be an easier implementation.

Now that the infrastructure is in place, however, it allows us the possibility of conducting further experiments with either three or more photons. With the experiment succeeding in violating the Mermin inequality, a possible future direction of the experiment would be to alter the source to allow for the violation of the Svetlichny inequality. The measurements of the GPS coordinates as well as the delays of all the fibers and cables in the building can be stored for future use to make future experiments quicker. The trailers are also available for future long-distance free space links.

Chapter 5

Conclusion

The overall theme of the projects that I worked on through this Masters degree has been studying free space and quantum optics, with many of the challenges that are found within, as well as studying technologies for satellite acquisition, pointing and tracking. Many of the techniques developed in these projects will be important for the study of future technologies and ideas.

The theory discussed in Chapter 1 will be very important when our free space tests of the satellite technologies begin and a keen understanding of the ways to work around atmospheric turbulence in advance will be necessary when implementing these long distance experiments. The technology behind adaptive optics could also prove to be an important technique for photon transmission through the turbulent atmosphere.

Although the experimental portion of Chapter 2 has not progressed as far as I would have liked, the theoretical results are promising. The results that were achieved are (largely) consistent with the theory calculations. The future of this experiment is very promising and there are lots of ideas to progress forward. Mainly to extend the idler receiver across the lab and to introduce turbulence effects in the beam path. With this proposed setup, we will be able to test our steering scheme to see if it will be useful for real satellite applications.

The experiments conducted in Chapter 3 were done with tight time constraints. The turbulence box that was built was seen to affect the beam in a much more dramatic way than what would be observed in the real atmosphere. In one way this is unrealistic for a test on a device which will only be subjected to atmospheric turbulence, but if the device performs well under this intense turbulence, it should work very well when the turbulence is weaker. The quad sensor which was studied did show to work very well under these conditions, and we also exposed weaknesses in the CMOS camera reference sensor.

The Mermin parameter violation experiment from Chapter 4 was a great experience for working with large groups of people and for working out the problems that come with long distance experiments. Although it took many months to complete (and was extremely frustrating at times), it was certainly worth the work that was put in. The violation of the Mermin parameter by over 9σ while adhereing to locality conditions is a new result and will help further solidify the theory of quantum mechanics.

Overall, the experiments performed here represent significant steps towards the larger scale project and give direction for future theories and experiments into the components for the QKD satellite that is being proposed. Many of the issues which will come up when dealing with the real scenario have been addressed in these small scale experiments and techniques are being implemented to work around or solve these issues.

References

[1] C. H. Bennet and G. Brassard. Quantum cryptography: Public key distribution and coin tossing. International Conference on Computers, Systems & Signal Processing, 1984.

[2] M. Nielsen and I. Chuang. *Quantum Computation and Quantum Information*. Cambridge University Press, 2000.

[3] P. A. Hiskett, D. Rosenberg, C. G. Peterson, R. J. Hughes, S. Nam, A. E. Lita, A. J. Miller, and J. E. Nordholt. Long-distance quantum key distribution in optical fibre. *New Journal of Physics*, 8(9):193, 2006.

[4] M. Toyoshima, Y. Takayama, T. Takahashi, K. Suzuki, S. Kimura, K. Takizawa, T. Kuri, W. Klaus, M. Toyoda, H. Kunimori, T. Jono, and K. Arai. Ground-to-satellite laser communication experiments. *IEEE A&E Systems*, 23(8), 2008.

[5] J-P Bourgoin, E. Meyer-Scott, B. L. Higgins, B. Helou, C. Erven, H. Hübel, B. Kumar, D. Hudson, I. D'Souza, R. Girard, R. Laflamme, and T. Jennewein. A comprehensive design and performance analysis of low earth orbit satellite quantum communication. *New Journal of Physics*, 15(023006), 2013.

[6] *Acquisition and Tracking Terminal for Optical Inter-Satellite Communications*, 2001.

[7] P. Bandera. A fine pointing mechanism for intersatellite laser communication. European Space Agency Publications, 1999.

[8] G. Ortiz, S. Lee, and J. Alexander. Sub-microradian pointing for deep space optical telecommunications network. 19th AIAA International Communications Satellite Systems Conference, 2001.

[9] A. Skullestad. Pointing mechanism for optical communication. European Space Agency Publications, 1999.

[10] T. Aruga, K. Araki, R. Hayashi, T. Iwabuchi, M. Takahashi, and S. Nakamura. Earth-to-geosynchronous satellite laser beam transmission. *Applied Optics*, 24(1):53–56, 1985.

[11] SPIE. *Pointing and tracking subsystem design for optical communications link between the International Space Station and ground*, volume 3932 of *Free-Space Laser Communication Technologies XII*, 2000.

[12] ESA. *Optical Communications between an Aircraft & a Geo Relay Satellite: Design & Flight Results of the LOLA Demonstrator*, 7th International Conference on Space Optics, 2008.

[13] J.D. Barry. Space communications: Practical application of a visible nd: {YAG} laser. *Optics & Laser Technology*, 9(5):207–216, 1977.

[14] R. Barho and M. Schmid. Coarse pointing and fine pointing mechanism (cpa and fpa) for an optical communication link. 10th European Space Mechanisms and Tribology Symposium, 2003.

[15] Robert K. Tyson. *Principles of Adaptive Optics*. CRC Press, 3rd edition, 2011.

[16] A. N. Kolmogorov. The local structure of turbulence in incompressible viscous fluid for very large reynolds numbers. *Proc. R. Soc. Lond*, 434(1890):9–13, 1991.

[17] A. N. Kolmogorov. Dissipation of energy in locally isotropic turbulence. *Proceedings: Mathematical and Physical Sciences*, 434(1890):15–17, 1961.

[18] J. W. Strohnbehn ed. *Laser Beam Propagation in the Atmosphere*. New York:Springer-Verlag, 1978.

[19] G. K. Batchelor. *The Theory of Homogeneous Turbulence*. Cambridge University Press, London, 1953.

[20] R. J. Hill and S. F. Clifford. Modified spectrum of atmospheric temperature fluctuations and its application to optical propagation. *Appl. Opt.*, 68(7):892–899, 1978.

[21] G. R. Ochs and R. J. Hill. Optical-scintillation method of measuring turbulence inner scale. *Appl. Opt.*, 24(15):2430–2432, 1985.

[22] V. I. Tatarskii. *Wave Propagation in a Turbulent Medium*. New York: McGraw-Hill, 1961.

[23] V. I. Tatarskii. *The Effects of the Turbulent Atmosphere on Wave Propagation*. U.S. Dept. of Commerce, National Technical Information Service, 1971.

[24] S. Corrsin. On the spectrum of isotropic temperature fluctuations in an isotropic turbulence. *Journal of App. Phys.*, 22(4):469–473, 1951.

[25] E. Masciadri and J. Vernin. Optical technique for inner-scale measurement: possible astronomical applications. *Applied Optics*, 36(6):1320–1327, 1997.

[26] A. Fuchs, J. Vernin, and M. Tallon. Laboratory simulation of a turbulent layer: optical and in situ characterization. *Applied Optics*, 35(10):1751–1755, 1996.

[27] D. L. Fried. The effect of wavefront distortion on the performance of an ideal optical heterodyne receiver and an ideal camera. Conference on Atmospheric Limitations to Optical Propagation, 1965.

[28] D. L. Fried. Statistics of a geometric representation of wavefront distortion. *J. Opt. Soc. Am.*, 55(11):1427–1435, 1965.

[29] R. W. Duffner. Revolutionary imaging: Air force contributions to laser guide star adaptive optics. *ITEA Journal*, 29:341–345, 2008.

[30] G. A. Tyler. Adaptive optics compensation for propagation through deep turbulence: initial investigation of gradient descent tomography. *J. Opt. Soc. Am. A*, 23(8), 2006.

[31] A. Roorda. Adaptive optics for studying visual function: A comprehensive review. *Journal of Vision*, 11(5), 2011.

[32] J. W. Armstrong, C. Yeh, and K. E. Wilson. Earth-to-deep-space optical communications system with adaptive tilt and scintillation correction by use of near-earth relay mirrors. *Opt. Lett.*, 23:1087–1089, 1998.

[33] M. N. Horenstein, J. B. Stewart, S. Cornelissen, R. Sumner, D. S. Freedman, M. Datta, N. Kani, and P. Miller. Advanced mems systems for optical communication and imaging. *Journal of Physics: Conference Series*, 301(1), 2011.

[34] C. R. Phipps, K. L. Baker, B. Bradford, E. V. George, S. B. Libby, D. A. Liedahl, B. Marcovici, S. S. Olivier, L. D. Pleasance, J. P. Reilly, A. Rubenchik, D. N. Strafford, and M. T. Valley. Removing orbital debris with lasers. *Advances in Space Research*, 49(9):1283–1300, 2012.

[35] J. W. Hardy. Active optics: A new technology for the control of light. Proceedings IEEE, 1978.

[36] J. W. Hardy. Adaptive optics–a progress review. Proceedings SPIE, 1991.

[37] E. S. Claflin and N. Bareket. Configuring an electrostatic membrane mirror by least-squares fitting with analytically derived influence functions. *J. Opt. Soc. Am. A*, 3(11):1833–1839, 1986.

[38] N. Devaney, D. Coburn, C. Coleman, J. C. Dainty, E. Dalimier, T. Farrell, D. Lara, D. Mackey, and R. Mackey. Characterisation of mems mirrors for use in atmospheric and ocular wavefront correction. Proc. of SPIE, 2008.

[39] M. C. Roggemann and D. J. Lee. Two-deformable-mirror concept for correcting scintillation effects in laser beam projection through the turbulent atmosphere. *Applied Optics*, 37(21):4577–4585, 1998.

[40] J. D. Barchers. Closed-loop stable control of two deformable mirrors for compensation of amplitude and phase fluctuations. *J. Opt. Soc. Am. A*, 19(5):926–945, 2002.

[41] G. Andersen. Fast, autonomous holographic adaptive optics. Proc. of SPIE, 2010.

[42] F. Zernike. Diffraction theory of the knife-edge test and its improved form, the phase-contrast method. *Monthly Notices of the Royal Astronomical Society*, 94:377–384, 1934.

[43] M. Born and E. Wolf. *Principles of Optics*. Oxford: Pergamon, 5th edition, 1975.

[44] R. J. Noll. Zernike polynomials and atmospheric turbulence. *J. Opt. Soc. Am.*, 66(3):207–211, 1976.

[45] N. Roddier. Atmospheric wavefront simulation using zernike polynomials. *Optical Engineering*, 29(10):1174–1180, 1990.

[46] G. S. He. Optical phase conjugation: principles, techniques, and applications. *Progress in Quantum Electronics*, 26(3):131–191, 2002.

[47] G. Vdovin and P. M. Sarro. Flexible mirror micromachined in silicon. *Applied Optics*, 34(16):2968–2972, 1995.

[48] R. K. Tyson ed. *Adaptive Optics Engineering Handbook*. Marcel Dekker, Inc., 2000.

[49] T. Bifano, P. Bierden, and J. Perreault. Micromachined deformable mirrors for dynamic wavefront control. Proc. of SPIE, 2004.

[50] T. G. Bifano, R. K. Mali, J. K. Dorton, J. Perreault, N. Vandelli, M. N. Horenstein, and D. A. Casta non. Continuous-membrane surface-micromachined silicon deformable mirror. *Opt. Eng.*, 36(5):1354–1360, 1997.

[51] OKO Technologies. 17-channel micromachined deformable mirror with built-in tip-tilt stage: technical passport. Technical report, Flexible Optical B.V., 2012.

[52] OKO Technologies. Frontsurfer wavefront analysis and control system. Technical report, Flexible Optical B.V., 2011.

[53] J. M. Geary. *Introduction to Wavefront Sensors*. SPIE–The International Society for Optical Engineering, 1995.

[54] J. Hartmann. Bemerkungen uber den bau und die justirung von spektrographen. *Z. Instrumentenkd*, 20:47, 1900.

[55] J. Hartmann. Objektuvuntersuchungen. *Z. Instrumentenkd*, 24:1, 1904.

[56] R. B. Shack and B. C. Platt. Production and use of a lenticular hartmann screen. *J. Opt. Soc. Am.*, 61:656, 1971.

[57] B. E. A. Saleh and M. C. Teich. *Fundamentals of Photonics*. Wiley-Interscience, 2nd edition, 2007.

[58] D. Griffiths. *Introduction to Electrodynamics*. Pearson Addison Wesley, 3rd edition, 1999.

[59] K. Resch. Quantum optics class notes, 2012.

[60] R. Loudon. *The Quantum Theory of Light*. Oxford University Press, New York, 3rd edition, 2010.

[61] S. P. Walborn, C. H. Monken, S. Pádua, and P. H. S. Ribeiro. Spatial correlations in parametric down-conversion. *Physics Reports*, 495:87–139, 2010.

[62] A. Joobeur, B. E. A. Saleh, and M. C. Teich. Spatiotemporal coherence properties of entangled light beams generated by parametric down-conversion. *Phys. Rev. A*, 50(4):3349–3361, 1994.

[63] V. D. Salakhutdinov, E. R. Eliel, and W. Löffler. Full-field quantum correlations of spatially entangled photons. *Phys. Rev. Lett.*, 108(17), 2012.

[64] S. P. Walborn, P. H. S. Ribeiro, and C. H. Monken. Interference effects induced by non-local spatial filtering. *Optics Express*, 19(18):17308–17317, 2011.

[65] J. P. Torres, G. Molina-Terriza, and L. Torner. The spatial shape of entangled photon states generated in non-collinear, walking parametric downconversion. *J. Opt. B: Quantum Semiclass. Opt.*, 7:235–239, 2005.

[66] T. B. Pittman, D. V. Strekalov, D. N. Klyshko, M. H. Rubin, A. V. Sergienko, and Y. H. Shih. Two-photon geometric optics. *Phys. Rev. A*, 53(4):2804–2815, 1996.

[67] M. Minozzi, S. Bonora, A. V. Sergienko, G. Vallone, and P. Villoresi. Bi-photon propagation control with optimized wavefront by means of adaptive optics. *Optics Letters*, 38(489), 2013.

[68] J. C. Howell, R. S. Bennink, S. J. Bentley, and R. W. Boyd. Realization of the einstein-podolsky-rosen paradox using momentum- and position-entangled photons from spontaneous parametric down conversion. *Phys. Rev. Lett.*, 92(21), 2004.

[69] C. H. Monken, P. H. S. Ribeiro, and S. Pádua. Transfer of angular spectrum and image formation in spontaneous parametric down-conversion. *Phys. Rev. A*, 57(4):3123–3126, 1998.

[70] P. Kolenderski, W. Wasilewski, and K. Banaszek. Modelling and optimization of photon pair sources based on spontaneous parametric down-conversion. *Phys. Rev. A*, 80(013811), 2009.

[71] P. Kolenderski and W. Wasilewski. Density matrix of a single photon produced in parametric down conversion derived. *Phys. Rev. A*, 80(015801), 2009.

[72] A. Dragan. Efficient fiber coupling of down-conversion photon pairs. *Phys. Rev. A*, 70(053814), 2004.

[73] A. U'Ren, C. Silberhorn, R. Erdmann, K. Banaszek, W. Grice, I. Walmsley, and M. Raymer. Generation of pure single photon wavepackets by conditional preparation based on spontaneous parametric downconversion. *Las. Phys.*, 15(1), 2005.

[74] Chris Pugh, Brendon Higgins, Jean-Philippe Bourgoin, and Thomas Jennewein. QEYSSat APT–Scintillation Study. Technical report, Institute for Quantum Computing, 2013.

[75] Pacific Silicon Sensor Incorporated. Pacific silicon sensor series 6 data sheet. Technical Report QP50-6SD2, Pacific Silicon Sensor Incorporated, 2009.

[76] Onur Keskin, Laurent Jolissaint, and Colin Bradley. Hot-air optical turbulence generator for the testing of adaptive optics systems: principles and characterization. *Applied Optics*, 45(20), 2006.

[77] A. Einstein, B. Podolsky, and N. Rosen. Can quantum-mechanical description of physical reality be considered complete? *Phys. Rev.*, 47(10):777–780, 1935.

[78] J. S. Bell. On the einstein podolsky rosen paradox. *Physics*, 1:195–200, 1964.

[79] J. Clauser, M. Horne, A. Shimony, and R. Holt. Proposed experiment to test local hidden-variable theories. *Phys. Rev. Lett.*, 23(15):880–884, 1969.

[80] S. Freedman and J. Clauser. Experimental test of local hidden-variable theories. *Phys. Rev. Lett.*, 28(14):938–941, 1972.

[81] A. Aspect, P. Grangier, and G. Roger. Experimental realization of einstein-podolsky-rosen-bohm gedankenexperiment: A new violation of bell's inequalities. *Phys. Rev. Lett.*, 49(2):91–94, 1982.

[82] W. Tittel, J. Brendel, H. Zbinden, and N. Gisin. Violation of bell inequalities by photons more than 10 km apart. *Phys. Rev. Lett.*, 81(17):3563–3566, 1998.

[83] M. A. Rowe, D. Kielpinski, V. Meyer, C. A. Sackett, W. M. Itano, C. Monroe, and D. J. Wineland. Experimental violation of a bell's inequality with efficient detection. *Nature*, 309(6822):791–794, 2001.

[84] G. Weihs, T. Jennewein, C. Simon, H. Weinfurter, and A. Zeilinger. Violation of bell's inequality under strict einstein locality conditions. *Phys. Rev. Lett.*, 81(23):5039–5043, 1998.

[85] Jian-Wei Pan, D. Bouwmeester, M. Daniell, H Weinfurter, and A. Zeilinger. Experimental test of quantum nonlocality in three-photon ghz entanglement. *Nature*, 403(6769):515–519, 2000.

[86] J. Lavoie, R. Kaltenbaek, and K. Resch. Experimental violation of svetlichny's inequality. *New Journal of Physics*, 11(073051), 2009.

[87] N. D. Mermin. Extreme quantum entanglement in a superposition of macroscopically distinct states. *Phys. Rev. Lett.*, 65(15):1838–1840, 1990.

[88] G. Svetlichny. Distinguishing three-body from two-body nonseparability by a bell-type inequality. *Phys. Rev. D*, 35(10):3066–3069, 1987.

[89] D. M. Greenberger, M. Horne, and A. Zeilinger. Going beyond bell's theorem. *Bell's theorem, Quantum Theory, and Conceptions of the Universe*, pages 73–76, 1989.

[90] Speedtest.net. http://www.speedtest.net/.

[91] UBiQUiTi. http://www.ubnt.ca/en/.

[92] Spectrum Instruments, INC. http://www.spectruminstruments.net/.

Appendix A

Mathematica Code for Turbulence Box Characterization

A.1 Code for FWHM Experiment

```
(*Clear all the variables in the sheet before starting and import the appropriate image file*)
Clear[xMin, xMax, yMin, yMax, ImageFile, PeakImage, r, c, maxPixel,
 minPixelX, minPixelY, xGaussian, yGaussian, xGauss, yGauss, Values, $stream]
ImageFile = Import["//FilePath//File.tiff", "Data"];

(*Define the coordinates where the spot is and
 make sure it appears in the two images(roughly centered)*)
xMin = 380;
xMax = 420;
yMin = 200;
yMax = 250;
ListContourPlot[Take[ImageFile, {yMin, yMax}, {xMin, xMax}],
 DataRange → {{xMin, xMax}, {yMin, yMax}}]
ListPlot3D[Take[ImageFile, {yMin, yMax}, {xMin, xMax}],
 DataRange → {{xMin, xMax}, {yMin, yMax}}, PlotRange → {0, 60 000}]

(*Creates a subarray of the image which only holds
 the data to be analyzed instead of holding the entire picture*)
PeakImage = Take[ImageFile, {yMin, yMax}, {xMin, xMax}];

(*Finds the maximum pixel in the data for the peak of the PSF*)
Max[PeakImage]
r = 1;
c = 1;
maxPixel = 1;
For[i = 1, i ≤ Length[PeakImage], i++,
 For[j = 1, j ≤ Length[PeakImage[[i]]], j++,
  If[PeakImage[[i, j]] > maxPixel, r = i; c = j; maxPixel = PeakImage[[i, j]];];
 ]
]

(*Look at the 3D image where the peak is
 contained and check to see if any noise peaks are higher*)
ListPlot3D[PeakImage, PlotRange → All]

(*If there is noise peak which is higher,
set it to a value lower so it is not considered part of the PSF. Then rerun the above code to find
 the new max peak. Continue doing this until only the peak from the actual PSF is the max pixel*)
PeakImage[[r, c]] = 3000
```

```
  Take the pixels in the x cross section and in the y cross section and find
 their minimum. To make a better Gaussian fit, subtract the value of the lowest
 pixel from all the pixels to lower the outer edges to approximately zero
xGaussian  PeakImage  r
yGaussian  Flatten Take PeakImage, All,  c, c
minPixelX  Min xGaussian ;
minPixelY  Min yGaussian ;
For i  1, i  Length xGaussian , i  , xGaussian  i    xGaussian  i    minPixelX;
For i  1, i  Length yGaussian , i  , yGaussian  i    yGaussian  i    minPixelY;
Values  Table 0,  i, 1 ,  j, 4  ;
  Find a Gaussian fit for the x and y cross sections. Show what the values
 of each of the variables is and then calculate the FWHM of the Gaussian fit.
xGauss  NonlinearModelFit xGaussian, a E^(-(x-b)^2/(2d^2)),  a, b, d , x ;
Normal xGauss
xGauss "ParameterTable"
  FWHM calculation
Values  1, 1    Abs ArcTan 2 Sqrt[2 Log 2]  xGauss "ParameterTableEntries"   3, 1    5.6 10^6  0.15
  Error in the FWHM
Values  1, 2    Abs ArcTan 2 Sqrt[2 Log 2]  xGauss "ParameterTableEntries"   3, 2    5.6 10^6  0.15
Show ListPlot xGaussian , Plot xGauss x ,  x, 0, 40 , PlotRange  All , PlotRange  All
  Same as above but for the y direction
yGauss  NonlinearModelFit yGaussian, a E^(-(x-b)^2/(2d^2)),  a, b, d , x ;
Normal yGauss
yGauss "ParameterTable"
Values  1, 3    Abs ArcTan 2 Sqrt[2 Log 2]  yGauss "ParameterTableEntries"   3, 1    5.6 10^6  0.15
Values  1, 4    Abs ArcTan 2 Sqrt[2 Log 2]  yGauss "ParameterTableEntries"   3, 2    5.6 10^6  0.15
Show ListPlot yGaussian , Plot yGauss x ,  x, 0, 50 , PlotRange  All , PlotRange  All
  Output the data to a file to be compiled and analyzed
$stream  OpenAppend "  FilePath  File.txt", BinaryFormat  True ;
Export $stream, Values, "Table"
WriteString $stream, "\n"
Close $stream
```

A.2 Code for AoA Experiment

```
(*Clear all the values before begining*)
Clear[yData, xData, Both, Points, Values]
(*Import the appropriate file containing the
 centroid positions from the camera in the following format:
   x1
   y1
   x2
   y2
   x3
   y3
    .
    .
    .
*)
Points = Import["FilePath//File.txt", "Data"];
(*Creat and poplulate tables for the x data, the y data, and a table with the points as {xn,yn}*)
xData = Table[0, {n, Length[Points] / 2}];
yData = Table[0, {n, Length[Points] / 2}];
Both = Table[0, {n, Length[Points] / 2}, {z, 2}];
j = 1;
k = 1;
For[i = 1, i ≤ Length[Points], i++,
 If[Mod[i, 2] == 1, xData[[j]] = Points[[i, 1]]; Both[[j, 1]] = Points[[i, 1]];
  Both[[j, 2]] = Points[[i + 1, 1]]; j++;, yData[[k]] = Points[[i, 1]]; k++;]]
j = 1;
k = 1;
(*Convert the data from pixel to angle of arrival*)
xData = xData * (6.7 * 10^-6) / 0.15;
yData = yData * (6.7 * 10^-6) / 0.15;
(*Remove any data which goes below zero as this was an algorithm or camera malfunction*)
For[i = 1, i ≤ Length[xData], i++, If[xData[[i]] ≤ 0., xData = Delete[xData, i];
  yData = Delete[yData, i]; Points = Delete[Points, i]; Both = Delete[Both, i]; i--;]]
For[i = 1, i ≤ Length[yData], i++, If[yData[[i]] ≤ 0., xData = Delete[xData, i];
  yData = Delete[yData, i]; Both = Delete[Both, i]; i--;]]
Both = Both * (6.7 * 10^-6) / 0.15;
ListPlot[Both, PlotRange → All]
(*Set the value of the pupil diameter in mm and wavelength in
 nm. Create a table which will contain the important aspects of the data*)
d = 2;
λ = 633;
Values = Table[0, {i, 1}, {j, 8}];
(*Calculates the variance of the x data*)
Values[[1, 1]] = Variance[xData]
(*Calculates the variance of the y data*)
Values[[1, 2]] = Variance[yData]
(*Calculates the Cn^2δh profile in the x direction*)
Values[[1, 3]] = Solve[Variance[xData] == 2.8375 x (d * 10^-3)^(-1/3), x][[1, 1]][[2]]
(*Calculates the r0 value in the x direction.*)
Values[[1, 4]] = Solve[Variance[xData] == 0.1698 ((λ) / (d * 10^-3))^2 ((d * 10^-3) / r)^(5/3), r][[1, 1]][[2]]
(*Calculates the Cn^2δh profile in the y direction*)
Values[[1, 5]] = Solve[Variance[yData] == 2.8375 x (d * 10^-3)^(-1/3), x][[1, 1]][[2]]
```

```
  Calculates the r0 value in the y direction.
Values[1, 6] = SolveVariance[yData == 0.1698 A^2 (d/10^3)^2 (r/10^3)^(5/3), r, {1, 1}, 2]
  Calculates the Cn^2Δh profile for both directions together
Values[1, 7] = SolveVariance[xData == 2.8375 x (d/10^3)^(1/3), x, {1, 1}, 2]

    SolveVariance[yData == 2.8375 x (d/10^3)^(1/3), x, {1, 1}, 2, 2]
  Calculates the r0 value in both directions.
Values[1, 8] =
  SolveVariance[xData == 0.1698 A^2 (d/10^3)^2 (r/10^3)^(5/3), r, {1, 1}, 2]

    SolveVariance[yData == 0.1698 A^2 (d/10^3)^2 (r/10^3)^(5/3), r, {1, 1}, 2, 2]
Min[xData]
Min[yData]
Values
  Output the data into a file for analysis
$stream = OpenAppend["/home/chris/Documents/University/Masters/TurbBox/AoA/AoAData.txt",
   BinaryFormat -> True];
Export[$stream, Values, "Table"]
WriteString[$stream, "\n"]
Close[$stream]
```

A.3 Code for Calculating Inner and Outer Scales

```
(*Import the data from the appropriate file*)
FullData = Import["FilePath//AoAData.txt", "Data"];
(*Define the minimum value function for the normalization*)
MinimumValue[l_?NumericQ, L_?NumericQ] := NIntegrate[
```

$$fx^2 \left(\left(fx^2 + fy^2\right) + L^{-2}\right)^{-11/6} E^{-l^2 \left(fx^2+fy^2\right)} \left(\frac{2\,\text{BesselJ}\left[1,\ \pi\, 0.002 \sqrt{\left(fx^2 + fy^2\right)}\ \right]}{\pi\, 0.002 \sqrt{\left(fx^2 + fy^2\right)}}\right)^2 , \{fx, 0, \infty\}, \{fy, 0, \infty\}\Big]$$

```
(*Define the function to solve for L0 and l0*)
f[l_?NumericQ, L_?NumericQ, d_] :=
```

$$\left(\text{DData}[[d, 2]] - \frac{1}{\text{MinimumValue}[l, L]} \text{NIntegrate}\left[fx^2 \left(\left(fx^2 + fy^2\right) + L^{-2}\right)^{-11/6}\right.\right.$$

$$\left.\left. E^{-l^2 \left(fx^2+fy^2\right)} \left(\frac{2\,\text{BesselJ}\left[1,\ \pi\, (d/500) \sqrt{\left(fx^2 + fy^2\right)}\ \right]}{\pi\, (d/500) \sqrt{\left(fx^2 + fy^2\right)}}\right)^2 , \{fx, 0, \infty\}, \{fy, 0, \infty\}\right]\right)^2$$

```
(*Clear the sub array*)
Clear[DData]
(*Create the sub table and set the minimum value from the data for the normalization*)
DData = Table[0, {i, 10}, {j, 2}];
MinData = FullData[[21, 2]];
(*Counting variables*)
j = 0.002;
k = 1;
(*Populate the sub array with the variance of
 angle of arrival values and the diameters of the pupil*)
For[i = 21, i ≤ 30, i++,
 DData[[k, 1]] = j;
 DData[[k, 2]] = FullData[[i, 2]] / MinData;
 k++;
 j += 0.002;
]
Clear[j, k]
(*Minimize the least squares value between the function and the data over the variables L0 and l0*)
NMinimize[{Sum[f[l, 0.445929, d], {d, 1, 10, 1}], 0 < l < 0.02}, l,
 EvaluationMonitor :> Print["Step to l = ", l], WorkingPrecision → MachinePrecision, PrecisionGoal → 5]
```